MASSACHUSETTS INSTITUTE OF TECHNOLOGY

INTEGRATION OF VISUAL AND MOTION CUES FOR FLIGHT
SIMULATOR REQUIREMENTS AND RIDE QUALITY
INVESTIGATION
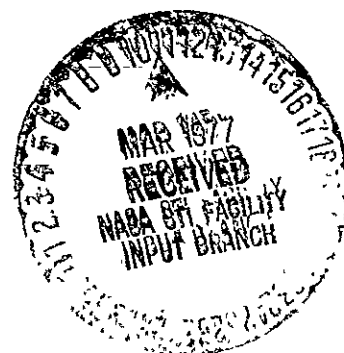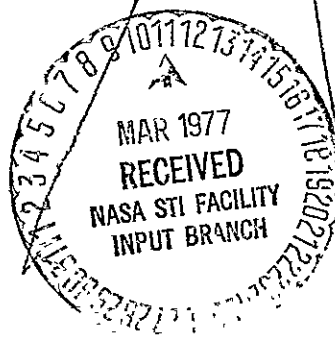
NGR 22-009-701

Status Report

June 1976 - December 1976

PRINCIPAL INVESTIGATOR

L.R. YOUNG

MAN-VEHICLE LABORATORY
DEPARTMENT OF AERONAUTICS AND ASTRONAUTICS
CENTER FOR SPACE RESEARCH
MASSACHUSETTS INSTITUTE OF TECHNOLOGY
CAMBRIDGE, MASSACHUSETTS 02139

HUMAN DYNAMIC ORIENTATION MODEL APPLIED TO MOTION SIMULATION

Work on this project has led to a Master's Thesis by
Joshua D. Borah.   The thesis is abstracted below.

Human Dynamic Orientation Model Applied to Motion Simulation

Joshua D. Borah

ABSTRACT

The Ormsby model of dynamic orientation, in the form of
a discrete time computer program, has been used to predict
non-visually induced sensations during an idealized coordi-
nated aircraft turn.   It was found that attitude and angular
rate perceptions may be contradictory and furthermore, in a
three rotational degree of freedom simulator, it is impossible
to duplicate both simultaneously.   To predict simulation fidelity,
a simple scheme was devised using the Ormsby model to assign
penalties for incorrect attitude and angular rate perceptions.
With this scheme, it was determined that a three rotational
degree of freedom simulation should probably remain faithful
to the attitude perception even at the expense of incorrect
angular rate sensations.   Implementing this strategy, a simu-
lation profile for the idealized turn was designed for a Link
GAT-1 trainer.   Use of a simple optokinetic display was proposed
as an attempt to improve the fidelity of roll rate sensations.

Two open loop subjective tasks were designed, to obtain
attitude and roll rate perception indications.   A series of
experiments were performed in our modified Link trainer to
test the effectiveness of the tasks and to check model predic-
tions and visual display effects.

PROGRESS REPORT

INTEGRATION OF VISUAL AND MOTION REQUIREMENTS

FOR FLIGHT SIMULATION AND RIDE QUALITY INVESTIGATION

June 1976 through December 1976

The following report briefly summarizes the work carried

on during this period. Included are sections on visual cues

in landing, comparison of linear and non-linear washout filters

using a model of the vestibular system, and visual vestibular

interactions (yaw axis). One of the major accomplishments of

this period was the completion of Mr. Joshua Borah's master's

thesis, a copy of which is being sent separately.

The subjective responses were self consistent, and both tasks are considered to be useful for obtaining low frequency information. An unexpected difference was found between subjective indications and model predictions for the turn simulation. It can probably be explained by the response lag inherent in the task (low bandwidth) plus consideration of dynamic detection threshold effects; but this must be clarified by further work. The optokinetic display was found to be insufficient to significantly improve roll rate perception fidelity in the turn simulation, probably due to the short duration of the movements involved.

Although not designed for the purpose, the predetermined simulation profiles were rated for realism by two pilots. The results did not contradict model predictions, although support was weak. A dynamic simulator motion logic was proposed, incorporating the strategy derived from the model. Its use would enable pilots to "fly" the simulator, and may provide more convincing data for use in evaluating and revising the fidelity prediction scheme.

HUMAN DYNAMIC ORIENTATION MODEL APPLIED TO MOTION SIMULATION

Work on this project has led to a Master's Thesis by Joshua D. Borah. The thesis is abstracted below.

Human Dynamic Orientation Model Applied to Motion Simulation

Joshua D. Borah

ABSTRACT

The Ormsby model of dynamic orientation, in the form of a discrete time computer program, has been used to predict non-visually induced sensations during an idealized coordinated aircraft turn. It was found that attitude and angular rate perceptions may be contradictory and furthermore, in a three rotational degree of freedom simulator, it is impossible to duplicate both simultaneously. To predict simulation fidelity, a simple scheme was devised using the Ormsby model to assign penalties for incorrect attitude and angular rate perceptions. With this scheme, it was determined that a three rotational degree of freedom simulation should probably remain faithful to the attitude perception even at the expense of incorrect angular rate sensations. Implementing this strategy, a simulation profile for the idealized turn was designed for a Link GAT-1 trainer. Use of a simple optokinetic display was proposed as an attempt to improve the fidelity of roll rate sensations.

Two open loop subjective tasks were designed, to obtain attitude and roll rate perception indications. A series of experiments were performed in our modified Link trainer to test the effectiveness of the tasks and to check model predictions and visual display effects.

VISUAL CUES IN LANDING

Introduction

The overall aim of the research is the development of
practical tools which can extend the state of the art of moving
base flight simulation for research and training. The immediate
goal is the determination of the relative importance importance
of various visual cues in flight simulation. The experiments
to be conducted for this research are intended to obtain the
perceptual response of humans to deviations from a nominal flight
path during landing approaches. An existing fixed-based aircraft
simulator is being modified to use a television projector with
which the subjects will be shown recorded television images of
landing approaches. Verbal estimates of the magnitude of flight
path deviations will be made by the subjects, and this data will
be used to construct a statistical model of the subject responses.

Five subjects were run through the experiment to help
refine the experimental protocol, evaluate the video tape con-
figuration and quality, and provide preliminary data. The results
are given later in this report.

4

Physical modifications of the simulator room were completed. These include the installation of the window shade and door shades, construction and mounting of the reflecting mirror for the projector, final positioning of the cockpit and minor rewiring of the electronics rack for a clearer field of view, and removal of the extra pane of glass from the cockpit window.

Sideways shaking of the image was an annoying problem in the preliminary tests. It was at first thought to be due to mechanical problems in the Redifon at Langley, but was eventually discovered to be due to electronic incompatibility between the Amphicon projector and the 1/2 inch video tape format. (The Amphicon has a 'slow' horizontal AFC instead of the more modern 'fast' AFC.) The problem was traced to the feedback loop around the horizontal oscillator in the Amphicon sweep chassis, and has been largely alleviated by modifying this circuit. The Amphicon will be realigned before running any more experiments. Further modification can then be done, if this proves necessary.

Current configuration of the video tapes is as follows:

5

(1) Long orientation run (backwards)

(2) Long orientation run. nominal approach

(3) Four scaling runs: minimum and maximum

                        deviations at each

                        distance

(4) Long orientation run

(5) Eight practice runs

(6) Long orientation run

(7) One hundred and twenty data runs

Separate scaling and practice runs are provided for glide path and aim point tests. Criteria for the practice runs were that they have equal numbers of positive and negative deviations, large and small deviations, and short and long distances (but not all possible combinations) Also, deviations in the stimulus not being overtly tested were kept to the minimum level. All practice runs were presented in a random order. The original Langley tapes were edited and copied to make a set of tapes in the current configuration.

6

The original tapes were recorded at Langley on a Panasonic NV-3020 video tape recorder. This type of recorder must be started and stopped by hand and has no electronic switching to avoid recording start-up transients, so the control track is destroyed between runs. During playback, there is insufficient time for the player to re-stabilize itself after the loss of the control track, and the Amphicon projector cannot lock on to the signal before the start of the next run. The resulting degradation of picture quality, although lasting for only a second or so, is unacceptable for such short and carefully timed runs. Conventional video editing (such as is used for creating the scaling and practice runs) often makes the problem worse.

In principle, "insert" editing should be able to solve the problem by recording the old video signal, independently of the control track, onto a tape with a brand-new control track. This method assumes that the editor's playing deck can provide a usable video signal despite the damaged control track on the original tape. A reliably functioning video editor capable of performing good inserts (which require such refinements as flying erase heads) has not been available to date, so the insert method has not been properly tested. If this approach fails, new tapes will have to be made. New tapes of different landing approach conditions will eventually be needed anyway,

7

and discussions of better methods of preparing them are in progress.

When the original tapes were made, the skyplate on the Redifon simulator was not properly calibrated. The skyplate covers the lens to show a blank 'sky', and is used to establish the visible ceiling by being partially opened. Lack of calibration caused this ceiling to vary from run to run, but only one subject noticed this. It is not considered very important as long as the entire runway is visible, which is the case in all of the runs on the current tapes.

Instructions to Subjects

The purpose of this experiment is to determine your ability to detect errors in glidepath and aim point during aircraft landing approaches   The experiment has two sets of video-taped landing approach runs   (To save time, only a short segment of each run is shown.) During each set, you will be asked to estimate either glide path or aim point errors for each run. Both kinds of errors may occur simultaneously, but you should estimate only the one asked for. Since altitude along the glide path and aim point

miss distance depend on initial distance from the runway, you
should base your estimates on the *ANGLES* of the glide path
and aim point vector errors (see description below).

Each set of runs begins with two orientation runs to
show you the touchdown point and a correct approach. Four
scaling runs follow to show you the largest errors in that
set for either glide path or aim point. You should call the
maximum positive and negative errors "+10" and "-10" respec-
tively, and estimate all other errors in terms of the -10 to
+10 scale. For example, a positive error half as large as
the maximum should be called +5. Except for orientation runs,
there are no normal approaches (with error equal to zero).

The "glide path" is the path through space that would
take you to the runway touchdown point. The correct glide
path is the "glideslope", which here makes a 3° angle to the
horizontal.

For any given glide path error, the difference in
altitude will change with the distance from the runway, so
you should estimate the *ANGULAR* error of the glide path (the
glide path error angle).

The "flight vector" is the direction you are moving in through space. The "aim point" is the place on the ground that you will reach if you continue along your present flight vector. The correct aim point is simply the runway touchdown point; to reach it, the flight vector must exactly align with the glide path.

In an actual aircraft, only the instantaneous flight vector angle can be controlled directly, not the ultimate aim point, and this experiment is set up accordingly. For any given flight vector angle error, the ultimate touchdown point depends on the initial distance from the runway. Also the absolute size of the aim point error is not symmetrical for initial symmetrical flight vector angle errors. So you should estimate the error of the flight vector *ANGLE*, rather than the ground distance of the resulting aim point.

Note that it is possible to reach the correct touchdown point, even if the glide path is incorrect, and that the aim point can be in error even if you start out on the proper glide-slope. If the flight vector is not aligned with the glide path, you may notice a slight change in the glide path during the run. If so, simply estimate the average glide path (or aim point), or that at the middle of the run.

10

A score of your performance during the test will be kept. You will not be scored on correctly estimating the exact size of the error, just the right direction (+ or =). Your score is simply the total number of estimates in the right direction. Your score does not represent your actual abilities as a pilot in a real aircraft and will be kept confidential.

The runs average about 8 seconds long each, with 3 seconds between runs, so you should make your estimates quickly. You will have 8 practice runs, and you may repeat the scaling and orientation runs if you wish.

Method and Preliminary Results

The current experimental setup is as follows:

Glidepath: 3° nominal

                  ±0.5°, ±1.0° deviations

                  (±1.5° training)

Flightpath·   3° nominal

                  ±0.6°, ±1.2° deviations

                  (±1.8 training)

Distance: 3000 ft, 6000 ft

//

The glide path is the vector from the aircraft to the desired touchdown point on the runway. The flightpath is the velocity vector of the aircraft.

Subjects are asked to give verbal estimates of the magnitudes of deviations on a subjective scale of -10 to +10, corresponding to the maximum deviations seen during the training runs. Each subject estimates either glide path or flight path, but not both, during any particular experiment.

A statistical model of the responses is constructed along the following lines:

Response = Mean + (Glide path) + (Flight path)

+ (Distance) + [...interactions...]

+ error

The model is not intended to establish any cause and effect relationships, but to establish instead the relative importance of the different visual stimuli.

For each experiment, we have the following stimuli:

4 glideslopes x 4 flightpaths x 2 distances

x 3 replications = 96 stimuli

14

Each subject sits through two experiments, one for glideslope and one for flightpath.
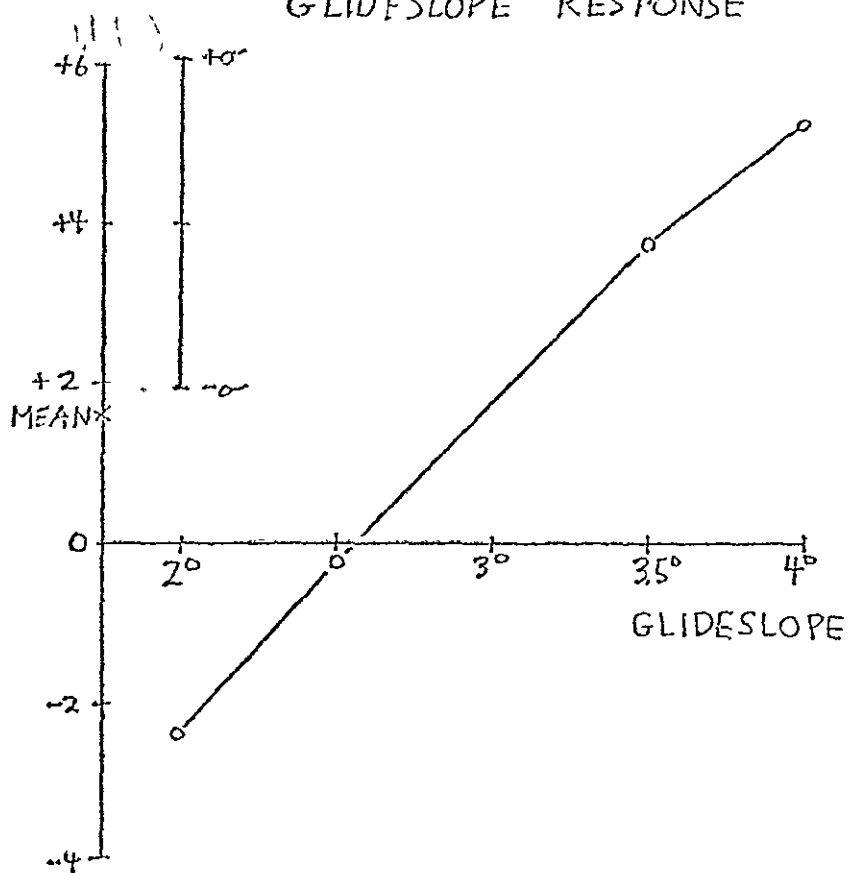
Plots of some of the results from a preliminary set of experiments are shown in the following figures. The actual magnitude of the deviation stimulus is given by the horizontal scale; the subject's response to that stimulus (as derived by the statistical model) is given by the vertical scale. The sigma bars, where present, represent ±1 standard deviation of the "error" in the response which could not be statistically explained by the model.

Keep in mind that the plots represent partial data from preliminary experiments. The subjects had different backgrounds of flight and simulator experience and variations in the experimental protocol were tried out. The plots were used primarily to test the application of the model, and do not all correspond to the same statistical confidence level or include all significant interactions. Nevertheless, they should give some indication of what the final data may look like.
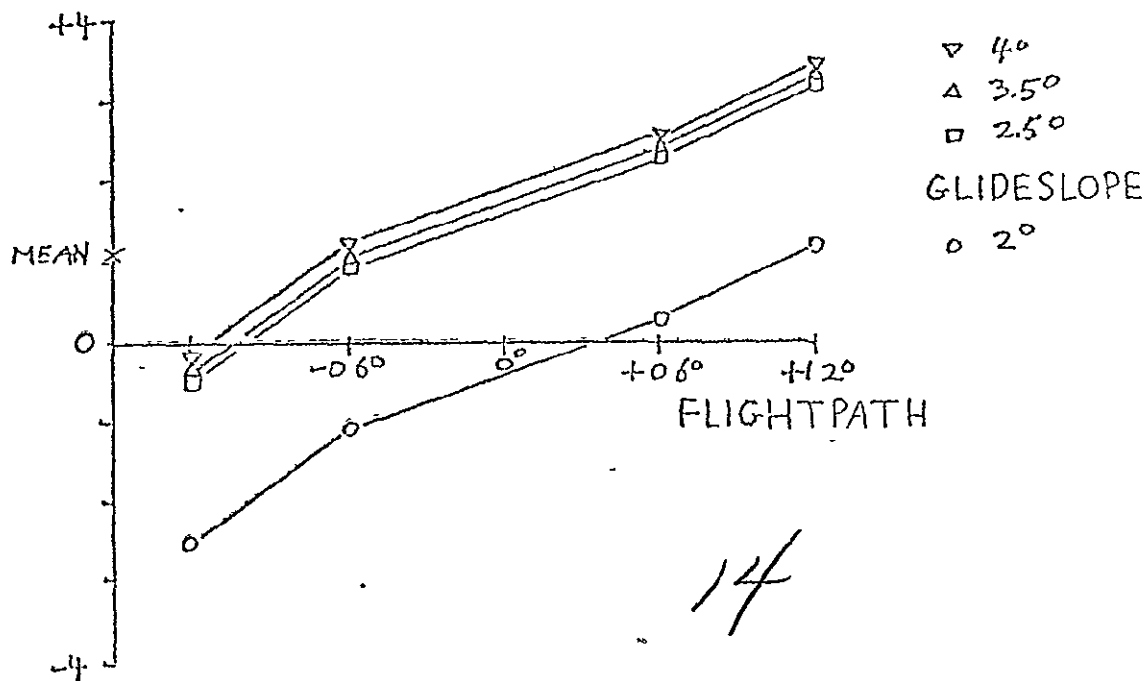
13

GLIDESLOPE RESPONSE

FLIGHTPATH RESPONSE

14

GLIDESLOPE RESPONSE

+σ

-σ

+5

0

-5

MEAN

2°   2.5°   3.5°   4°

GLIDESLOPE

DISTANCE

6000'

3000'

(7, 8)

GLIDESLOPE RESPONSE

+6

+3

0

-3

-6

+σ

-σ

MEAN

2°   2.5°   0°   3.5°   4°
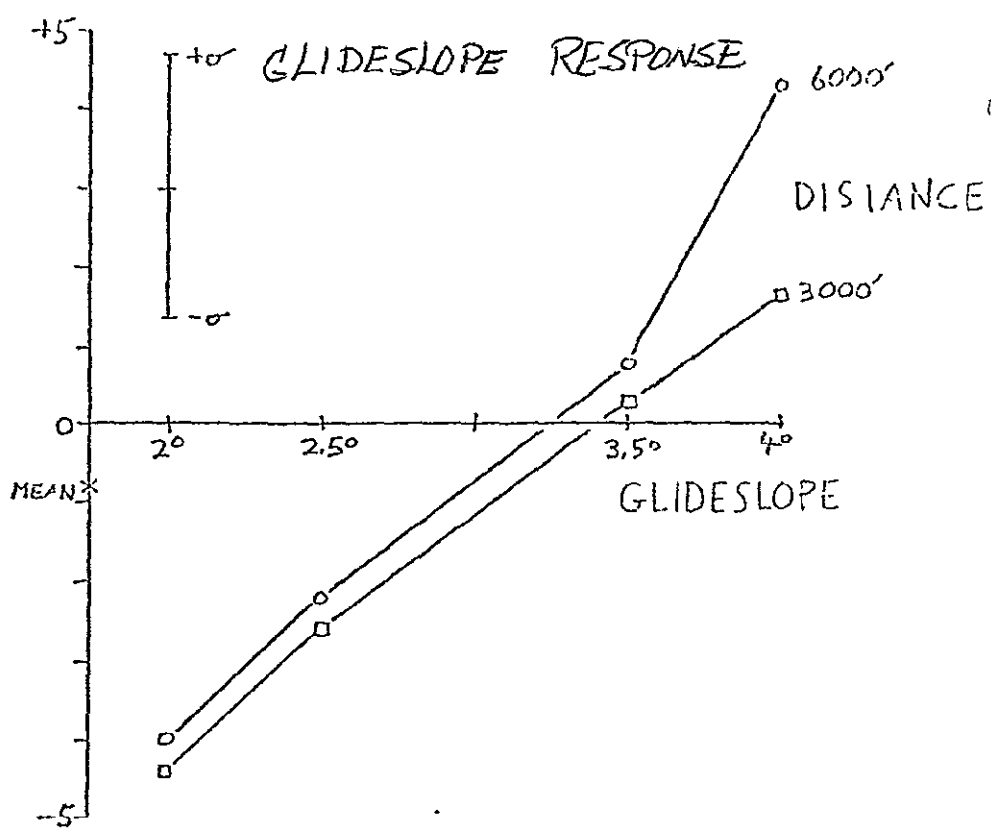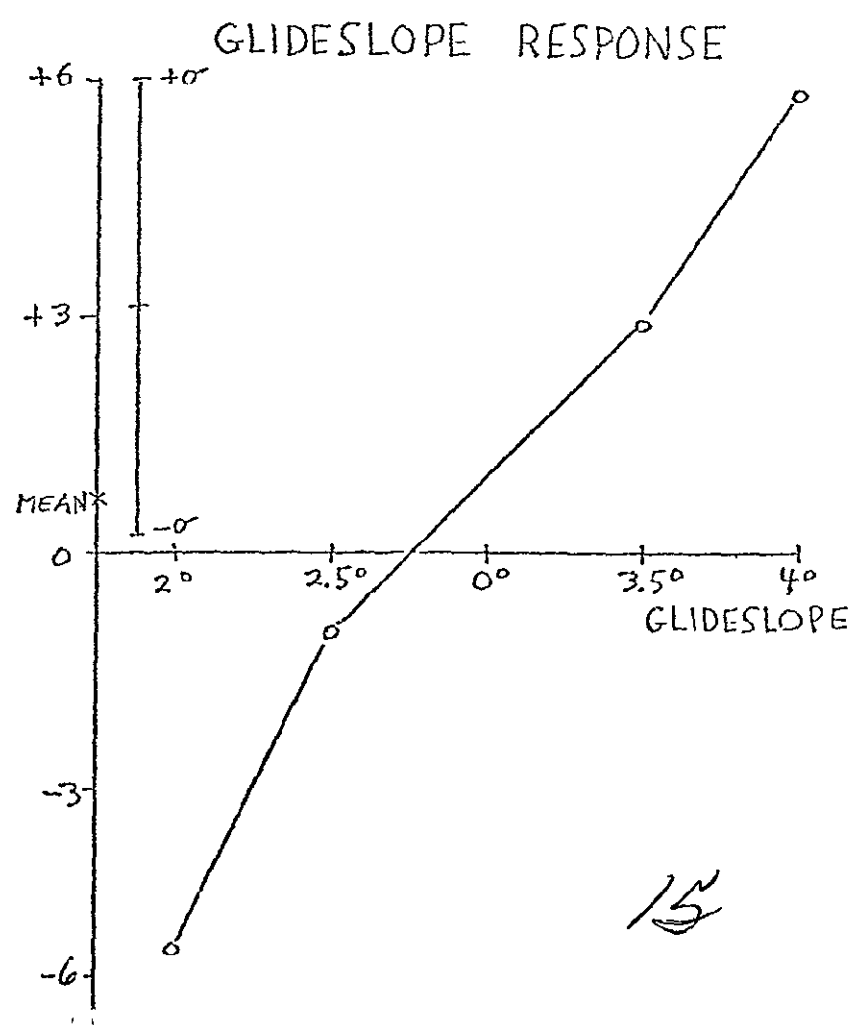
GLIDESLOPE

15

FLIGHT PATH   RESPONSES
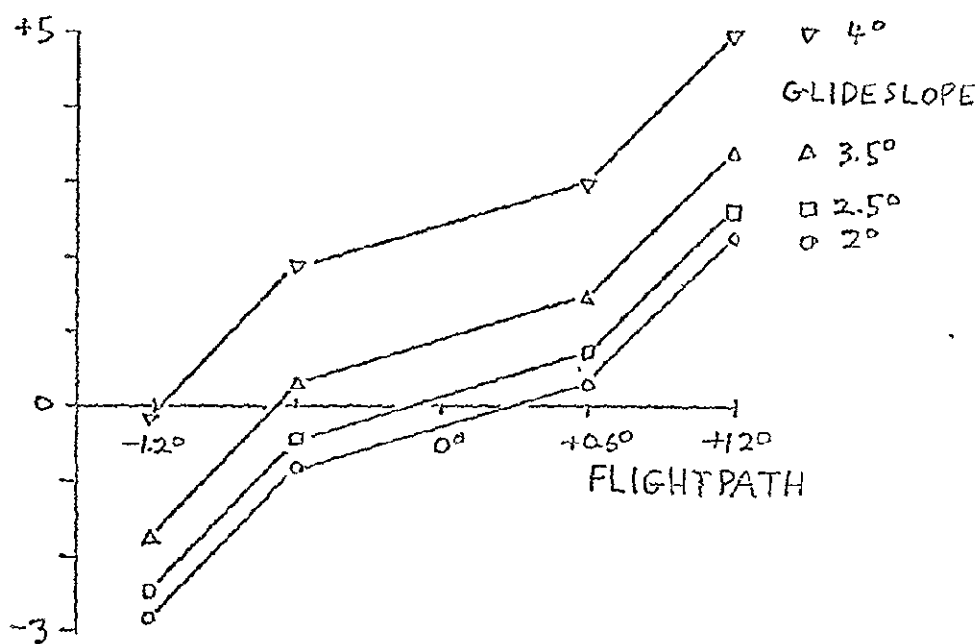
DISTANCE = 3000 ft.

DISTANCE = 6000 ft.

16
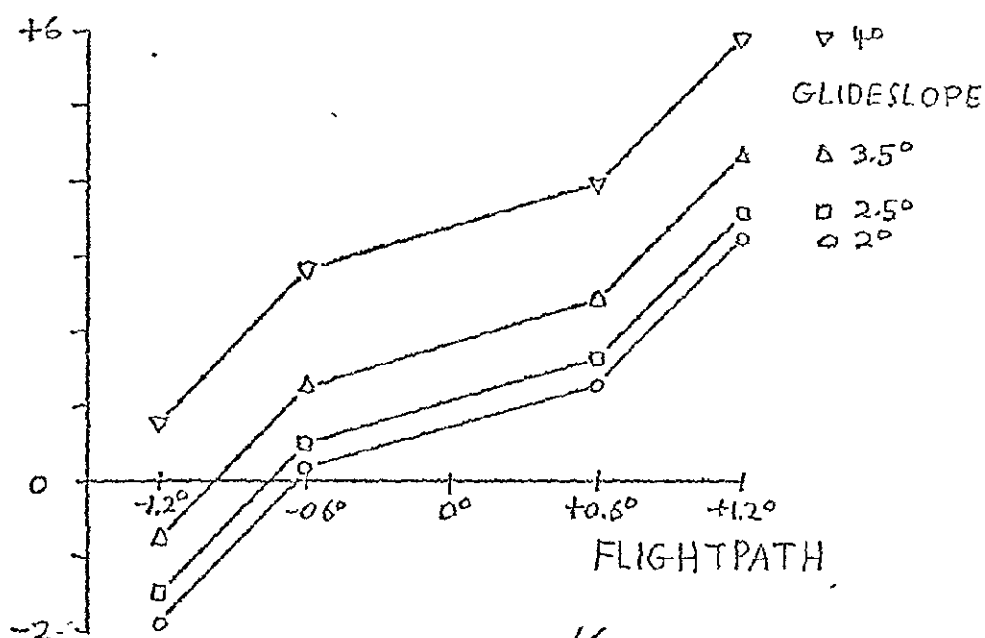
FLIGHT PATH   RESPONSES

DISTANCE = 6000 ft

DISTANCE = 3000 ft.
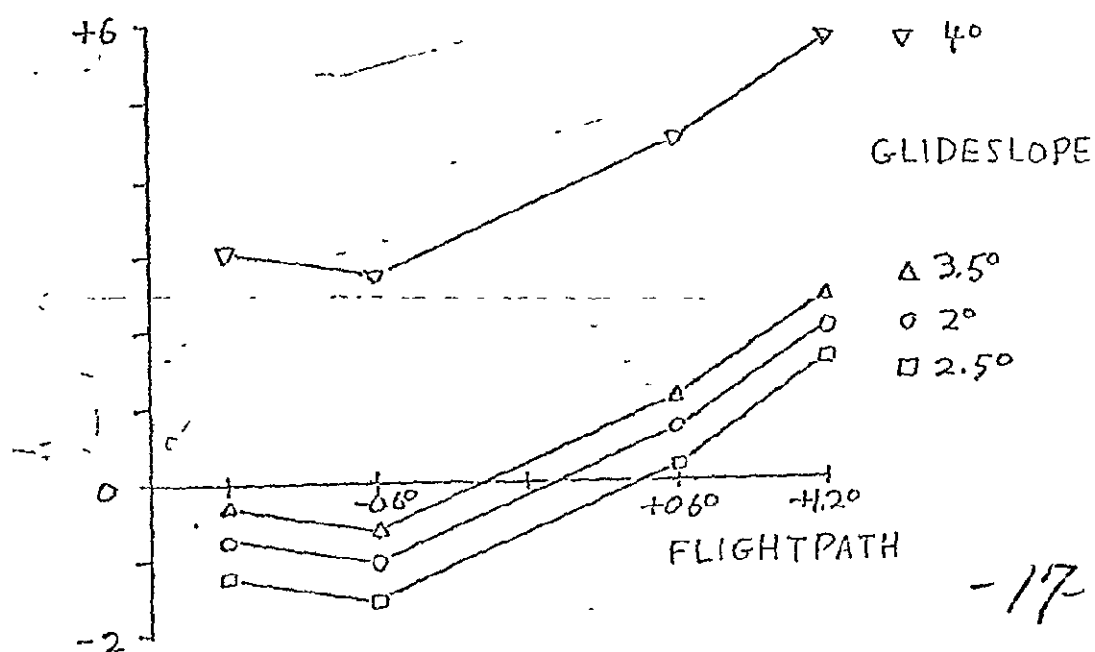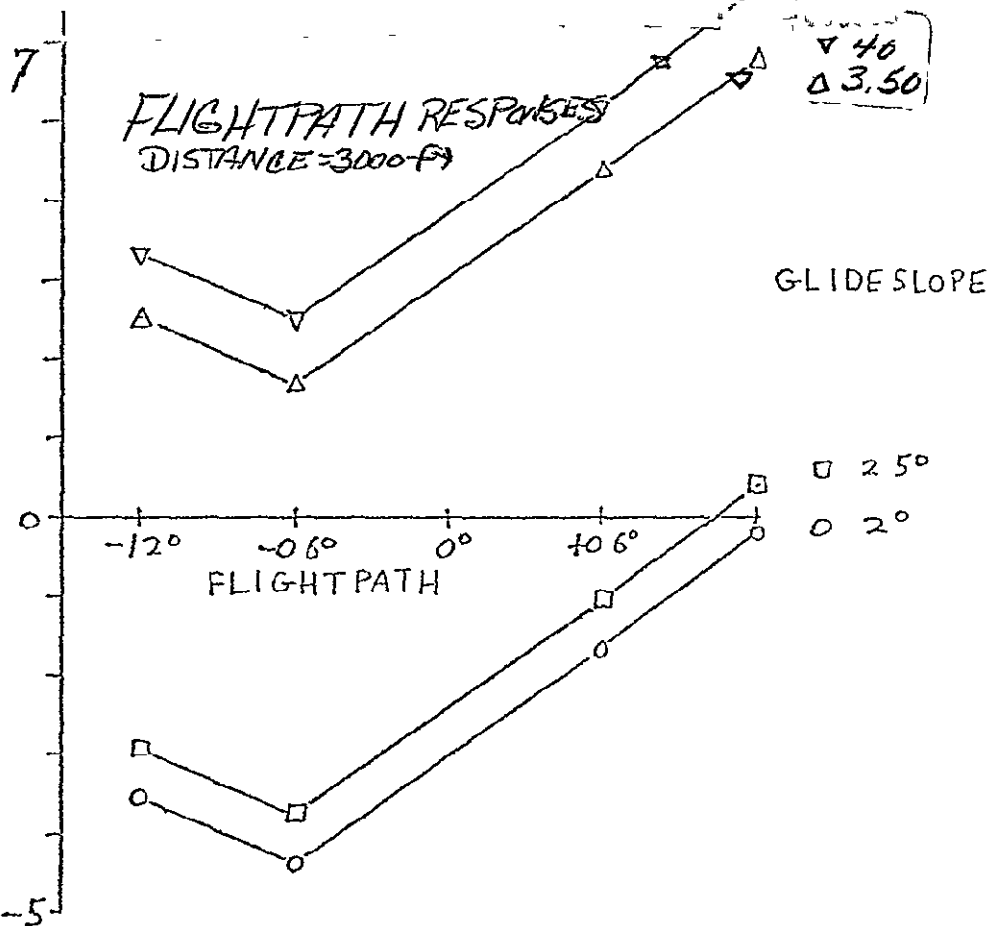
-17

FLIGHTPATH RESPONSES
DISTANCE = 3000 ft
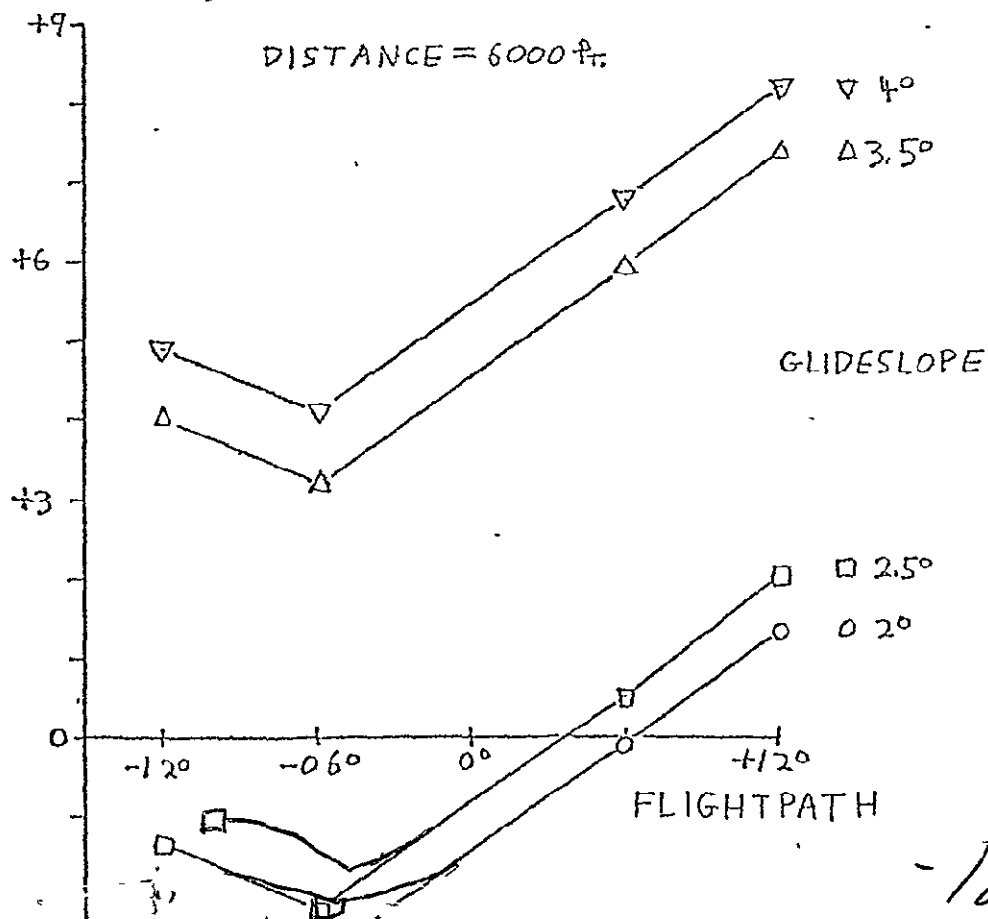
GLIDESLOPE
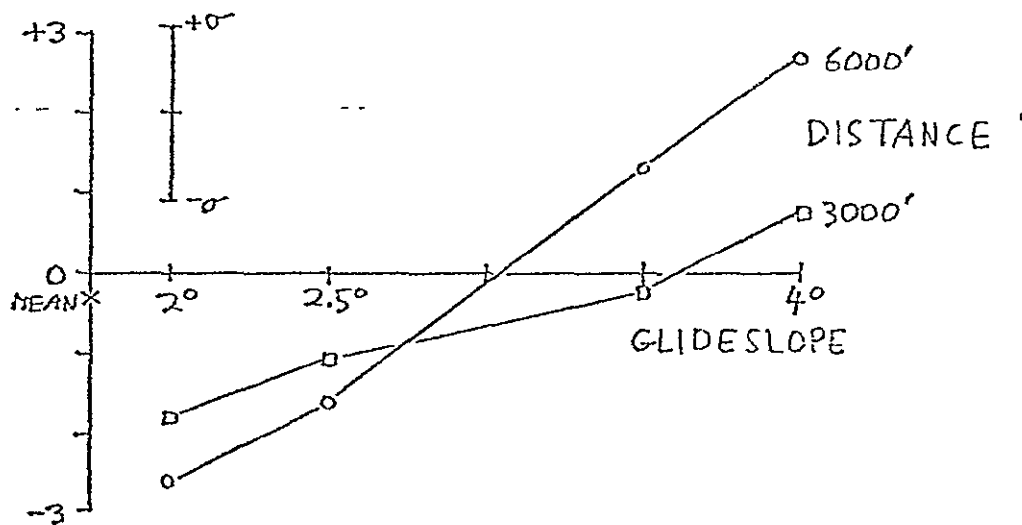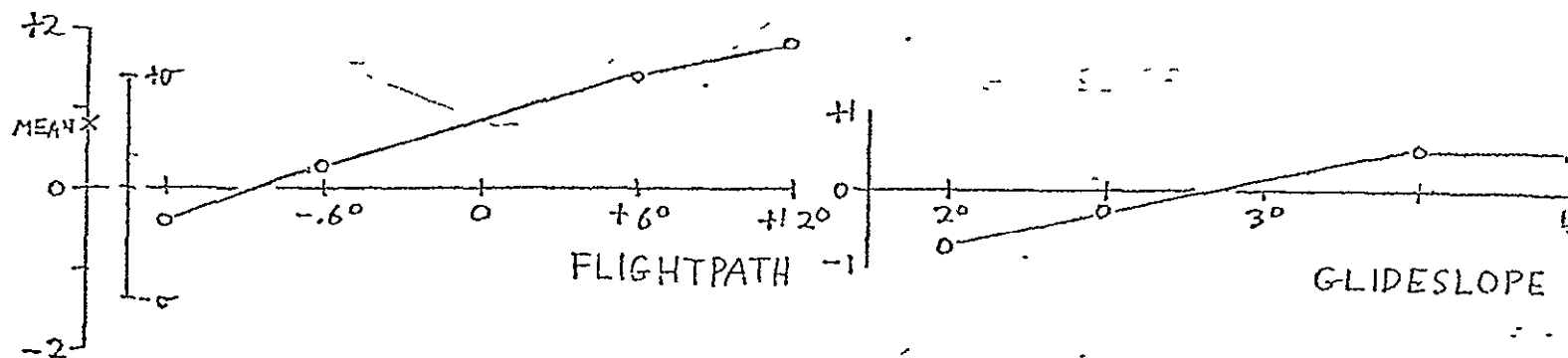
∇ 4°
△ 3.50

□ 2 5°
○ 2°

7

0

-5

-12°   -06°   0°   +06°

FLIGHTPATH

DISTANCE = 6000 ft.

+9

∇ 4°
△ 3.5°

GLIDESLOPE

+6

□ 2.5°
○ 2°

+3

0

-12°   -06°   0°   +12°

FLIGHTPATH

-18-

GLIDESLOPE RESPONSE

FLIGHT PATH RESPONSE

19

COMPARISON OF LINEAR AND NONLINEAR WASHOUT FILTERS USING

A MODEL OF THE HUMAN VESTIBULAR SYSTEM

The purpose of this portion of the research is to

discover what information the model of the human vestibular

system can give about the effects of washout filters on a

pilot's perception of motion. A qualitative evalutation of

linear versus non-linear washout filters as used in an air-

craft simulator shows that the non-linear filter provides a

"better" representation of actual motion than the linear

filter. This subjective pilot response seems to be due pri-

marily to the fact that the non-linear filter eliminates the

false rotational rate cues presented by the linear filter.

Hopefully, the model of the vestibular system will allow

more objective results to replace the rating of "better",

thereby providing a more quantitative method for predicting

simulator performance.

The model of the vestibular system, in its present form

as developed in the Man-Vehicle Laboratory, exists as a FORTRAN

program with a very limited input/output format. The data, as

20

recorded during the subjective tests at Langley, does not con-
form to that format, so the following changes are being made
to that program:

(1)   The program must, for convenience, run on the
        Laboratory's PDP 11/34. Since it was previously
        run on the IBM 370, this requires only a few
        modifications to the code. These changes were
        made and the program is now operational on the
        PDP 11/34.

(2)   The input format must be made more flexible,
        not only for the sake of this project, but for
        future projects as well. The program is in-
        flexible mainly because the state transition
        matrices and Kalman gain matrices are pre-
        calculated for a state transition matrix update
        interval of 0.1 second and a Kalman filter update
        interval of 1 second. If different update inter-
        vals are desired, these matrix values must be
        recalculated before the program is used.

        This continued recalculation doesn't make much
        sense in light of the new uses of the program.
        Therefore, the program will be changed to accept
        as input the two update intervals. Then the
        program would calculate the matrix values and

proceed as before. In order to accomplish this, it is necessary to determine how these matrix values were first calculated. Then a subroutine must be added to the program to calculate the values, given the update intervals. This has been completed.

(3)   The output, in its present form, consists of pages and pages of data describing the various responses of the vestibular system. Since the PDP 11/34 is equipped with a wide variety of graphics capabilities, it is desirable to display this data on graphs, rather than by hand plotting of the printed data. This part of the conversion is not yet complete.

Once the graphics changes are made to the program, it will be ready to interface with the data, and the analysis of the results can begin.

VISUAL-VESTIBULAR INTERACTIONS (YAW AXIS)

Effort during this reporting period has concentrated on modelling rotational motion sensation dependence on visual and vestibular cues, with exclusive concentration on yaw rotation about an earth-vertical axis. The primary results discussed below include. a) the proposal of a velocity drift model which helps explain low frequency drift observed during certain visual field presentations; b) a parallel channel visual-vestibular model which extends the earlier results obtained from combined input experiments; c) a human operator model appropriate to the velocity nulling task used to measure sensations; and d) a remnant correction technique useful for obtaining a more accurate estimate of the human operator's linear characteristics.

This progress report is divided into 7 sections. Sections 1 and 2 discuss velocity drift results obtained in a velocity nulling experiment obtained under two different visual field presentations: a field fixed with respect to the observer, and one moving at constant velocity with respect to the observer. Section 3 then presents some very simple functional models consistent with this observed drift behavior. To extend the visual-vestibular model reported on in the May progress report, section 4 proposes and describes a dual-input parallel channel model, and develops the equations necessary to extract the model characteristics from the experimental data. Section 5 describes some of the results obtained from a dual-input velocity nulling experiment, and presents Bode plots defining the human operator's combined controller/

23

estimator describing functions, appropriate to a parallel channel

structure. Section 6 then proposes how the control portion of the

operator's transfer function can be divided out of the dual-input

results, and section 7 presents various estimates of the inferred

estimator describing functions resulting from such an approach.

1.0   VELOCITY DRIFT WITH A FIXED VISUAL FIELD

Review of previous data obtained from the first two series of
closed-loop velocity nulling experiments and the results from a third
series of similar experiments suggest that the velocity drift charac-
teristics reported in the May progress report be amended. Specifically,
it should be noted that:

a.   The latencies and dual ramp drift characteristics illustrated
in figure 2C of the May progress report should be discounted, since they
may simply be an artifact of the drift measurement technique applied to
the strip chart histories. It has been found that computed values are too
sensitive to slight variations in fitting the data in a piecewise linear
manner. A more conservative approach has since been taken, in which only
one straight line is used to approximate the drift rate resulting from
each fixed field presentation Such an approach is considerably less
sensitive to variations in the fitting procedure, and has been reapplied
to all of the presentations obtained in the second series of experiments.

b.   The drift rate statistics given in figure 2C of the May progress
report should also be discounted, since they were obtained by pooling the
results of a relatively well-controlled experimental series (Series II)
with those of a pilot series (Series I), and the latter did not incorporate
an adequate balance for presentation order, fatigue, and learning the task.

The results presented here were obtained from two experimental series.
One has already been described in the May report (series II) and was the
source of the describing function (DF) data presented there. It suffices

25

to note here that the subject used a spring-centered stick for subject control of velocity. The other series (series III) was a duplicate, except that a control wheel affording no centering cues was substituted for the stick. Thus, the effect of possible centering cues could be investigated by comparing the results of the two experimental series. Both experiments were properly balanced as to the order of stimulus presentation, and the drift measurements were obtained by using a single straight line to fit the data.

Both series used the same six subjects: four received 2 FIX presentations (that is, a presentation of a visual field fixed with respect to the subject, lasting 128 seconds), and two subjects received 3 FIX presentations. Thus, in each series, there were 14 opportunities to observe possible velocity drift in the subject responses.

In the first series using the control stick, there were 8 instances of observed drift, and 6 no responses (NR) observed, within the accuracy afforded by the strip chart recording. Counting each NR as a $\overline{0.0^{o}/s^{2}}$ drift rate, the population statistics are given by.

$$\text{Stick control:} \quad \mu_1 = 0.004^{o}/s^{2}; \quad \sigma_1 = 0.041^{o}/s^{2}; \quad N_1 = 14 \qquad (1a)$$

A t-test shows that the mean μ_1 is not significantly different from zero ($p > 0.5$), which is what would be hoped for, since a significant non-zero mean would suggest a directional bias in the experimental equipment, procedure, and/or subject population.

We can now ask the following question. Is the self-centering property of the stick affecting the measured population response by providing a cue as to where the null is? Or, stated differently, are the subjects using the stick centering cue to augment their perception of the low-frequency motion cues?

26

With the experimental series repeated using the non-centering wheel as a control element (series III), there were again 14 opportunities to observe velocity drift. Actually observed were 13 cases of drift and one no response (NR). Again, counting the NR as a $0.0^{\circ}/s^2$ drift rate, the population statistics are given by:

$$\text{wheel control:} \quad \mu_2 = 0.015^{\circ}/s^2; \quad \sigma_2 = 0.050^{\circ}/s^2; \quad N_2 = 14 \qquad (1b)$$

As with stick control, a t-test shows that the mean drift rate is not significantly different from zero, suggesting the absence of a directional bias. Of more interest, however, is the question concerning a different population response due to wheel versus stick control. Comparing the statistics of (1a) with those of (1b), we find that an F-test on the variances shows them not to be significantly different ($p > 0.2$), so that we can pool them ($\sigma_p = 0.046^{\circ}/s^2$) and use a t-test on the means. We find that the means are also not significantly different ($p > 0.5$), so that this statistical measure shows no difference between wheel and stick control

Perhaps, however, this conclusion is biased by the fact that the NR's of each series were included to arrive at the means and variances of (1). By excluding them, and simply looking at the drift statistics of the responding population, we find the following:

$$\text{stick control:} \quad \mu_1 = 0.016; \quad \sigma_1 = 0.052; \quad N_1 = 8 \qquad (2a)$$

$$\text{wheel control:} \quad \mu_2 = 0.006; \quad \sigma_2 = 0.056; \quad N_2 = 13 \qquad (2b)$$

An F-test shows the variances to be not significantly different ($p > 0.2$), so that we can pool them ($\sigma_p = 0.054^{\circ}/s^2$) and use a t-test on the means.

27

Again, we find thatthe means are also not significantly different (p > 0.5) so that even excluding the NR's from the data, we find no significant difference between   wheel and stick control, by these measures.

What should be obvious at this point, however, is that the number of NR's observed with wheel control (1) is quite a bit smaller than the number observed with stick control (6). To test the significance   of this observation, we use a contingency table and the χ_0^2-test:

	Stick	Wheel
Drift occurred	8	13
No drift occurred	6	1

$\chi_0^2 = 4.76$
$\nu = 1$
$\left.\right\} \Rightarrow p < 0.05$

Thus, there is a significant difference between stick and wheel control, in terms of the number of times zero drift (NR) was observed. The suggestion is that the stick provides centering information which completely suppresses drift in some cases, although the average drift rate is independent of the type of control used.

Since the statistical tests done above on the means and variances of the drift rates showed no significant differences between stick and wheel control, it seems reasonable to pool the data. Of interest, then, is the manner in which the NR's are handled. If we assume the one NR observed with wheel control is a legitimate case of zero drift, uncorrupted by a controller centering cue, then we are obliged to include it in the population results. This is not unreasonable since it seems safe to assume that no controller centering cues were possible with the wheel control.

Turning now to the NR's observed with stick control, one approach
is to simply exclude them all, on the basis of possible response cor-
ruption due to centering cues. The corresponding contingency table
test results in a χ_0^2 value of 0.39, a considerable reduction from the
4.76 value obtained above, and suggests that this is the proper direction
in which to proceed. Including only one of the NR's observed during stick
control results in a χ_0^2 value of 0.11, and including two NR's results in
a χ_0^2 value of 0.88. Including additional NR's only increases the χ_0^2
value, thus, the minimum χ_0^2 value is obtained with one NR included in
the stick responses.

For the results of the two experimental series to be most congruent,
in terms of NR occurances, it is clear that a contingency table test should
result in a minimum χ_0^2 value. Thus, the decision may be made to eliminate
5 of the 6 NR's obtained under stick control. When the data is so edited,
keeping one NR from each series, the following statistics result:

$$\text{Drift rate:} \quad \mu = 0.011^\circ/s^2; \quad \sigma = 0.050^\circ/s^2, \quad N = 23 \qquad (3)$$

A t-test shows the mean to be not significantly different from zero (p > 0.5),
as expected.

To gain an appreciation for the magnitude of the drift rates observed
under fixed-field presentations, we can look at the statistics of the
absolute values of the pooled stick/wheel data.

$$\text{Drift rate (magnitude):} \quad \mu = 0.043^\circ/s^2; \quad \sigma = 0.027^\circ/s^2; \quad N = 23 \qquad (4)$$

These drift rate magnitudes are well below accepted threshold values for
yaw axis earth-vertical rotation ($\simeq 0.10^\circ/s^2$) and thus are consistent with the

29

notion that the subject is completely unaware of his drift acceleration
when deprived of visual motion cues.

A summary of the above results is presented in Figure 1.

A final note concerning the statistical characteristics of the
velocity drift rates concerns the normality of the pooled data. Shown
in Figure 2 is the cumulative frequency distribution (CFD) of the drift
rates normalized with respect to the mean and variance of (4); super-
imposed on this experimentally derived curve is the CFD for the unit
normal distribution, $N(0,1)$. Use of Kolmogorov-Smirnov test for normality
strongly rejects non-normality, so that it is not unreasonable to conclude
that velocity drift rates, caused by visual motion cue deprivation, are
normally distributed. This will be contrasted to the results presented
below, concerning drift rate distribution observed with subject performance
during presentation of a constant velocity (CV) visual field.

A functional model of angular velocity perception incorporating
the above-discussed drift characteristics will be presented in a later
section, after discussion of the CV results.

FIGURE 1 : <u>VELOCITY DRIFT WITH NO VISUAL CUES</u>
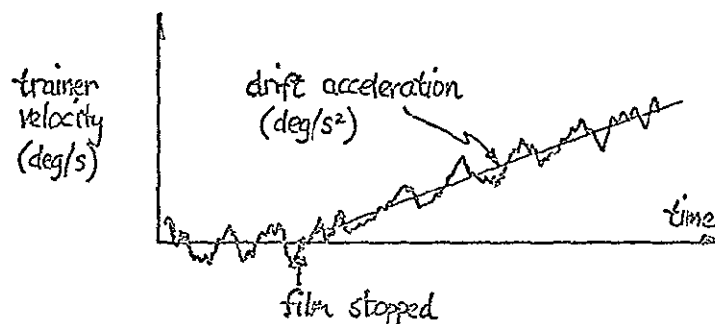
- SIX SUBJECTS, 14 FIXED FIELD PRESENTATIONS OVERALL,
  TWO CONTROL METHODS

CONTROL METHOD	DRIFT OCCURANCES	$\bar{x}$ $(^{\circ}/s^2)$	σ $(^{\circ}/s^2)$
STICK	8	.016	.052
WHEEL	13	.006	.056

- ONLY SIGNIFICANT DIFFERENCE BETWEEN METHODS IS IN NUMBER
  OF DRIFT OCCURANCES. STICK PROVIDES A CENTERING CUE

- POOLED DATA.

  $\bar{x}$ = .011 $^{\circ}/s^2$ σ = .050$^{\circ}/s^2$ N = 23

  NOT SIGNIFICANTLY DIFFERENT FROM ZERO. BALANCED.

- DRIFT MAGNITUDES:

  $\overline{|x|}$ = .043 $^{\circ}/s^2$ σ = .027 $^{\circ}/s^2$ N = 23

  WELL BELOW THRESHOLD
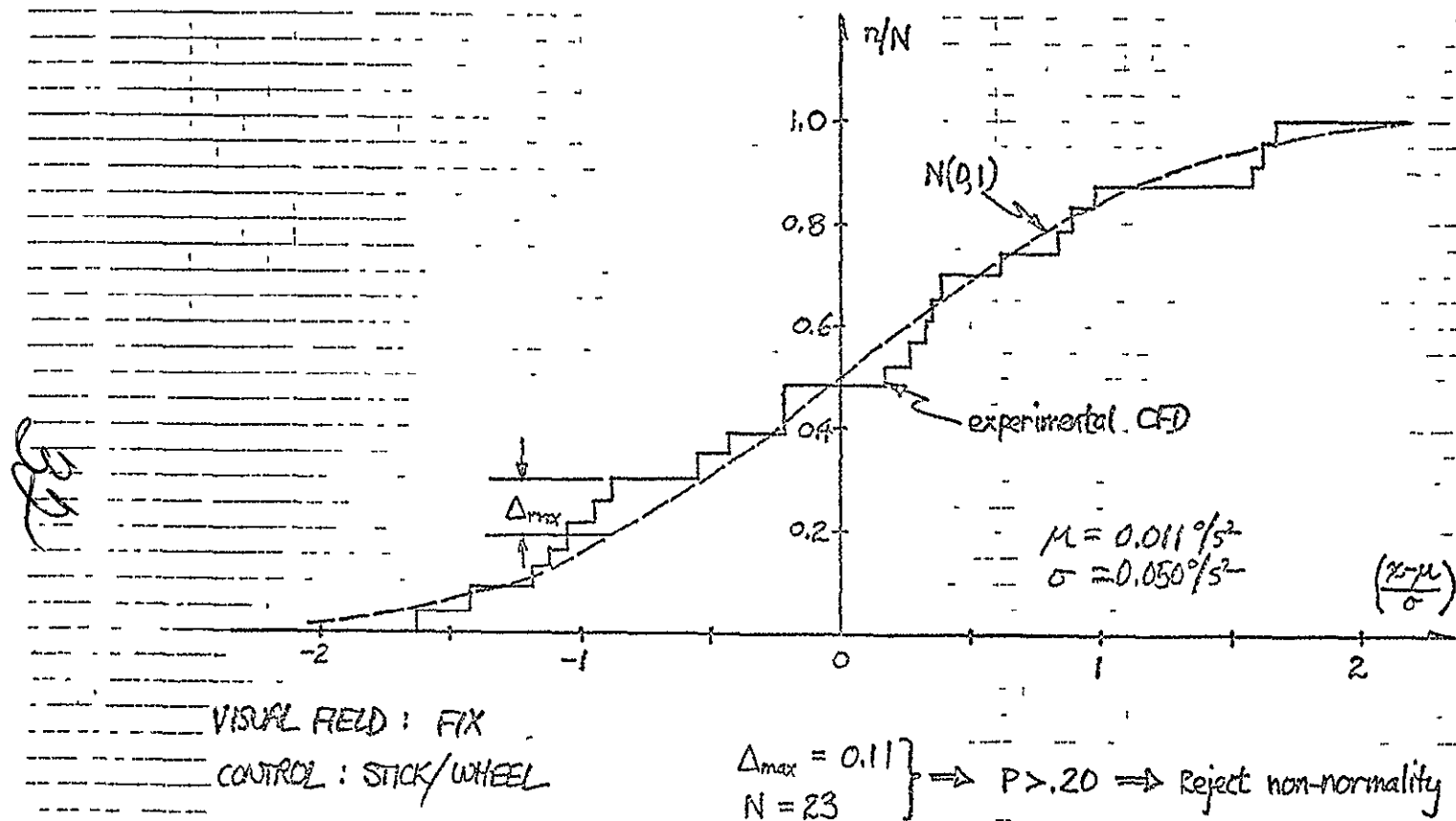
FIG 2 : Cumulative Frequency Distribution for Velocity Drift Rates — Fixed Visual Field

VISUAL FIELD : FIX
CONTROL : STICK/WHEEL

$\Delta_{max} = 0.11$ } $\Rightarrow$ P > .20 $\Rightarrow$ Reject non-normality
$N = 23$

On the figure:
- n/N (vertical axis)
- N(0,1)
- experimental CFD
- Δ_{max}
- $\mu = 0.011\,°/s^2$
- $\sigma = 0.050\,°/s^2$
- $\left(\frac{x-\mu}{\sigma}\right)$
- axis values: -2, -1, 0, 1, 2
- vertical values: 0.2, 0.4, 0.6, 0.8, 1.0

2.0   VELOCITY DRIFT WITH A CONSTANT VELOCITY VISUAL FIELD

The effect of a constant velocity (CV) visual field presentation on subject performance in the closed-loop velocity-nulling task has already been qualitatively described in the May progress report. Briefly, it was found that relatively large velocity drifts were observed during such presentations, and that drift always was in the direction of visual field motion. Given below is a more quantitative description of these drift responses.

During the course of the previously-described velocity-nulling task, a constant velocity ($4°/s$) right-moving peripheral visual field was presented to the subject. Velocity drift measurements were made on the ensuing subject responses, using the single straight line fit noted in the previous section. As in the case of fixed visual field presentations, two series were run: one using self-centering stick control (series II) and the other using wheel control (series III).

Both series used the same six subjects. four received 2 CV presentations (that is, a presentation of a visual field moving at a constant velocity with respect to the subject), and two received 3 CV presentations. As with the FIX presentations, there were thus 14 opportunities per series to observe possible velocity drift in the subject responses.

Out of a total possible 28 occurences of drift, there were observed 27, with one case of severe disorientation and subsequent inconsistent and task-unrelated response. This case has been eliminated from the data base whose statistics are given below:

33

stick control: $\mu_1 = 0.261^\circ/s^2$; $\sigma_1 = 0.141^\circ/s^2$; $N_1 = 14$ (1a)

wheel control: $\mu_2 = 0.328^\circ/s^2$; $\sigma_2 = 0.265^\circ/s^2$; $N_2 = 13$ (1b)

As in the preceeding section, we can ask if stick control results in significantly different subject responses from those seen with wheel control. It should be clear that they are equivalent in terms of not suppressing drift responses, this in contrast to the large numbers of NR's seen with stick control and a fixed visual field presentation as noted in the preceeding section. What remains then is to compare the statistical measures above.

Comparing the statistics of (1a) with (1b), an F-test on the variances shows them to be significantly different ($p < 0.05$). A Welch t-test, however, shows that the means are not significantly different ($p > 0.5$), and one is thus motivated to pool the data for the two control methods, in spite of the variance differences. The pooled data for CV presentation velocity drift rates are then characterized by the following statistics.

drift rate(CV): $\mu = 0.293^\circ/s^2$; $\sigma = 0.209^\circ/s^2$; $N = 27$ (2)

It should be recalled that since all of the observed drifts were in the same direction (following the direction of the visual field motion), these statistics also apply to drift rate magnitudes. It is also appropriate to recall that these statistics apply to the single stimulus magnitude of a $4^\circ/s$ right moving visual field.

A simple t-test on the pooled statistics of (2) show the mean drift rate to be significantly different from zero ($p < 0.005$); this is to be contrasted to the approximately zero drift rate seen across the population in response to a fixed-field presentation. Further contrast between the

responses to the two visual field environments is provided by comparing drift rate magnitudes. From (4) of the previous section, fixed-field drift was characterized by:

Drift rate magnitude (FIX)· $\mu = 0.043^{\circ}/s^2$; $\sigma = 0.027^{\circ}/s^2$, N = 23   (3)

An F-test on the variances of (2) and (3) above show a highly significant difference ($p < 0.001$), as does a Welch t-test on the means ($p < 0.005$) Thus we are led to conclude that drift rate magnitudes resulting from a CV visual field presentation are significantly different from those seen during a FIX presentation.

Also of interest is the fact that the mean CV drift rate of approximately $0.3^{\circ}/s^2$ is near three times the accepted yaw axis earth-vertical rotational acceleration threshold, suggesting a strong modulation of "vestibular" thresholds by visual inputs. A qualitative discussion of how such a drift rate can arise and remain undetected by the subject is given in the May progress report; a slightly more quantitative functional model is presented in the next section.

A summary of the above findings is presented in Figure 1

A final note concerning the statistical characteristics of the velocity drift rates concerns the normality of the pooled data. Shown in Figure 2 is the cumulative frequency distribution (CFD) of the drift rates normalized with respect to the mean and variance of (2), presented in the same format used previously for the FIX drift rates. As before, use of the Kolmogorov-Smirnov test for normality requires us to reject non-normality ($p > 0.2$). Comparing this figure with the one drawn for the FIX drift rates (Figure 2, last section), however, suggests that the CV drift data is "less normal", because of the late rise and slow tail off

FIGURE 1 : <u>VELOCITY DRIFT WITH CONSTANT VELOCITY VISUAL FIELD</u>

- SIX SUBJECTS, 14 CV FIELD PRESENTATIONS OVERALL, TWO CONTROL METHODS

CONTROL METHOD	DRIFT OCCURANCES	$\bar{x}$ (°/s²)	σ (°/s²)
STICK	13[*]	.261	.141
WHEEL	14	.328	.265

*one severe disorientation eliminated from talley

- SIGNIFICANT DIFFERENCE BETWEEN TWO METHODS IN VARIANCE, NOT MEANS

- POOLED DATA·

$$\tilde{x} = 0.293 \ °/s^2 \quad \sigma = 0.209 \ °/s^2 \quad N = 27$$

- MEAN SIGNIFICANTLY DIFFERENT FROM ZERO (P<.005), AND ABOVE THRESHOLD ($\sim 0.1 \ °/s^2$)

- RESULTS SIGNIFICANTLY DIFFERENT FROM FIX PRESENTATIONS

- DATA BEST FIT WITH A LOG-NORMAL DISTRIBUTION MAGNITUDE ESTIMATE IMPLICATIONS ???

36

FIGURE 2 : Cumulative Frequency Distribution for Velocity Drift Rates — Constant Velocity Visual Field

of the CFD. We are thus motivated to look at the log of the data, and
the normalized CFD is plotted in Figure 3. Comparing this with that of
Figure 2 shows that the CV drift rate is more accurately described as a
log=normal random variable, rather than a normal random variable. How
this is to be interpreted is, at present, unclear, although it may sug-
gest that some Weber law estimation process is at work within each in-
dividual's response, and is somehow reflected across the population
response.

FIGURE 3: Cumulative Frequency Distribution for Log (Velocity Drift Rate) — Constant Velocity Visual Field

In the figure:

$$y = \log_{10}(\text{drift rate})$$
$$\mu_y = -0.615$$
$$\sigma_y = 0.267$$

Axis label: $\left(\dfrac{y - \mu_y}{\sigma_y}\right)$

Vertical axis: n/N
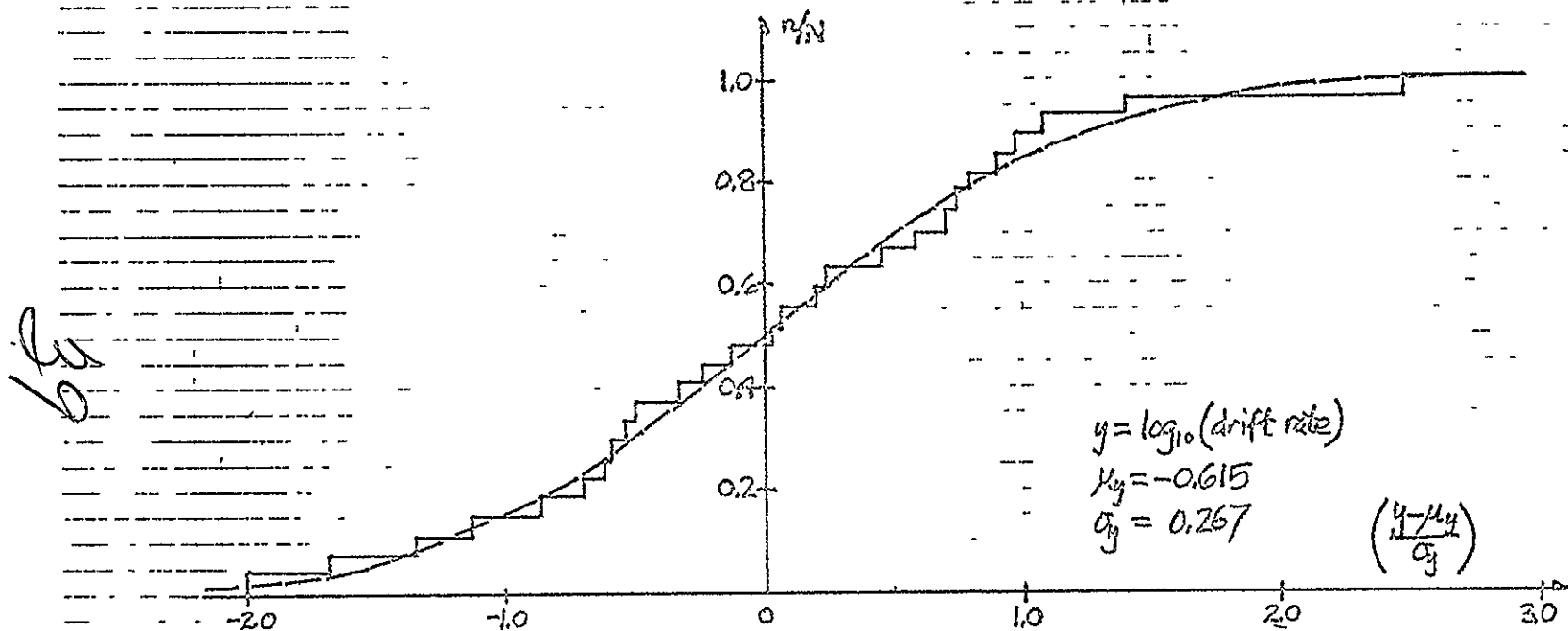
VISUAL FIELD : CV

CONTROL : STICK/WHEEL

3.0   VELOCITY DRIFT MODELS

The previous two sections have discussed the statistical charac-
teristics of velocity drift incurred by subjects during the task of
closed-loop velocity nulling, when presented with two types of visual
motion cues. This section will now present very simple functional
models of the human operator which are consistent with the observed
drift behavior.

3.1   Fixed Visual Field

As discussed in the May progress report, past investigators have
-attributed velocity drift arising out of a velocity nulling experiment
(with visual motion cue deprivation) to be a characteristic primarily
associated with the vestibular sensory channels. Functionally, this
is an appealing interpretation because a very simple model can be
constructed which is consistent with the observed drift and with the
generally accepted properties of the vestibular sensors. Shown in
Figure 1 is such a model. a bilateral model of the two horizontal
semicircular canals, whose outputs are differenced to provide an estimate
of head angular velocity. Note that both canals are characterized as
identical linear bandpass filters on velocity, but differing in DC gain
and output bias.

Shortly it will be shown that a simple constant offset in the
estimate $\hat{\omega}$ is sufficient to give rise to the drift behavior seen in the
experiments. In particular, if a non-zero estimate $\hat{\omega}$ can be generated
by the model of Figure 1, in the face of an angular velocity ω which is
actually zero, then it is a fairly direct matter to predict velocity drift
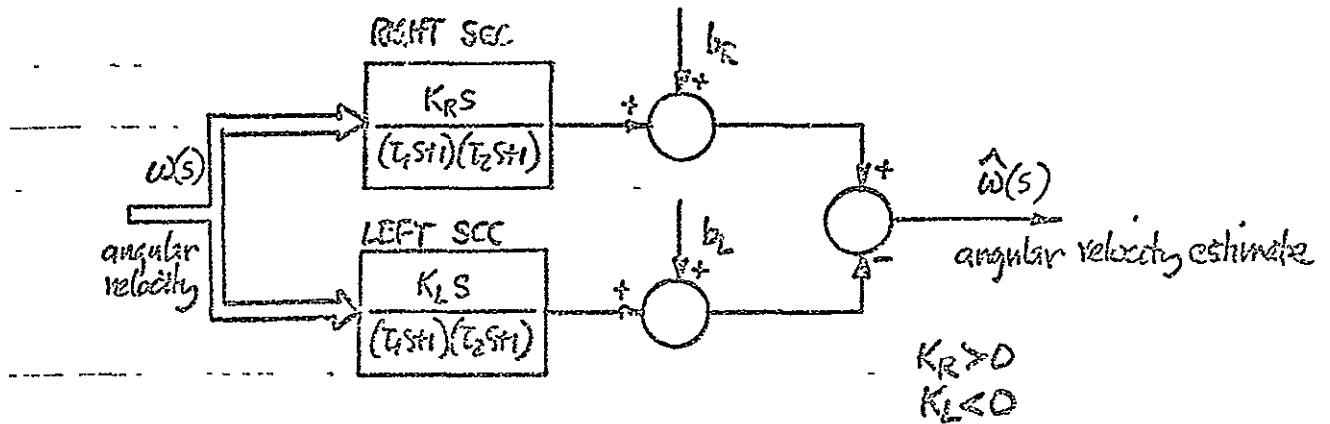in the closed-loop velocity nulling task. Of interest now is to see how
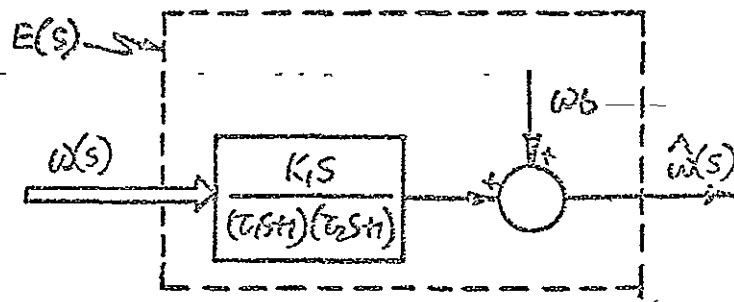
FIGURE 1: Bilateral Vestibular Model, with Output Biases

FIGURE 2: Cyclopean Vestibular Model, with Output Bias

an offset can arise from a model parameter imbalance. . From the figure,
the angular velocity estimate is given by.

$$\hat{\omega}(s) = (b_R - b_L) + \frac{(K_R - K_L)s}{(\tau_1 s+1)(\tau_2 s+1)} \omega(s) \qquad (1)$$

It should be clear that if the bias terms are equal ($b_R = b_L$), then a gain
imbalance ($K_R \neq -K_L$) is __not__ sufficient to provide a non-zero $\hat{\omega}$ when ω is
actually zero. Neither is it necessary, since a non-zero $\hat{\omega}$ can be simply
obtained when ω is zero by having the biases unequal ($b_R \neq b_L$). Thus a
gain imbalance is irrelevant to a discussion of a steady offset in the
velocity estimate, and for simiplicity we can assume a gain balance:

$$K_R = -K_L \equiv K_1/2 \qquad (2)$$

so that (1) simplifies to the standard "cyclopean" canal model, with
bias:

$$\hat{\omega}(s) = \omega_b(s) + \frac{K_1 s}{(\tau_1 s+1)(\tau_2 s+1)} \omega(s) \qquad / \qquad (3)$$

where the bias velocity is defined by

$$\omega_b = b_R - b_L \qquad (4)$$

The functional model corresponding to (3) and (4) is sketched in
Figure 2, and will be used in the sequel.

Now to show how such an angular velocity bias can give rise to
the drift observed in the velocity nulling task, it is necessary to
refer to the loop diagram previously presented in the May progress
report and repeated in Figure 3. Since we are presently considering
the purely vestibular situation, in which the subject is presented

43

FIGURE 3 : Velocity Nulling Task Loop Diagram .
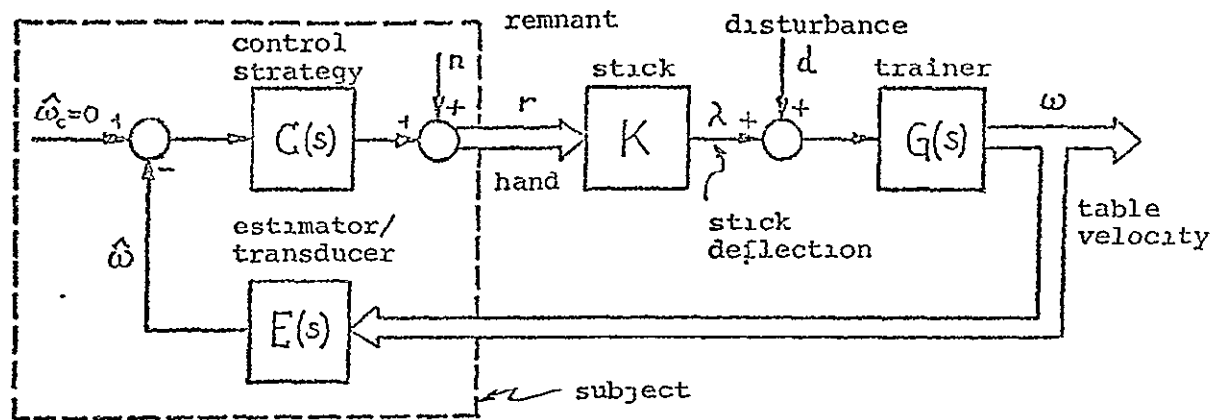
Feedback path control:

43
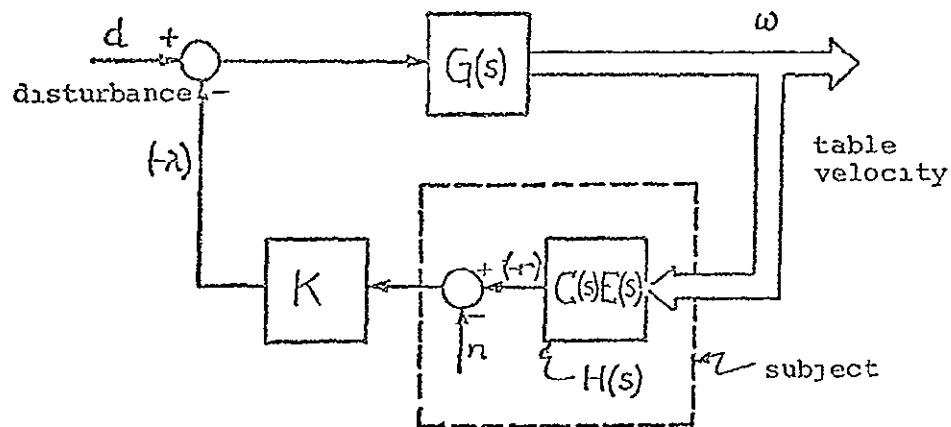
with a stationary visual surround, the estimator block E(s) can be
replaced by the vestibular model of Figure 2. Furthermore, as will be
discussed at greater length in section 6, the control strategy
C(s) can be approximated by an integrator with gain, or:

$$C(s) = K_c/s \tag{5}$$

Simple block diagram arithmetic then yields the following expression
for the angular velocity, ω, resulting from the subject's remnant, n,
his vestibular bias, ω_b, and the input disturbance, d:

$$\omega(s) = \frac{G}{1+KGCE'} \{Kn - KC\omega_b + d\} \tag{6}$$

where E' is the linear portion of the vestibular estimator:

$$E'(s) \equiv K_1 s/\{(\tau_1 s+1)(\tau_2 s+1)\} \tag{7}$$

Since we are interested in low-frequency behavior (specifically, drift),
we note that·

$$\lim_{s \to 0} E'(s) = K_1 s \tag{8a}$$

Further, the trainer transfer function is unity at DC, so that

$$\lim_{s \to 0} G(s) = 1 \tag{8b}$$

Since the disturbance d(t) is a sum of sinusoids (as described in the May
progress report),

$$\lim_{s \to 0} d(s) = 0 \tag{8c}$$

Finally, if we assume the remnant to have no power at zero frequency, then

$$\lim_{s \to 0} n(s) = 0 \tag{8d}$$

44

Substituting (5) and (8) into (6), we find the low frequency portion of
the angular velocity signal to be given by:

$$\lim_{s \to 0} \omega(s) = \lim_{s \to 0} \left(\frac{-KK_c}{1+KK_cK_1} \right) \frac{\omega_b}{s^2} \tag{9'}$$

where we have used the fact that the bias ω_b is a constant over time,
so that

$$\omega_b(s) = \omega_b/s \tag{8e}$$

In the time domain, then, (9') implies that, due to the velocity estimate
bias ω_b, the subject will continue to accelerate at a constant rate, his
angular velocity being given by:

$$\omega(t) = - \frac{KK_c}{1+KK_cK_1} \omega_b t \qquad \text{(FIX \quad Drift)} \tag{10}$$

assuming zero initial conditions. The minus sign, of course, implies
that a positive (rightward) bias will give rise to a negative (leftward)
drift. Thus, the simple cyclopean vestibular model, modified with the
addition of a bias on the output, appears to be an adequate descriptor
of subject performance when one is deprived of visual motion cues on the
velocity nulling task.

Presumably, the estimator bias ω_b for an individual could be inferred
from (10) by measuring the drift acceleration and by estimating the indi-
vidual transfer function gains K, K_c and K_1. The same could be done for
the entire population, but it is simpler to recognize from (3) of section 1
that the average drift rate $\bar{\omega}$ is zero over the population. Thus, from
(10), the average velocity bias $\bar{\omega}_b$ over the population must also be zero,
since KK_c has always been found to be non-zero (see section 6). Estimation

45

of the variance of ω_b from drift rate measurements is, of course,

complicated by the unknown statistical properties of the gains in

(10).

One final qualitative aspect of this bias model is worth noting,

and concerns the subject's perceived velocity while engaged in the

velocity nulling task. His estimated velocity $\hat{\omega}$ is neither zero nor

ω_b, but an intermediate value found by substituting the transform of

(10) into the cyclopean canal model of (3), to yield:

$$\hat{\omega}_{LF}(s) = \lim_{s \to 0} \frac{\omega_b}{s} \{ 1 + \frac{K_1 s}{(\tau_1 s+1)(\tau_2 s+1)} \{ \frac{-KK_c}{1+KK_c K_1} \} \frac{1}{s} \}$$

where the subscript LF indicates that we are interested in the low

frequency portion of perceived velocity. The above expression simplifies

to yield the following relation between bias velocity and perceived

velocity:

$$\hat{\omega}_{LF} = \frac{1}{1+KK_c K_1} \omega_b \tag{11'}$$

Thus, the subject perceives that he is moving at a constant velocity,

and hence is obligated to provide a compensatory control stick deflection

to null it, thus leading to the eventual acceleration drift seen in the

records. Note that his perceived velocity $\hat{\omega}_{LF}$ is simply the bias velocity

attentuated by the closed loop gain, so that individuals with higher loop

gains will tend to have lower values of perceived velocity, and vice versa,

assuming other factors remain equal between subjects.

3.2 Constant Velocity Visual Field

To this point, we have been concerned with the drift incurred with

a fixed visual field (FIX); a similar argument can be made to help under-

stand the cause of drift under constant velocity visual field presentation (CV).

Shown in Figure 4 is perhaps the simplest possible parallel channel visual-vestibular model, in which it is presumed that visual surround velocity contributes only to the low frequency portion of the angular velocity estimate, in a linear manner. Some justification for this model has already been given in the May progress report; more will be given in a later section describing an experiment whose goal is to determine the components of such a parallel channel model. For now, it suffices to note that the velocity estimate from this model is given by:

$$\hat{\omega}(s) = \omega_b(s) + K_2\omega_2(s) + \frac{K_1 s}{(\tau_1 s+1)(\tau_2 s+1)} \omega_1(s) \qquad (12)$$

where ω_1 and ω_2 refer to vestibular and visual field velocities respectively. Note that by defining

$$\omega_b' \equiv \omega_b + K_2\omega_2 \qquad (13)$$

the equation is identical to (3), the biased estimator for the purely vestibular situation. Thus, the same low-frequency derivation is is applicable and (10) can be used to describe the CV-induced drift rates seen experimentally, with ω_b in the equation replaced by ω_b' above, or

$$\omega(t) = -\frac{KK_c}{1+KK_cK_1}(\omega_b + K_2\omega_2)t \qquad \text{(CV drift)} \qquad (14)$$
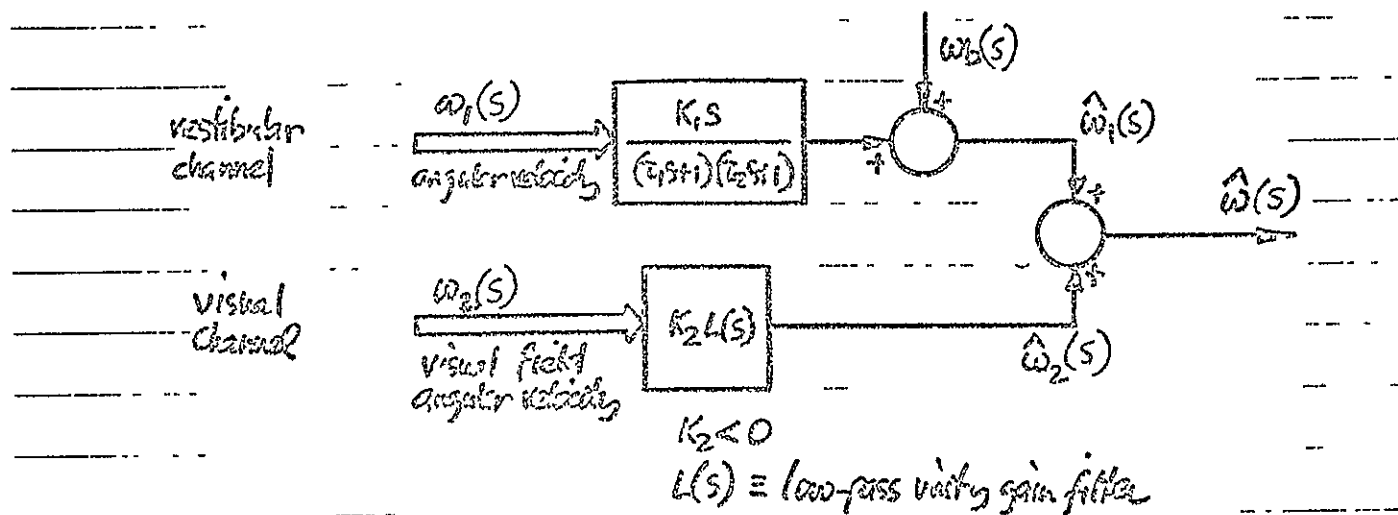
FIGURE 4: Parallel Channel Visual-Vestibular Velocity Estimator

In the previous section it was noted that all CV-induced drifts were observed to be in the same direction as the stimulus visual field velocity. What this suggests is that the visual field effect is large with respect to the (bilateral) vestibular offset term. This is seen fairly directly by recasting (10) and (14) in terms of drift acceleration levels:

$$\dot{\omega}_{FIX} = \Lambda\omega_b \qquad\qquad (a)$$

$$\tag{15}$$

$$\dot{\omega}_{CV} = \Lambda(\omega_b + K_2\omega_2) = \dot{\omega}_{FIX} + \Lambda K_2\omega_2 \qquad (b)$$

where Λ is defined by

$$\Lambda \equiv -\frac{KK_c}{1+KK_c K_1} \qquad\qquad (16)$$

But, from the previous two sections, the average drift accelerations were

$$\overline{\dot{\omega}}_{FIX} \simeq 0.04^\circ/s^2$$

$$\tag{17}$$

$$\overline{\dot{\omega}}_{CV} \simeq 0.29^\circ/s^2$$

So that inspection of (15b) would lead one to conclude that, over the population,

$$\omega_b << K_2\omega_2 \qquad\qquad (18)$$

that is, the vestibular bias velocity is small with respect to the CV-induced velocity sensation. It should be recognized that this conclusion is applicable to the particular value of ω_2 used in the experiment, a $4^\circ/s$ right-moving visual field, and lower field velocities may not allow similar conclusions to be made.

4.0   PARALLEL CHANNEL VISUAL-VESTIBULAR MODEL

The previously described velocity-nulling experiments (series I, II, and III) looked at closed-loop velocity control in the face of a vestibular disturbance combined with one of three types of visual surround environments: a counterrotating visual field (CON) which exactly confirmed vestibular inputs, a field stationary with respect to the subject (FIX) which provided no visual motion cues, and a field moving at constant velocity with respect to the subject (CV) which induced circularvection sensations.

The results, analyzed in both the time and frequency domain, support the notion of a frequency separation of visual and vestibular inputs, where the visual cues provide the steady state or low frequency cues, while the vestibular cues provide complementary high frequency or transient information. The human operator describing function was calculated for each of the three visual field conditions and was modelled as a lag-lead function whose parameters were dependent on the particular field condition (see May progress report).

The describing function itself relates actual trainer motion to the subject's control stick/wheel output, and thus can be viewed as a "vestibular" transfer function whose parameters depend on the parti- cular visual motion cues being presented to the subject. This, of course, assumes that the subject's control strategy for nulling per- ceived motion is essentially unity throughout the frequency range of interest; this subject will be addressed later in section 6.

50

In order to look more closely at what is essentially a dual-input problem, a parallel channel estimator model was proposed, and another experimental series (IV) was initiated to see if such a model could explain in greater detail how visual and vestibular inputs are combined to arrive at a sensation of motion. The approach is to work with two describing functions: one relating trainer velocity to wheel output, and the other relating visual field motion to wheel output.

In the previous three series, noise was injected into the trainer loop so that the subject would be obliged to provide compensatory stick or wheel deflections to null his perceived angular velocity. In the present dual-input (DI) series, noise is also injected into the visual field loop, so that any visually-induced motion sensation must also be compensated for by the subject. By choosing the two disturbances to be independent of one another, it is impossible for the subject to perform both nulling tasks at once. By examining the results in the frequency domain, it then becomes possible to see what components of the subject's response are due to vestibular inputs, and what are due to visual inputs. From this, one can infer a DI describing function model of perceived motion. From experience with the previous series, injecting noise into the trainer loop (vestibular path) is fairly straight forward: simply sum it with the subject's wheel signal prior to being sent to the trainer drive circuitry. The same approach can be taken for the projector loop (visual loop): sum a second noise signal with the wheel signal and send this combined signal to the projector drive circuitry.

A functional block diagram of the overall system, including a conjectural dual-input model of the human operator, is shown in Figure 1 . The two injected noise signals are denoted by d_1 and d_2, and the wheel signal λ is shown as an input to both the visual and vestibular loops For this series and others following, wheel control was used to avoid possible centering cues provided by the spring loaded stick. Two points should be noted First, the sign of the wheel signal is changed when it is sent to the projector drive, to make the resulting visual field motion consistent with the trainer motion. Thus, a right wheel motion results in a right trainer motion and a left visual field motion; i.e. analogous to the counter-rotating field situation of the previous three series. The second point to note is the addition of a prefilter, F_2, in the visual field path, necessary because the projector drive alone, G_2, has a relatively high bandpass compared to the bandpass of the filtered trainer transfer function, $F_1 G_1$ By choosing F_2 so that

$$F_1 G_1 = F_2 G_2 \quad (\equiv P)$$

then, in response to the subject's wheel deflections, the visual field motion will mimic the trainer motion, exhibiting the same amplitude attenuation and phase lag over the frequency regime of interest Another way of saying this, is, that, in the absence of any noise injected into either loop, the visual field motion, in response to the subject's wheel deflections, should be indistinguishable from the counterrotating visual field motion used in the previous experimental series. Thus, the pre-filter F_2 helps make the visual field a more compelling motion cue.

FIG 1 : DUAL-INPUT EXPERIMENT : FUNCTIONAL MODEL

note: $F_1 G_1 = F_2 G_2 \equiv P$
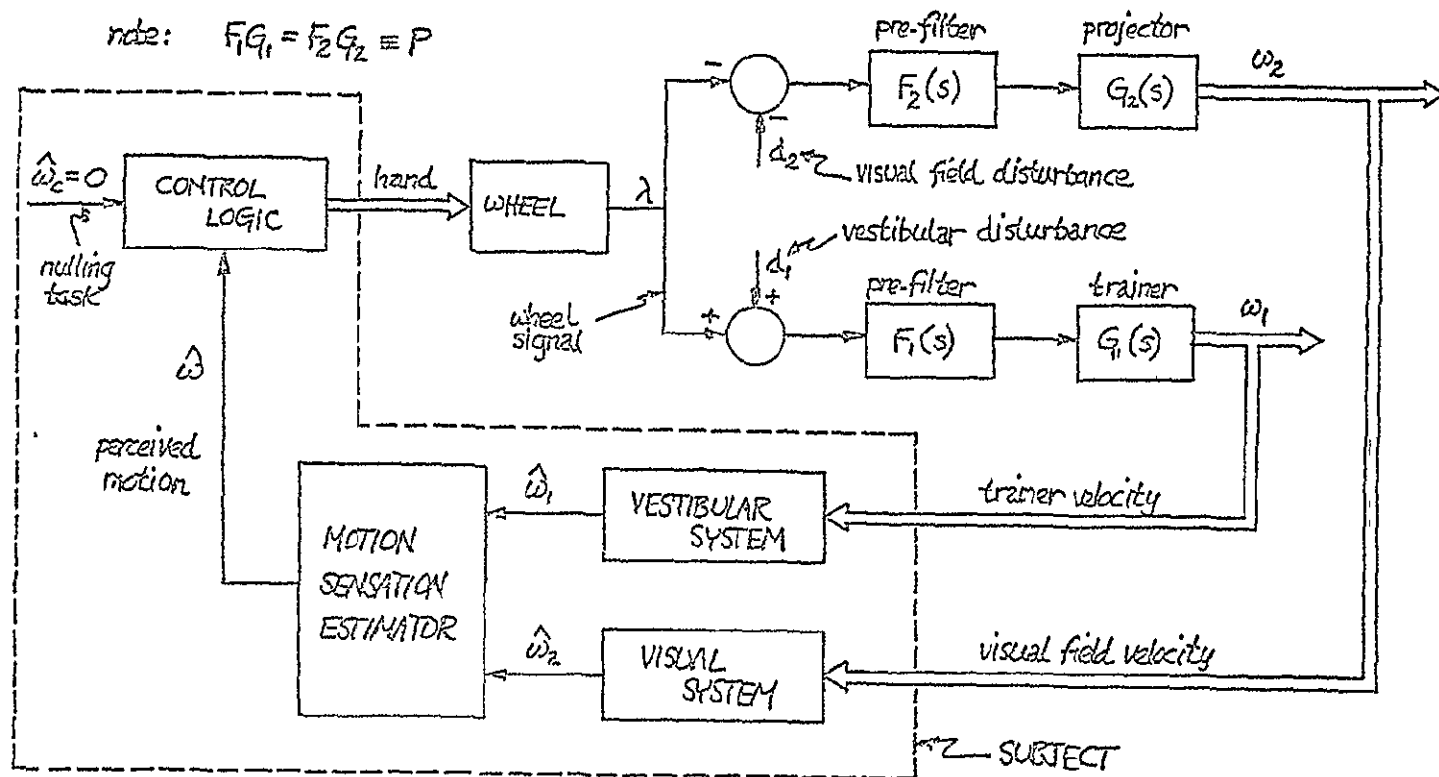
A linear model of the subject, interfaced with the experimental apparatus, is diagrammed in Figure 2. Here, it is assumed that the visual and vestibular channels work in parallel, with their outputs summed to provide an overall estimate of self-motion. This is the same approach used in the velocity drift modelling of section 3, but is to be contrasted with the single channel "vestibular" model, augmented by visually-induced parameter variations, derived from the results of the previously described experimental series. As before, an internal model of zero perceived velocity is assumed to be a set-point ($\hat{\omega}_c = 0$) upon which acts a linear control logic C(s) to generate the appropriate hand motion which drives the control wheel. A remnant signal provides for a source of subject output response which is uncorrelated with either of the disturbance inputs, d_1 and d_2.

The remainder of this section will now be concerned with the manner in which the estimator transfer functions E_1 and E_2 may be solved for in terms of the three loop inputs, d_1, d_2, and n, and the three loop outputs, ω_1, ω_2, and λ.

From block diagram algebra, it is a direct matter to show that the three outputs are determined by the three inputs in the following manner:

$$\lambda(s) = \frac{1}{\Delta}(Kn(s) + KPCE_1d_1(s) - KPCE_2d_2(s)) \qquad (a)$$

$$\omega_1(s) = \frac{P}{\Delta}(Kn(s) + (1 + KPCE_2)d_1(s) - KPCE_2d_2(s)) \qquad (b) \qquad (1)$$

$$\omega_2(s) = -\frac{P}{\Delta}(Kn(s) - KPCE_1d_1(s) + (1 + KPCE_1)d_2(s)) \qquad (c)$$

where

$$\Delta \equiv 1 + KPC(E_1 + E_2) \qquad (2)$$

54

FIGURE 2 : LINEARIZED SYSTEM, PARALLEL CHANNEL MODEL

note: $P = F_1 G_1 = F_2 G_2$
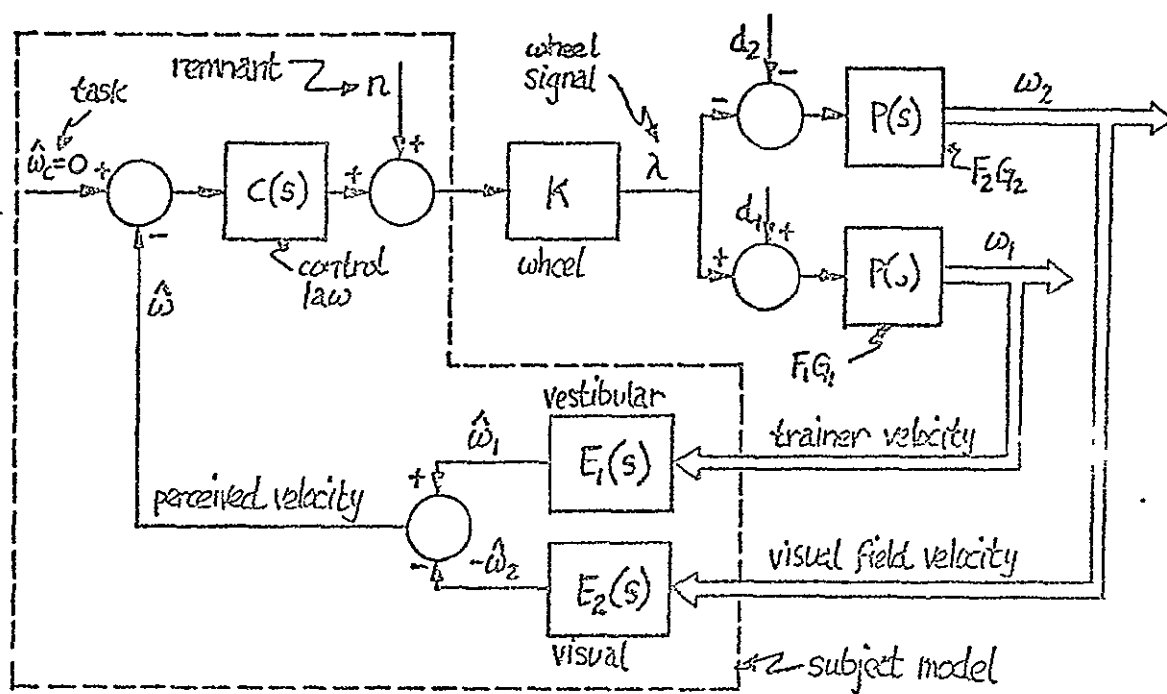
and where the transfer function dependence on the Laplace-transform variable s has been omitted for clarity. We can now make use of auto- and cross-power spectral density functions to solve for E_1 and E_2. Correlating d_1 with λ and ω_1, we have, from (1a) and (1b),

$$\Phi_{\lambda d_1} = \frac{1}{\Delta}(K\Phi_{nd_1} - KPCE_1\Phi_{d_1 d_1} - KPCE_2\Phi_{d_2 d_1}) \qquad (a)$$

$$\Phi_{\omega_1 d_1} = \frac{P}{\Delta}(K\Phi_{nd_1} + (1 + KPCE_2)\Phi_{d_1 d_1} - KPCE_2\Phi_{d_2 d_1}) \qquad (b)$$

$$(3)$$

Since the remnant is defined to be uncorrelated with the input disturbances, then

$$\Phi_{nd_1} = \Phi_{nd_2} = 0 \qquad (4)$$

Further, if the experimental design is such that d_1 and d_2 are uncorrelated, then

$$\Phi_{d_1 d_2} = \Phi_{d_2 d_2} = 0 \qquad (5)$$

Thus, dividing (3a) by (3b) and using (4) and (5) to simplify the result, we find that

$$\frac{\Phi_{\lambda d_1}}{\Phi_{\omega_1 d_1}} = -\frac{KCE_1}{1+KPCE_2} \qquad (6a)$$

In a similar fashion, it may be shown that

$$\frac{\Phi_{\lambda d_2}}{\Phi_{\omega_2 d_2}} = \frac{KCE_2}{1+KPCE_1} \qquad (6b)$$

Since the left-hand-sides of (6) are computable from the measured outputs of the experiment, we define

$$\alpha_1 \equiv \Phi_{\lambda d_1} / \Phi_{\omega_1 d_1} \qquad ; \qquad \alpha_2 \equiv \Phi_{\lambda d_2} / \Phi_{\omega_2 d_2} \qquad (7)$$

So that substituting into (6) allows for a solution for CE_1 and CE_2:

$$CE_1 = -\frac{1}{K} \frac{\alpha_1(1+P\alpha_2)}{1+P^2\alpha_1\alpha_2} \qquad (a)$$

$$(8)$$

$$CE_2 = \frac{1}{K} \frac{\alpha_2(1-P\alpha_1)}{1+P^2\alpha_1\alpha_2} \qquad (b)$$

Note that the control strategy C is embedded with the estimators E_1 and E_2 , as is to be expected, and cannot be separated from them in this type of experiment. Separation of control from estimation is the subject of section 7; the present discussion will be concerned with estimating the composite functions CE_1 and CE_2.

4.1 Disturbance Inputs

One major aspect of the experimental design concerns the choice of the two disturbance inputs d_1 and d_2. Basically, they were chosen to meet the following requirements

a. Their frequency content must span the frequency range of interest: ≈ 0.01 Hz to ≈ 1.00 Hz.

b. The high frequency power should gradually taper off, so as to avoid the "shelf" power spectrum used in earlier experiments.

c. The amplitude must be reasonably sized in terms of human operator threshold and maximum limitations on the equipment.

d. The two signals should be uncorrelated, to satisfy (5).

Chosen were   two "pseudo-random" signals, each composed of a sum of sinusoids. Each sinusoidal term is an integral prime multiple of a base frequency of 1/128 Hz (0.00781 Hz), so that the total period of each signal is 128 seconds, a period which is unrecognizable by the human operator in this task. Formally, the signals are defined by:

$$d_1 = \sum_{i=1}^{13} a_i \sin n_i \omega_0 t \qquad d_2 = \sum_{i=1}^{13} b_i \sin m_i \omega_0 t$$

where $\omega_0 = 2\pi/T$,   T = 128 seconds, and where the n_i and m_i are alternating prime numbers so as to avoid harmonic ambiguities and assure a zero correlation between the signals.

The amplitude spectra for the two signals are given in Figure 3 and are given in amplitude ratio (AR) form, referenced to a base low-frequency magnitude of $1.2^o/s$. As can be seen from the plot, the frequencies of the two signals are interleaved, and both follow the AR curve associated with a double lag-lead transfer function, given by

$$\frac{\omega_2^2 \; s^2 + 2\zeta_1 \omega_1 s + \omega_1^2}{\omega_1^2 \; s^2 + 2\zeta_2 \omega_2 s + \omega_2^2}$$

where

$$(\omega_1, \omega_2) = (0.475, 0.150) \text{ Hz}$$
$$(\zeta_1, \zeta_2) = (0.707, 0.707)$$

The lag and lead break frequencies were chosen to give a gradual transition between the large low frequency amplitudes and the small high frequency amplitudes; the 20 dB ratio between the two extremes was chosen from past experience with disturbance inputs into the trainer.

FIG 3 : Amplitude Spectra for Disturbance Inputs d_1 and d_2

$$\frac{\omega_2^2}{\omega_1^2} \frac{s^2 + 2\rho_1\omega_1 s + \omega_1^2}{s^2 + 2\rho_2\omega_2 s + \omega_2^2}$$

$$(\omega_1, \omega_2) = (0.475, 0.150) \text{ Hz}$$
$$(\rho_1, \rho_2) = (0.707, 0.707)$$

$x - d_1$ (vestibular)
$o - d_2$ (visual)

12%/s

0.12%/s

0.10   0.15   0.475   100 f (Hz)
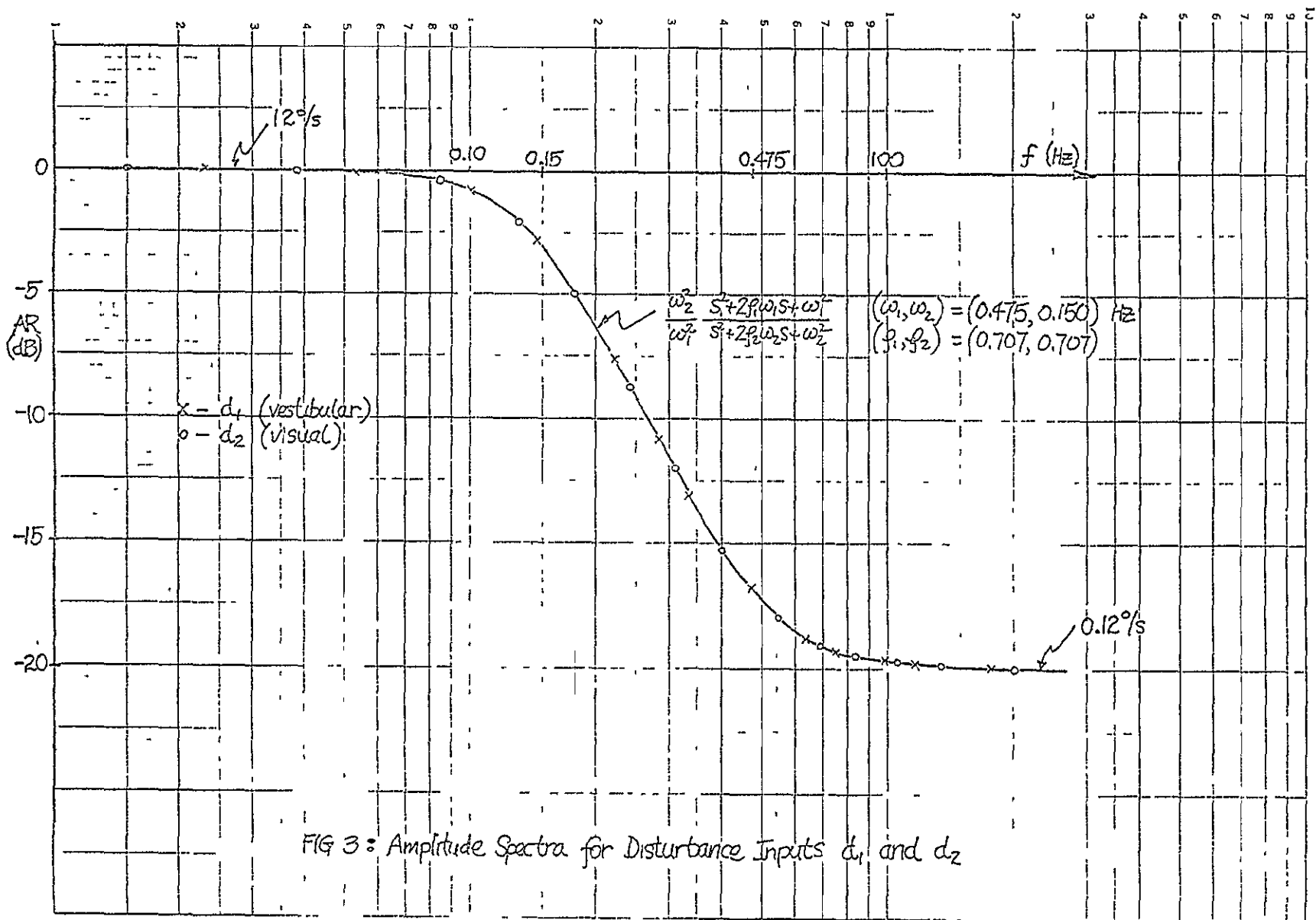
To avoid rapid start-up transients when the two disturbances begin, the signs of the amplitudes are alternated so that·

$$\text{sign}(a_{i+1}) = -\text{sign}(a_i) \quad ; \quad \text{sign}(b_{i+1}) = -\text{sign}(b_i)$$

where

$$\text{sign}(a_1) = 1 \quad ; \quad \text{sign}(b_1) = 1$$

The appearance of the resulting signals in the time domain is as shown in Figure 4 .

4.2 Plant Dynamics

The other major aspect of the experimental design concerns the choice of the plant dynamics. For computational simplicity, it would be desirable to maintain unity gain and zero phase lag for the entire range of test frequencies, but, as noted in the May progress report, the trainer transfer function, $G_1(s)$, exhibits a strong resonance at about 1.5 Hz, due to the mechanical properties of the load and drive system. To avoid this, a prefilter was added, $F_1(s)$, so as to ensure linear operation and reliable velocity feedback information over a lower frequency range. The combined plant, $F_1 G_1$, looks like a unity gain second-order system, with a break at 0.90 Hz and a damping ratio of 0.70.

It was noted earlier that this kind of response necessitates the use of a prefilter, F_2, in the projector drive circuit, to ensure that $F_1 G_1 = F_2 G_2$ ($\equiv$P). The prefilter was implemented on the analog computer and is a second-order filter with a break at 0.92 Hz and a damping ratio of 0.70.
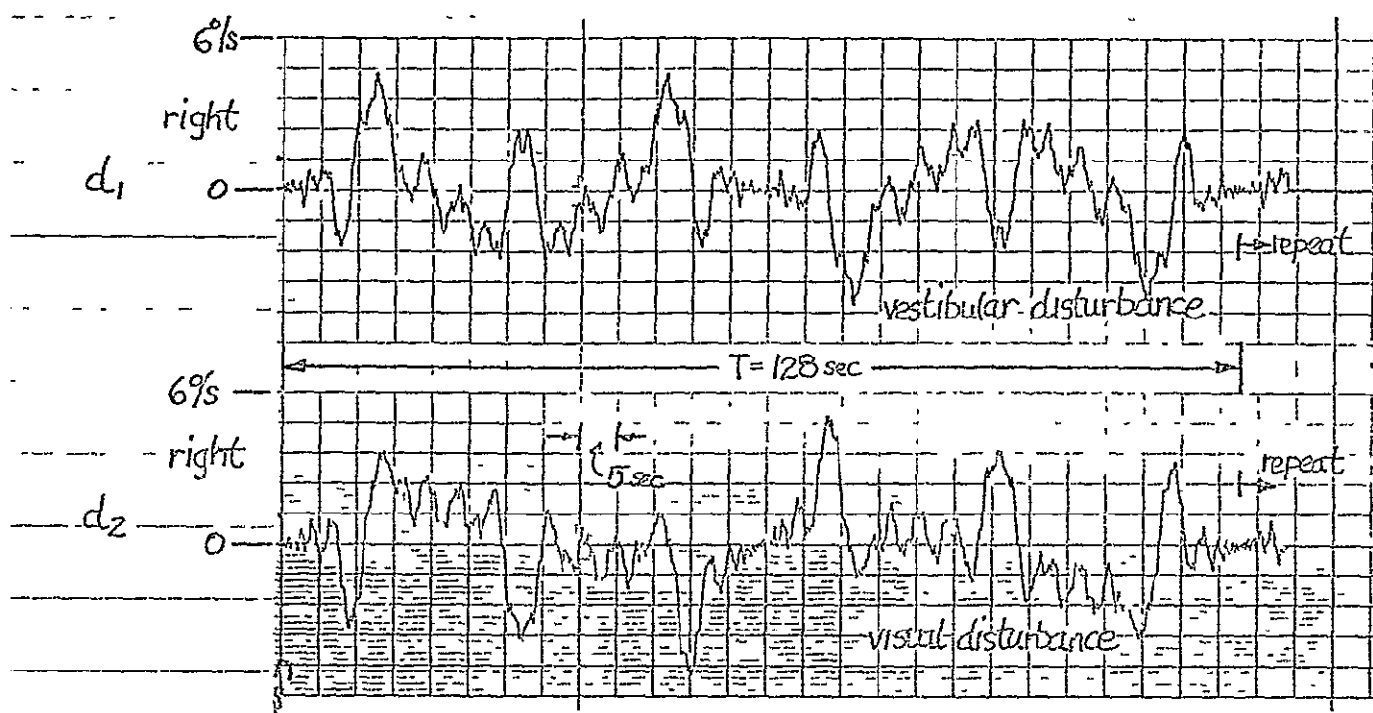
60

FIG 4 : Input Disturbances

FIGURE 5 : TRAINER/PROJECTOR I/O TEST (time histories)
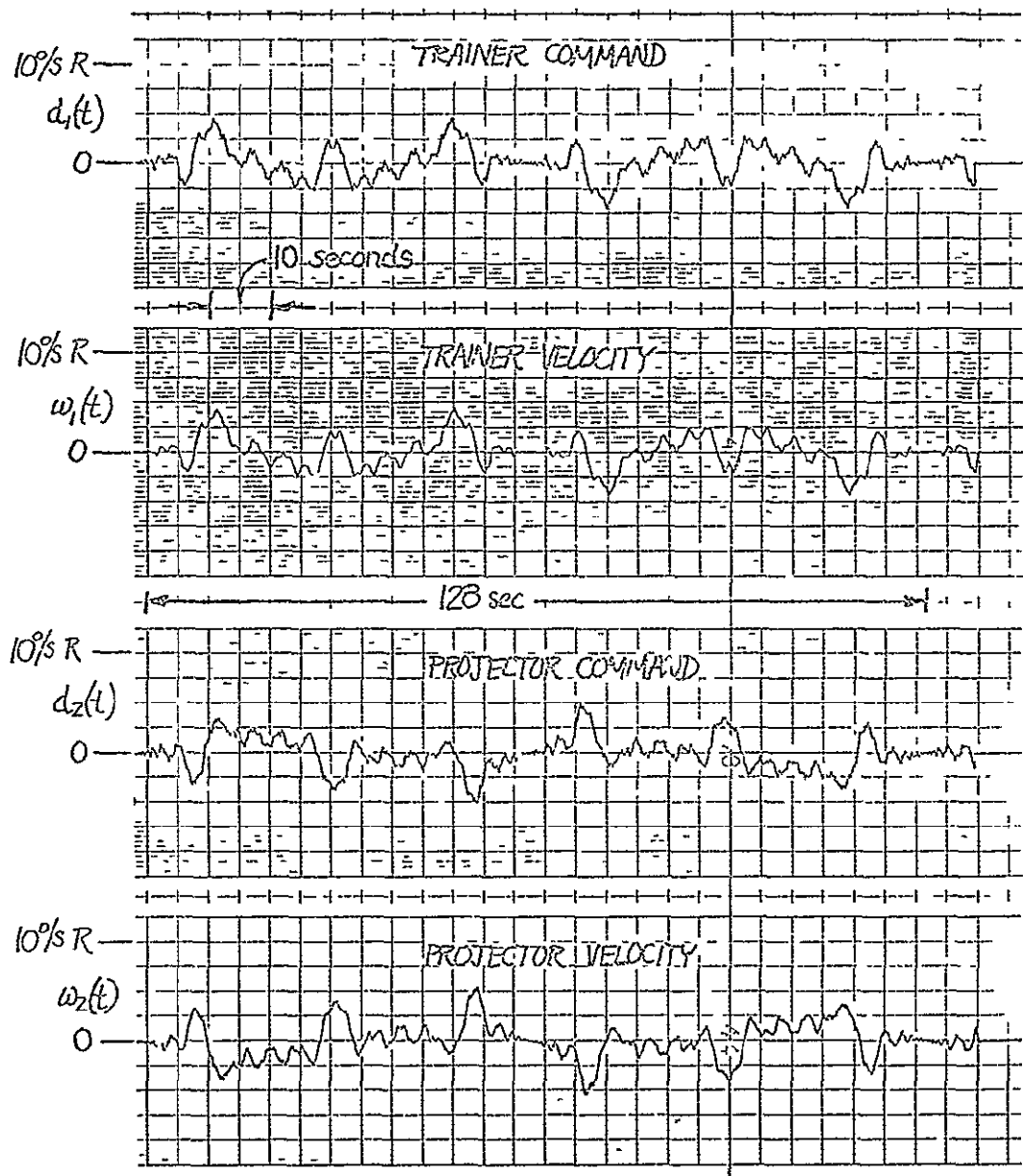
To ensure that the trainer and projector transfer functions, with their associated prefilters, were close approximations of one another, input-output testing was performed on each. The wheel signal was held at zero while the disturbance d_1 was sent into the trainer drive and the disturbance d_2 was sent into the projector drive. The time histories of the two, along with the resulting trainer and visual field motion, are shown in Figure 5 . Note the high frequency attenuation in both channels and note that the visual field velocity is the negative of the input command d_2.

By taking the Fourier transforms of these signals, the transfer functions of the trainer and projector drive can be computed. Shown in Figure 6 are the computed amplitude ratios (AR) and phase lags (ϕ) for both the trainer and projector system; superimposed on the data are the AR and ϕ curves associated with the second-order transfer function given in the figure. This data thus substantiates the experimental condition that·

$$F_1 G_1 = F_2 G_2 \equiv P = \frac{\omega_n^2}{s^2 + 2\zeta_n \omega_n s + \omega_n^2} \qquad \begin{array}{l} \omega_n = 5.65 \text{ rad/sec (0.90 Hz)} \\ \\ \zeta_n = 0.70 \end{array}$$

and thus visual field motion will mimic trainer motion, in response to both disturbance and control wheel inputs. Note that this knowledge of the plant dynamics is a prerequisite for solving for the estimator functions E_1 and E_2, as reference to (8) will show.

FIGURE. 6 :   TRAINER/PROJECTOR I/O TEST (frequency response)

Dual Input Experiment

$$P(s) \approx \frac{\omega_n^2}{s^2 + 2\zeta_n \omega_n s + \omega_n^2}$$

$\omega_n = 2\pi f_n$, $f_n = 0.90 Hz$
$\zeta_n = 0.7$

o $\left|\frac{trainer}{d_1}\right|$

+ $\left|\frac{projector}{d_2}\right|$

o $\angle \frac{trainer}{d_1}$

▫ $\angle \frac{projector}{d_2}$
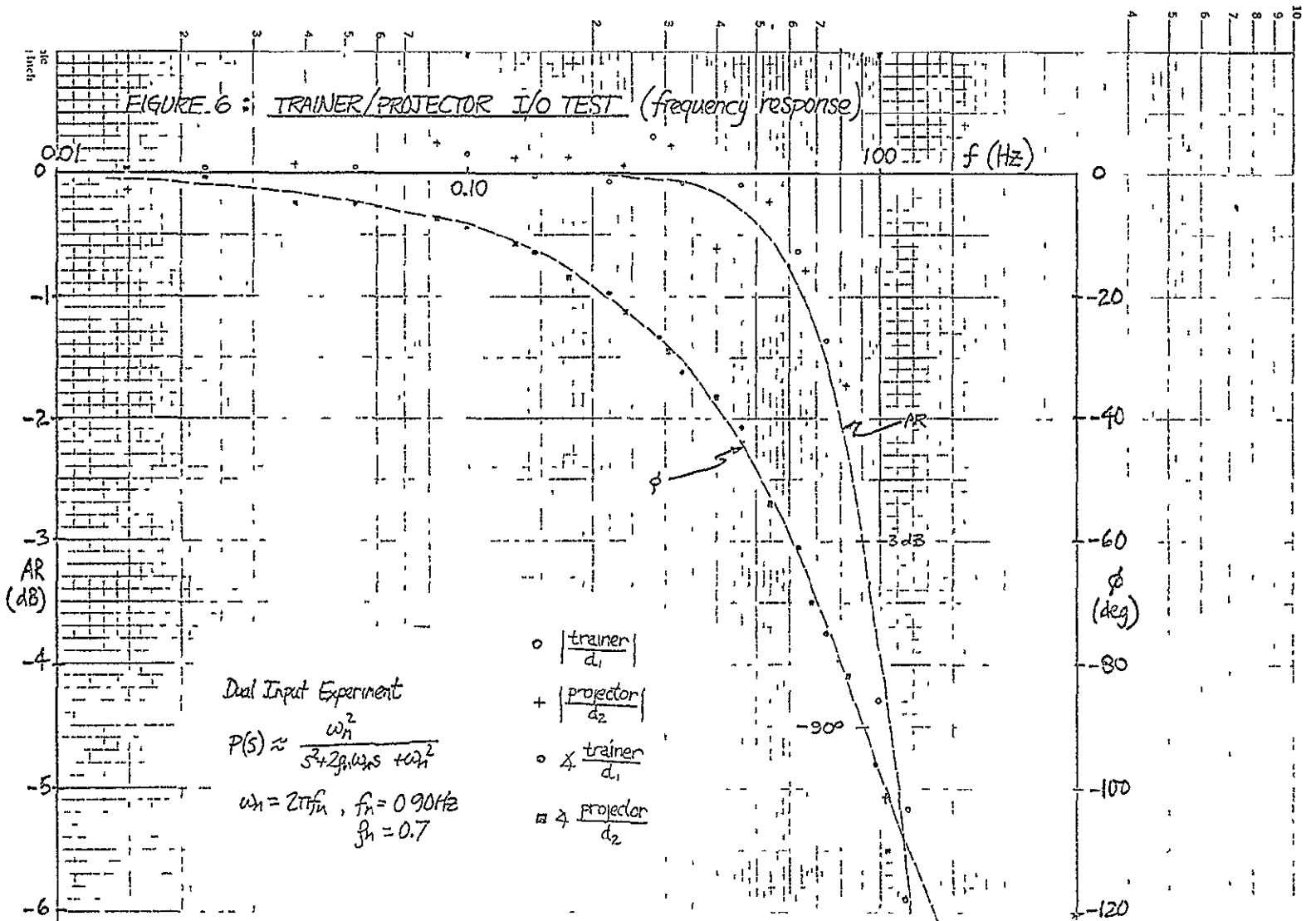
4.3 Computational Approach

At this point, it is appropriate to provide a brief description of the computational approach used in processing the experimental data to arrive at describing function estimates.

The analysis given above was based on the use of auto- and cross-power spectral density functions, but, from a practical viewpoint, it is computationally simpler to work with the Fourier transforms of the measured signals. To see how this is accomplished, it is convenient to regard the wheel response signal as being composed of three component signals, as follows.

$$\lambda(t) = \sum_{i=1}^{13} \lambda_{1i}\sin(n_i\omega_0 t + \phi_{1i}) + \sum_{i=1}^{13} \lambda_{2i}\sin(m_i\omega_0 t + \phi_{2i}) + \lambda_r(t) \tag{10}$$

By reference to (9), the first component contains those frequencies associated with d_1, the second those associated with d_2, and the third, all other frequencies which are integral multiples of the base frequency·

$$\lambda_r(t) \equiv \sum_{i=1}^{\infty} \lambda_{ri}\sin(\ell_i\omega_0 t + \theta_i) \tag{11}$$

where the set of ℓ_i is the set of all integers excluding the sets of $\{n_i\}$ and $\{m_i\}$. It should be recognized that with this definition, (10) is an approximation to the actual wheel signal, since non-integral multiples of the base frequency ω_0 have been excluded. However, such an approximation is consistent with the discrete frequency resolution which results from the digital Fourier transforms used in processing the data.

Recognizing that λ is periodic, with a period $T = 2\pi/\omega_0 = 128$ seconds, then it is a direct matter to solve for the cross-correlation function between the wheel signal and the "vestibular" disturbance:

$$\phi_{\lambda d_1}(\tau) = \overline{\lambda(t)d_1(t+\tau)} = \frac{1}{T}\int_{-T/2}^{T/2} \lambda(t)d_1(t+\tau)dt \qquad (12)$$

Substitution of (9), (10), and (11) in the above relation, followed by an application of the well-known orthogonality properties of sinusoids, results in the following expression for $\phi_{\lambda d_1}$:

$$\phi_{\lambda d_1}(\tau) = \sum_{i=1}^{13} a_i \lambda_{1i} \cos(n_i \omega_0 \tau - \phi_{1i}) \qquad (13a)$$

so that only the frequencies of d_1 appear in $\phi_{\lambda d_1}$. A similar expression may be found for $\phi_{\omega_1 d_1}$. If we follow the same procedure as with the wheel signal, and separate the trainer signal into three components, we have.

$$\omega_1(t) = \sum_{i=1}^{13} \omega_{1i} \sin(n_j \omega_0 t + \psi_{1i}) + \sum_{i=1}^{13} \omega_{2i} \sin(m_i \omega_0 t + \psi_{2i}) + \overline{\omega_{1r}(t)} \quad (14)$$

It follows that

$$\phi_{\omega_1 d_1}(\tau) = \sum_{i=1}^{13} a_i \omega_{1i} \cos(n_i \omega_0 \tau - \psi_{1i}) \qquad (13b)$$

So, again, we have only the frequencies of d_1 in $\phi_{\omega_1 d_1}$. Now, from the definition of α_j given in (7), and the sinusoidal composition of the cross-correlation functions of (13), it follows that:

66

$$|\alpha_1(n_i\omega_0)| = \frac{a_i\lambda_{1i}}{a_i\omega_{1i}} = \lambda_{1i}/\omega_{1i} = \frac{|\lambda(n_i\omega_0)|}{|\omega_1(n_i\omega_0)|} \qquad (i=1,13)$$

$$(15)$$

$$\not{\angle}\, \alpha_1(n_i\omega_0) = \phi_{1i} - \psi_{1i} = \not{\angle}\,\lambda(n_i\omega_0) - \not{\angle}\,\omega_1(n_i\omega_0) \qquad (i=1,13)$$

Or, more compactly,

$$\alpha_1(n_i\omega_0) = \lambda(n_i\omega_0)/\omega_1(n_i\omega_0) \qquad (i=1,13) \qquad (16a)$$

Naturally, the same results are applicable to the definition of α_2 given in (9):

$$\alpha_2(m_i\omega_0) = \lambda(m_i\omega_0)/\omega_2(m_i\omega_0) \qquad (i=1,13) \qquad (16b)$$

Thus instead of being involved with the computation of cross-correlation functions and their transforms to power spectral densities, the identification problem becomes one of simply input-output transfer function computation via (16), to define α_1 and α_2. That is, Fourier transforms may be made directly on the measured signals λ, ω_1, and ω_2, and the complex algebra of (16) can then be used to specify α_1 and α_2 at the discrete input frequencies of d_1 and d_2.

It should be noted from (16) that since α_1 and α_2 are not defined at the same frequencies, then the computations for CE_1 and CE_2 indicated by (8) cannot be made. What is required is an assumption of continuity, in the frequency domain, of the transfer functions introduced by the linear model. This then allows for one to interpolate across frequency to obtain the needed α_1 and α_2 values. That is, one can interpolate between the α_1 values

defined at the $n_i \omega_0$ frequencies to obtain values for α_1 at the $m_i \omega_0$ frequencies, and conversely for α_2. With α_1 and α_2 both defined in this manner at all 26 input frequencies introduced by both d_1 and d_2, (8) may then be used to define the describing functions CE_1 and CE_2, for all 26 frequencies. This was the approach used in the data processing which followed FFT processing of the recorded signals.

This then completes the discussion of the parallel channel visual-vestibular model and the dual-input experimental and computational approach for estimating the model's separate visual and vestibular transfer functions.

68

5.0 DUAL-INPUT EXPERIMENTAL RESULTS

As in the previous velocity-nulling experiments, the subject's task in this series was to maintain his sensation of self-velocity as close to zero as possible, by appropriate motions of the control wheel, and by inferring self-motion from the continued application of visual and vestibular cues. After a familiarization period with the procedure and equipment, the subject performed one continuous run of velocity nulling which lasted for approximately eight minutes. During this run, the vestibular disturbance (d_1 referred to in the last section) was continuously inputted to the trainer drive. The visual environment, however, alternated between two modes: a counter-rotating field (CON mode) which provided accurate confirmation of vestibular cues, as in the previous series, and an independently moving field (DI mode), which was the result of a visual field velocity disturbance (d_2 referred to in the last section) inputted to the projector drive. Each presentation mode lasted for 128 seconds, and alternated with the other, so that there were two presentations of each visual field condition to a subject

Series A   CON, DI, CON, DI

Series B.   DI, CON, DI, CON

Half the test population of 6 subjects received series A, while the other half received series B, so as to provide a balance for fatigue and learning effects when averages are taken across the population.

69

Shown in figure 1 are time histories of a portion of a subject's run, showing the vestibular disturbance d_1, the trainer and visual field velocities ω_1 and ω_2 and the subject's compensatory response λ. The first portion (CON mode) illustrates good velocity-nulling performance when the subject is presented with a counterrotating visual field, and specifically shows his ability to null out low frequency disturbances, presumably because of the corroborating visual motion cue provided The second portion (DI mode) illustrates poorer performance, especially with regard to nulling out low-frequency drift in the trainer velocity. Presumably, his low frequency stick response is primarily dedicated to nulling out the visual field velocity disturbance as evidenced by the contrasting lack of drift seen in the field velocity history.

5.1 Frequency Domain Results

More definitive observations on subject response during DI presentation can be made in the frequency domain. Shown in figure 2 are two wheel deflection amplitude spectra plots, superimposed on one another, obtained from one individual by transforming the recorded wheel history via an FFT program. The sample rate used was 8 Hz, and the sample length was 128 seconds, so that each FFT performed covered one entire DI presenta- tion , resulting in the two spectral sets shown

The circles identify subject response at the frequencies contained in the "vestibular" disturbance signal d_1, the squares identify response at the frequencies contained in the "visual" signal d_2, and the dots identify the remnant; i.e. response at frequencies contained in neither disturbance input. At the "vestibular" frequencies (circles), the

70

FIGURE 1 : DUAL INPUT PERFORMANCE

- Visual field velocity disturbance independent of vestibular disturbance
- High-frequency vestibular cues picked up
- Low-frequency vestibular cues corrupted by visual input

FIGURE 2 : _WHEEL AMPLITUDE SPECTRA_

DUAL-INPUT EXPERIMENT
TWO INDIVIDUAL RUNS

(DTS003 , DTS004)

wheel deflection
amplitude

(100 units ≈ 8.6°)

o   "vestibular" frequencies — d_1
□   "visual" frequencies — d_2
·   remnant response

remnant curve:
— (K=15,000; μ=0.4; σ_L=2; σ_R=0.15; α=2000)

f (Hz)

200

150

100

50

0

0.01   0.10   1.00
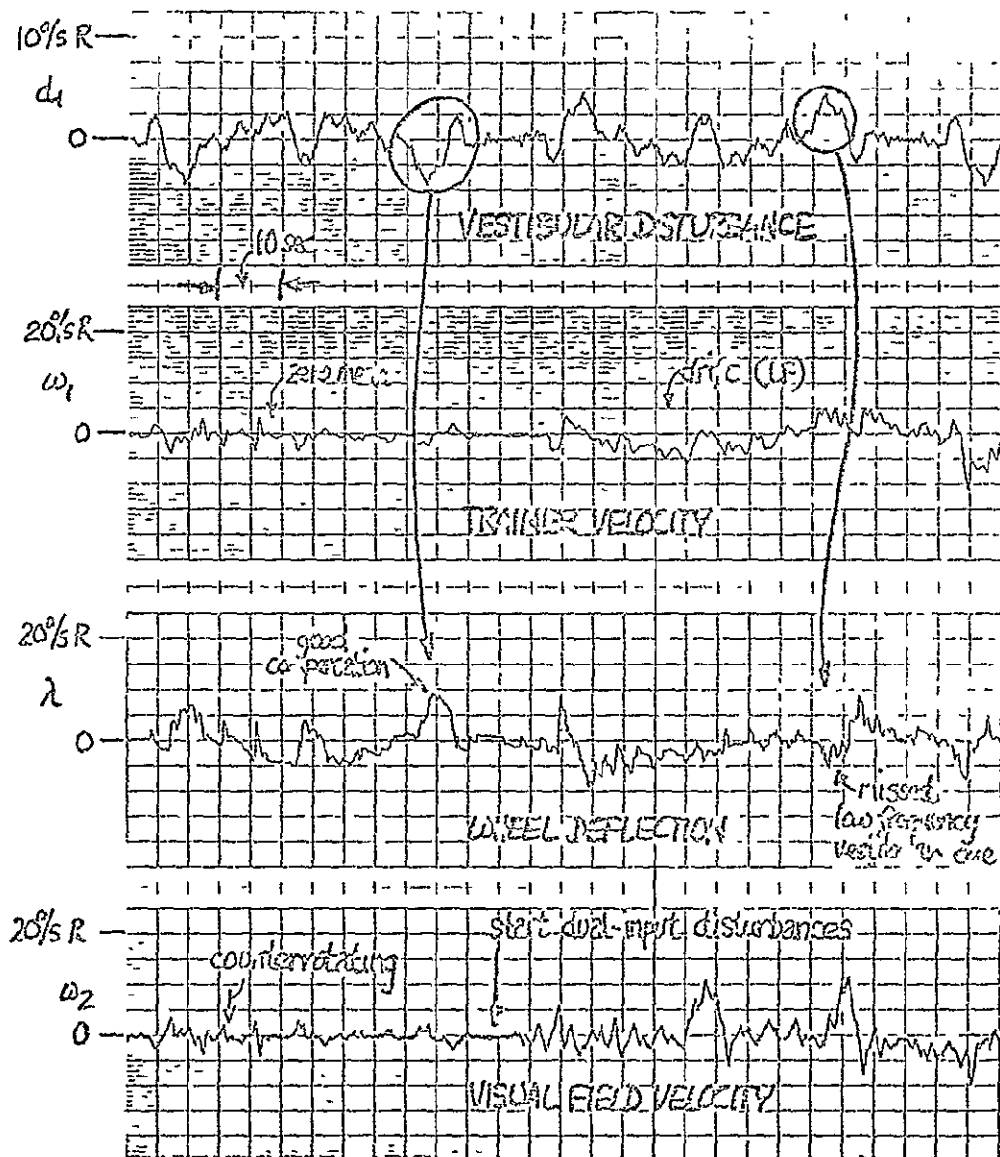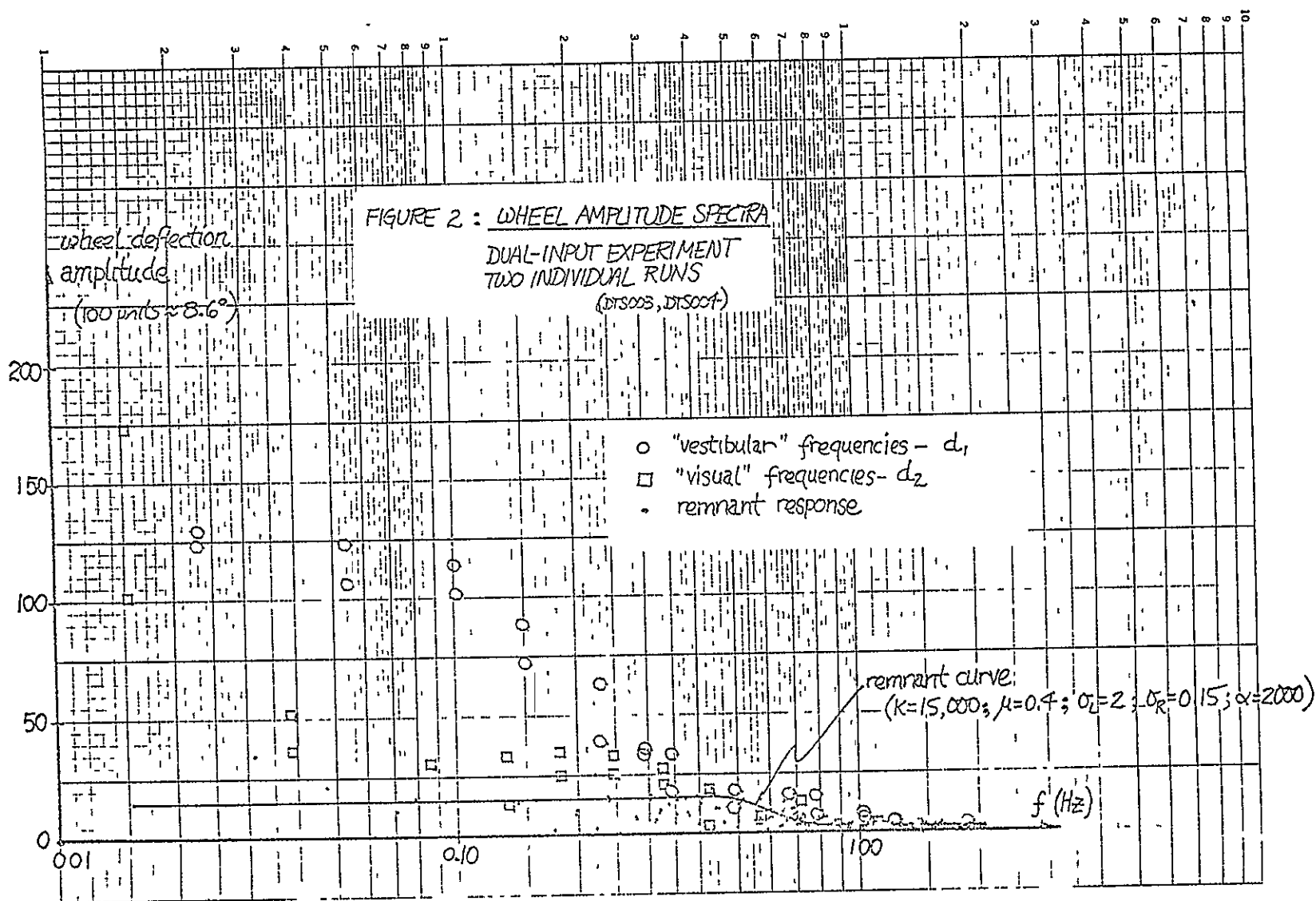
response can be seen to follow the shape of the disturbance spectrum
presented in the last section (figure 3), indicating an appropriate
compensatory response to trainer velocity. This, of course, assumes that
the phase is appropriate, a subject to be discussed later. In contrast,
response at the "visual" frequencies (squares) shows a sharp drop off at
low frequency, indicative of little attention being paid to the high
frequency visual inputs in the task of nulling perceived self-velocity.

A smooth curve has been drawn through the remnant response (dots) so as
to provide a simple approximation to the remnant power, and will serve
as the basis, in section 8, for a discussion of remnant power correction
to derived operator transfer functions. For now, however, it suffices to
note the general trend of remnant dominance of subject response as frequency
increases, especially at frequencies greater than approximately 0.5 Hz. It
is also appropriate to note the difference in signal-to-noise power (S/N)
ratios between response at "vestibular" frequencies and at "visual" fre-
quencies. To calculate the S/N ratios, we square the amplitudes of figure
2 to obtain the power spectra. Then, by linearly interpolating between
responses at the "vestibular" frequencies (circles), and integration over
the frequency range shown, the total "vestibular" power in the wheel
response can be calculated. A similar calculation yields the total "visual"
power, while integration under the smooth remnant curve yields a figure for
remnant or noise power. Ratios of these figures then result in S/N ratios
for both sensory channels. Since figure 2 illustrates response for two
DI presentations, we obtain the following two sets of S/N ratios:

DI Channel presentation	Vestibular	Visual
first	24.2	14.4
second	24.9	11.8

(S/N ratios in dB)

Obviously the major difference is the 10 to 12 dB difference between response at the two sets of frequencies, indicative of the greater importance of vestibular cues in this nulling task, especially at the higher frequencies. This aspect of the response will be discussed in greater detail when remnant corrections to the response are considered.

It should be clear that subject response during the CON visual field presentations of this DI experiment can be similarly analyzed in the frequency domain. Since many of the results are similar to those already presented in the May progress report (for earlier experimental series), a discussion of the CON results will be deferred to a later section. For now, we will continue to describe the results obtained from DI presentations.

5.2 Population Averages for CE_1 and CE_2

Plots similar to that of figure 2 could also be drawn to illustrate the amplitude spectra of trainer motion ω_1 and visual field motion ω_2, and qualitative conclusions could be drawn regarding the appropriatness of the subject's compensation. It is more direct, however, to simply apply the computational techniques of the last section to this frequency

74

data, and arrive at estimates of the two describing functions, CE_1

and CE_2. This has been done for both DI presentations to each subject,

for all six subjects, and the resulting population average Bode plots
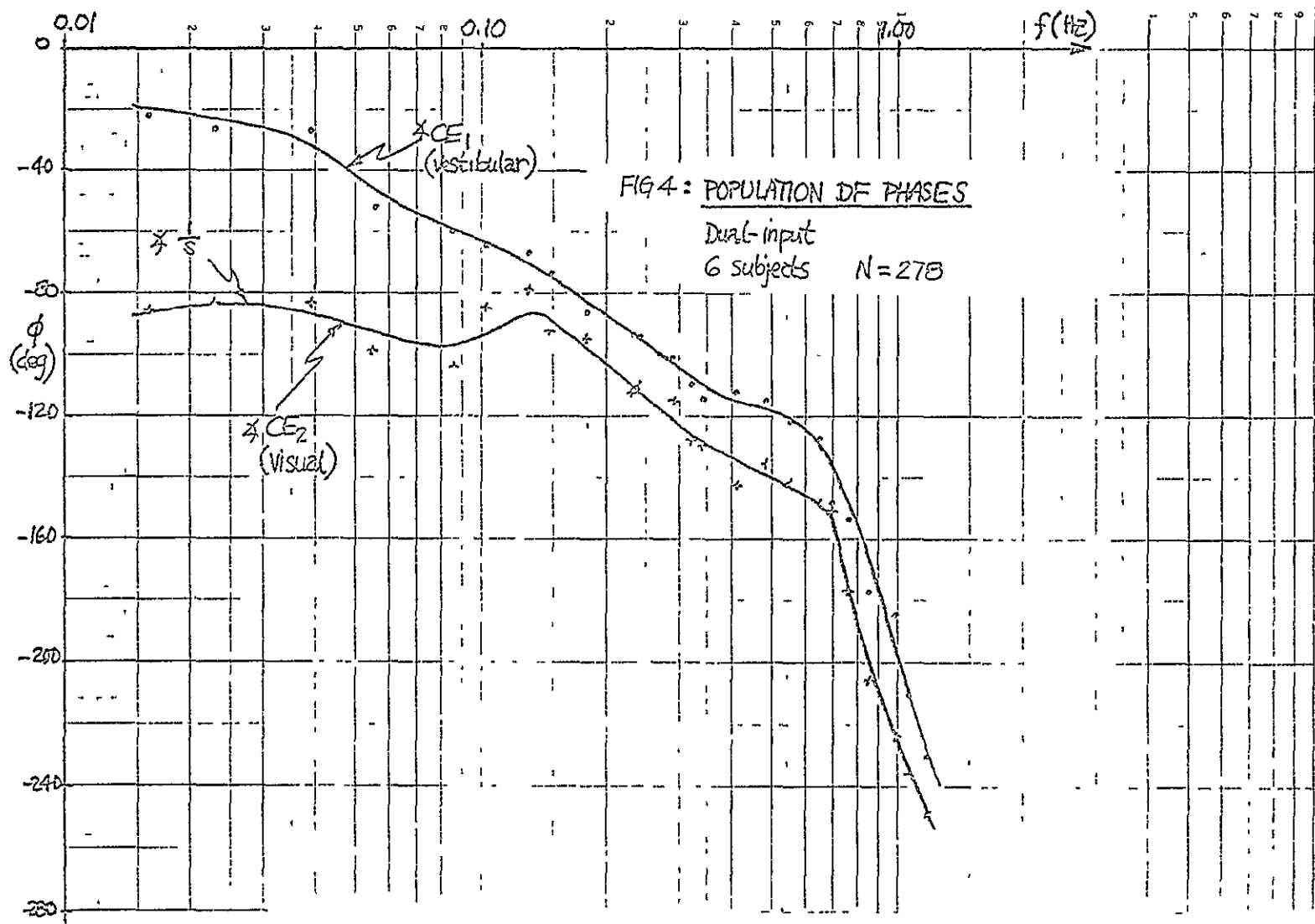
are given in figures 3 and 4.

The data points in the figures identify averages for the six subjects,

while the smooth lines drawn through them simply indicate trends as

the frequency changes. Several points are worth noting First, the

gain for the "vestibular" describing function, CE_1, follows, in the mid-

range frequencies, what would be expected from a lag-lead function. It

may be recalled from the May progress report that a lag-lead function

formed the basis for the adjustable parameter vestibular model, and the

results shown here support that approach. The earlier results also show

a lead at high frequencies, again evident in figure 3. The major dif-

ference, however, is in low frequency behavior· the earlier single channel

model indicated a levelling off to some fixed DC gain, whereas the gain for

CE_1, is seen to be dropping off as the frequency approaches zero. The

"washout" characteristic is entirely consistent with our notion of neg-

ligible canal response at very low frequencies, because of the canal's

AC physical properties. The Bode plots defining the "visual" transfer

function, CE_2, show quite contrasting behavior. At low frequencies, the

gain is higher than in the vestibular channel, supporting the previous

statements concerning the importance of low-frequency visual cues in

determining motion sensation. Up to approximately 0.1 Hz, CE_2 looks like

a simple integrator (in gain and phase), which, as will be seen in the

next section, is simply a reflection of of the control strategy used by the

subjects. Above that frequency, the CE_2 gain levels out, followed by a slight

FIG 3: POPULATION DF AR's

Dual-input
6 subjects   N = 278

FIG 4 : POPULATION OF PHASES

Dual-input
6 subjects   N = 278
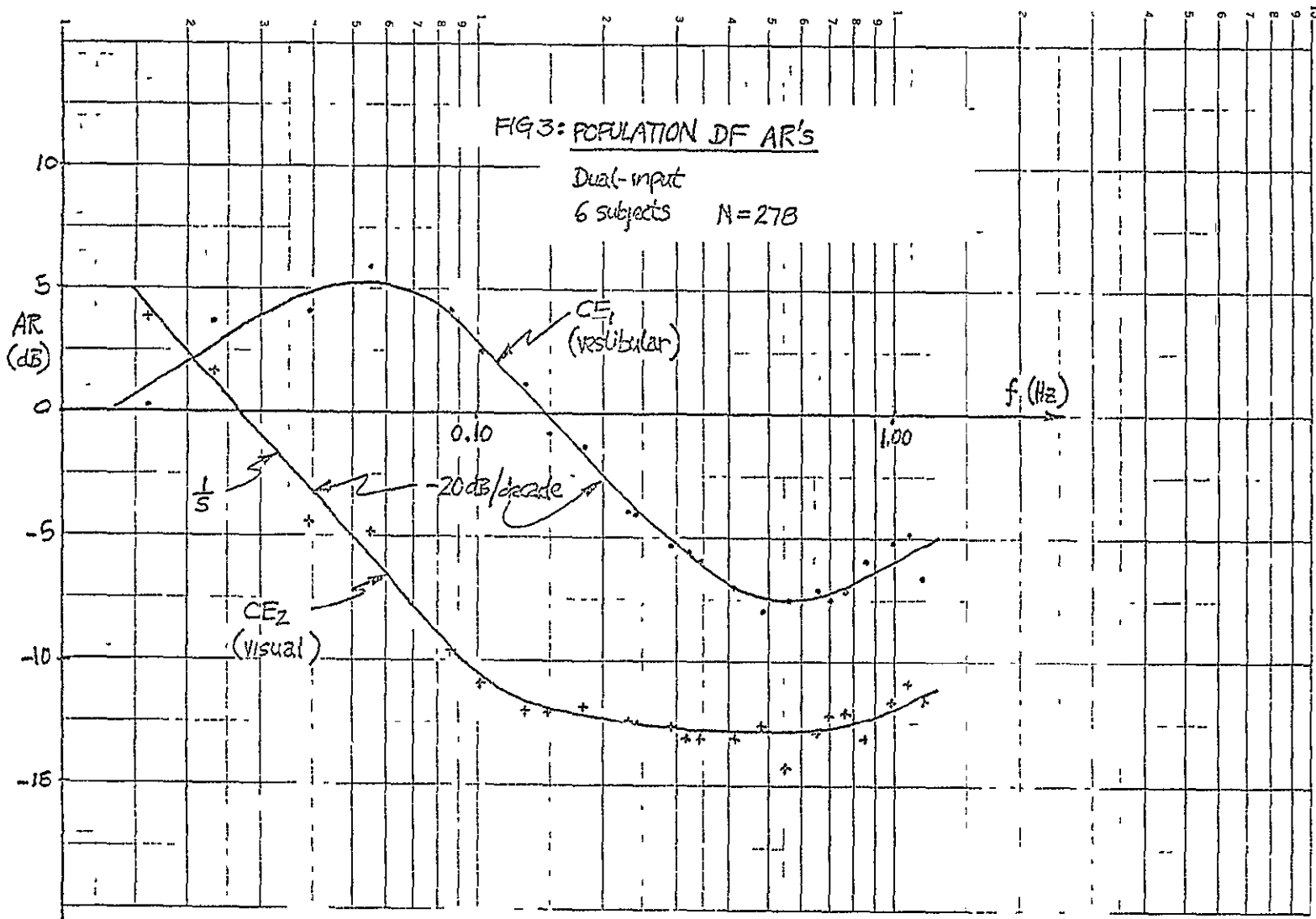
lead at the highest frequencies; these latter two features are not
particularly easy to interpret at this point, but will be discussed
in the section concerning remnant corrections. What should be obvious,
however, is that the visual gain is considerably smaller (~10 dB)
than the vestibular gain, over most of the frequency range, excluding
the very low-frequency crossover region.

5.3 Non-linear Least-squares Curve Fit Results

A non-linear curve-fitting program was used to fit the above data
with different types of specified transfer functions. Shown in figure
5 is the gain data for CE_1, with both the mean and standard deviation
bar-plotted at each frequency. Superimposed on this data are three
curves resulting from the fitting program and the choice of three
transfer functions:

$$\text{Lag-lead} \quad K\left(\frac{\tau_1 S+1}{\tau_2 S+1}\right) \tag{1a}$$

$$\begin{array}{l}\text{Lag-lead} \\ \text{plus washout}\end{array} \quad K\left(\frac{S}{\tau_3 S+1}\right)\left(\frac{\tau_1 S+1}{\tau_2 S+2}\right) = K\omega_1^2 \frac{S(\tau_1 S+1)}{S^2 + 2\zeta_1\omega_1 S + \omega_1^2} \tag{1b}$$

$$\begin{array}{l}\text{Lag-lead} \\ \text{plus washout} \\ \text{plus lead}\end{array} \quad K(\tau_4 S+1)\left(\frac{S}{\tau_3 S+1}\right)\left(\frac{\tau_1 S+1}{\tau_2 S+1}\right) = KS\frac{\omega_1^2}{\omega_2^2} \frac{S^2 + 2\zeta_2\omega_2 S + \omega_2^2}{S^2 + 2\zeta_1\omega_1 S + \omega_1^2} \tag{1c}$$

The complex pole format indicated above was chosen so as to allow the
fitting program the greatest flexibility in minimizing the fit error.
As can be seen from the figure, the lag-lead function approximates very
roughly the gerneral trend of the means, while the addition of the wash-
out allows for a very good fit at both the low- and mid-frequencies.

$|CE_1|$

FIG 5 : "VESTIBULAR" DF AR'S (CE₁)

6 SUBJECT POPULATION
UNCORRECTED FOR REMNANT
EMBEDDED CONTROL STRATEGY

AR (dB)

f (Hz)

lag-lead

{lag-lead plus washout;
{lag-lead plus washout plus lead

lag-lead plus washout
plus lead

{lag-lead;
{lag-lead plus washout

lag-lead : $K\left(\dfrac{\tau_1 s + 1}{\tau_2 s + 1}\right)$

lag-lead
plus washout : $K s \dfrac{(\tau_1 s + 1)\,\omega_1^2}{s^2 + 2f_1\omega_1 s + \omega_1^2}$

lag-lead
plus washout : $K \dfrac{\omega_1^2}{\omega_2^2} s \dfrac{s^2 + 2f_2\omega_2 s + \omega_2^2}{s^2 + 2f_1\omega_1 s + \omega_1^2}$
plus lead

$\begin{cases} K = 10\,8 \\ (\omega_1, \omega_2) = (0.29, 3.66) \\ (f_1, f_2) = (0.83, 0.85) \end{cases}$

79

Finally, addition of the lead provides for a good fit at the high end of the spectrum. Because of the spread in the data (indicated by the standard deviation bars), the fit improvement, as one progresses from one transfer function to another, is not especially dramatic when measured in terms of residual error: the residual is only reduced by approximately 10% when the lag-lead is augmented by the washout and additional lead. A more dramatic improvement would be evident if only the means were used as the data to be fitted, as should be clear by an inspection of the figure

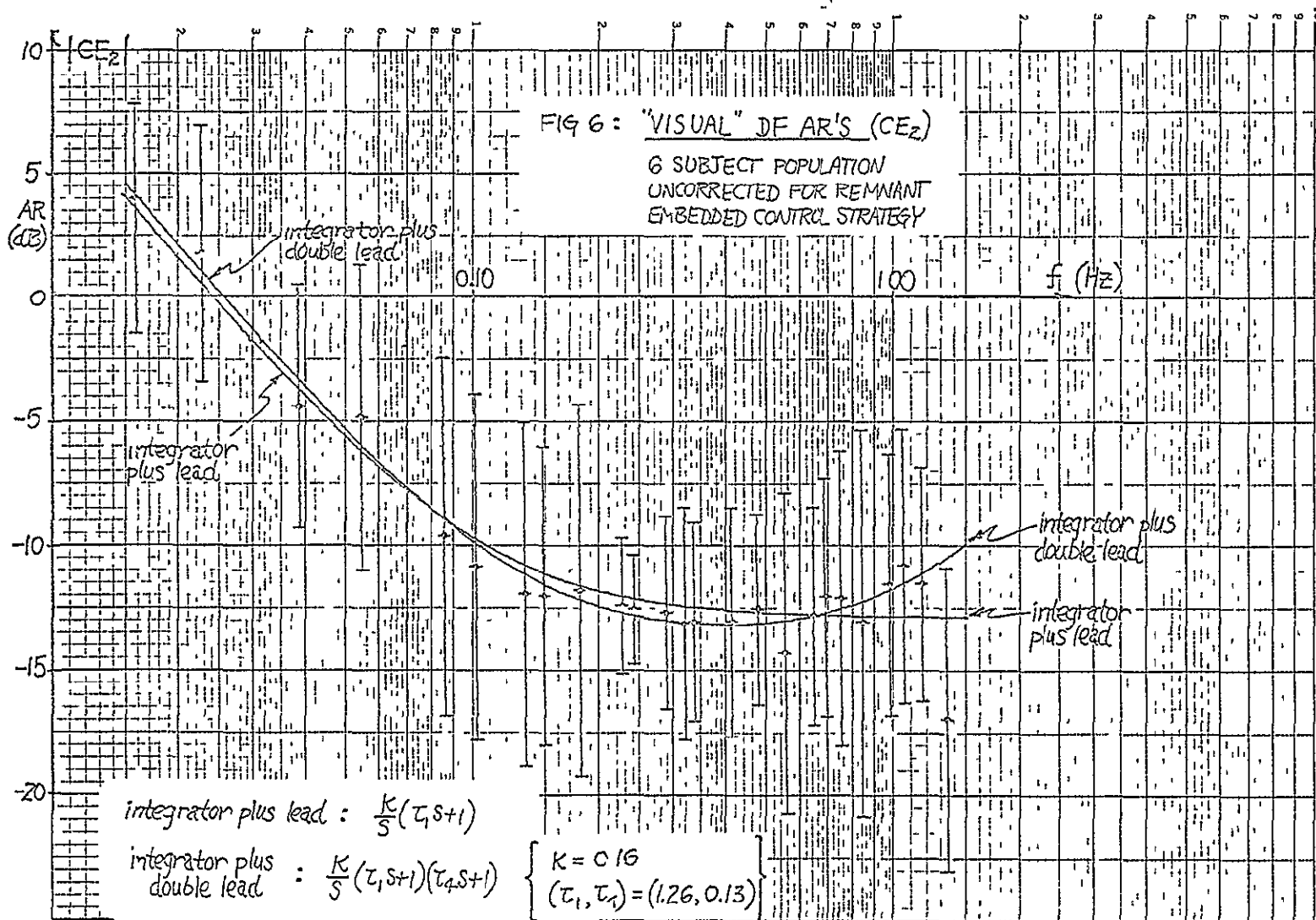The parameter values obtained from fitting the double second-order function of (1c) are given below:

Table 1: Parameter Values for CE_1 Amplitude Fit

Parameter	K	ω_1	ζ_1	ω_2	ζ_2	
Parameter Value θ	10.8	0.29	0.83	3.66	0.85	
Parameter S.D. σ_θ	1.70	0.02	0.14	0.25	0.14	

Note that both the poles and zeroes are complex, so that the fit procedure does not allow for a simple justification of the functional form by appealing to the idea of cascading simpler first-order transfer functions This aspect of the problem will be discussed later.

Similar transfer function fits may be made to the "visual" channel transfer function data specifying CE_2; these are shown in figure 6. The functions used were:

80

FIG 6: "VISUAL" DF AR'S (CE$_z$)

6 SUBJECT POPULATION
UNCORRECTED FOR REMNANT
EMBEDDED CONTROL STRATEGY

integrator plus lead : $\frac{K}{S}(\tau_1 S+1)$

integrator plus double lead : $\frac{K}{S}(\tau_1 S+1)(\tau_4 S+1)$ $\left\{ \begin{array}{l} K = 0.16 \\ (\tau_1, \tau_4) = (1.26, 0.13) \end{array} \right\}$

Integrator plus lead : $\frac{K}{S}(\tau_1 S + 1)$ (1d)

Integrator plus : $\frac{K}{S}(\tau_1' S + 1)(\tau_4 S + 1) = \frac{K}{S}\frac{1}{\omega_2^2}(S^2 + 2\zeta_2\omega_2 S + \omega_2^2)$ (1e)
double lead

where the parameter choice was made for consistency with the parameters

used in the fits on CE_1. As can be seen from the figure, both functions

fit the data means quite well, with the additional high-frequency lead

allowing for a better fit at the high end of the spectrum. Again,

because of the data spread indicated by the standard deviation bars,

the reduction in residual fit error is quite small with the additional

lead term, but it is clear that the mean trends are better fit with

the additional lead.

The parameter values obtained from fitting the integrator plus

double lead function of (1e) are given below:

Table 2. Parameter Values for CE_2 Amplitude Fit

Parameter	K	τ_1	τ_4	ω_2	ζ_2	
Parameter Value θ	0.16	1.26	0.13	2.45	1.71	
Parameter S.D. σ_θ	0.02	0.04	0.01	0 30	0.30	

Because of the large frequency difference seen in the break frequencies

of the data of figure 6, the double zero consists of two real zeroes.

The complex parameter values (ω_2, ζ_2) are included here for convenient
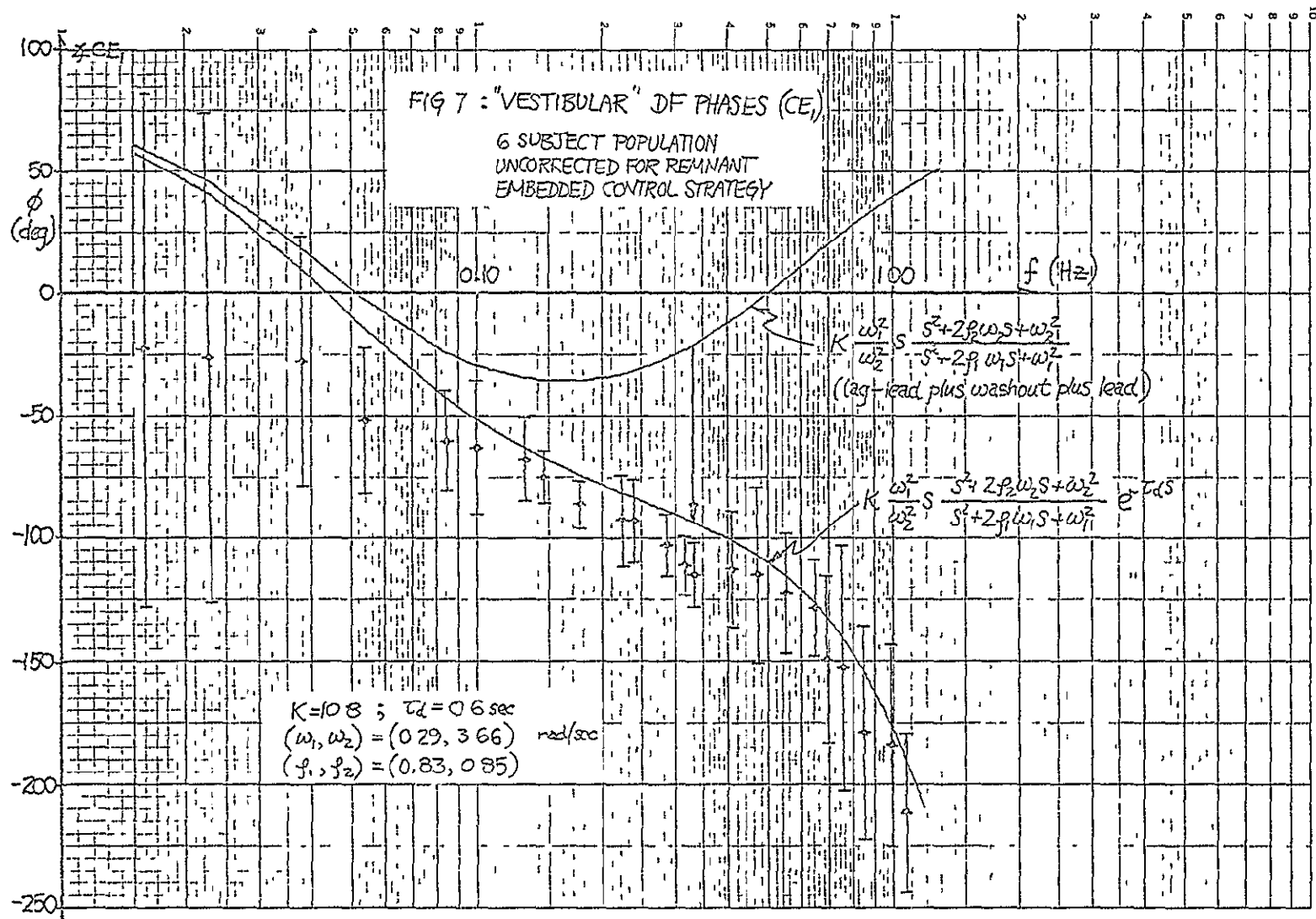
reference later.

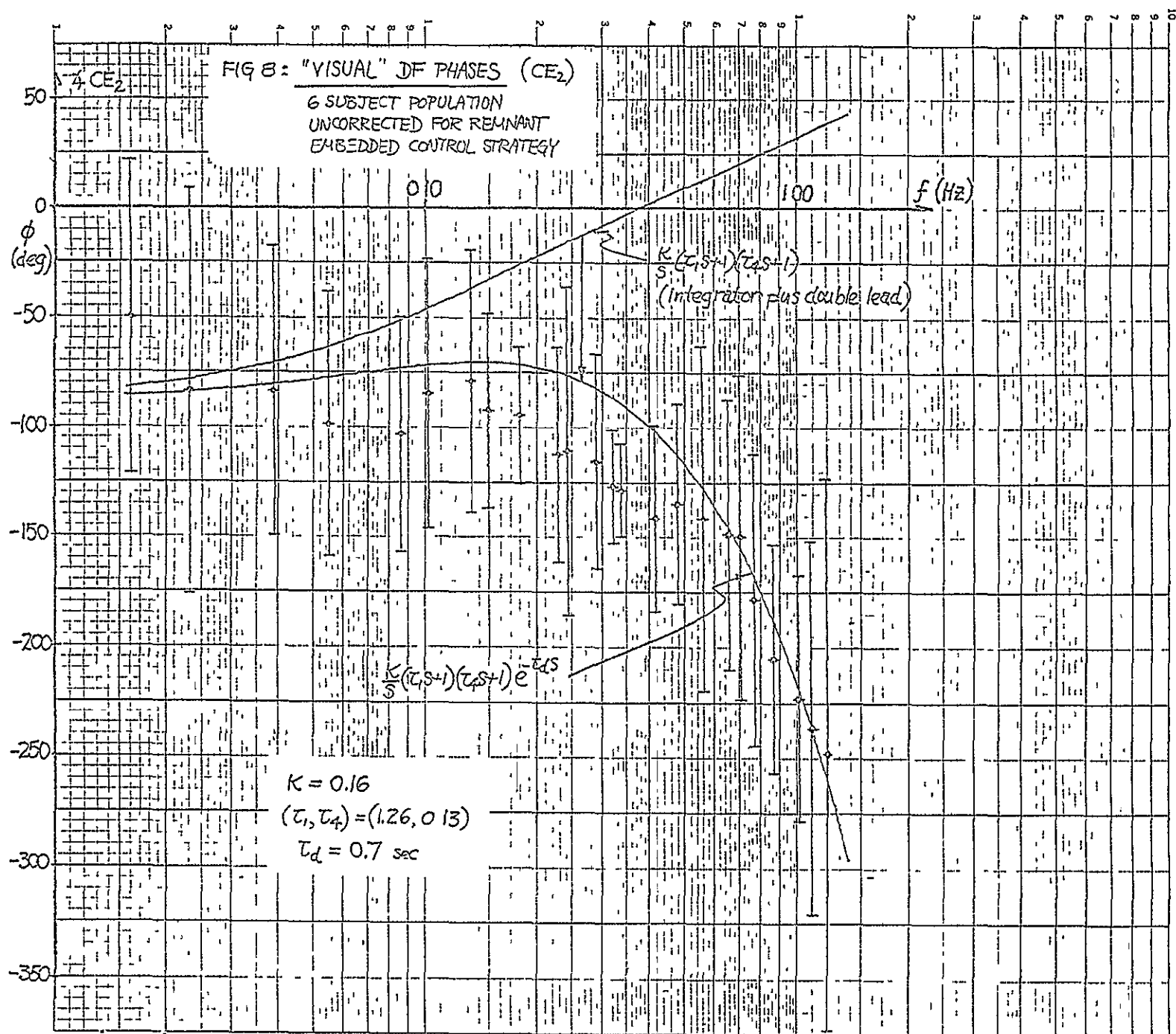What sould be clear at this point is that, if the "vestibular" transfer

function CE_1 is given by (1c) and the "visual" transfer function CE_2 by (1e), and the parameter values are as specified in tables 1 and 2, then a problem arises because of the non-congruence of any poles or zeroes. That is, if the control strategy C is anything but a DC gain, then we should expect to see its poles and zeroes common to both CE_1 and CE_2. But this is not the case, which suggests that either C is a pure gain so that we actually have measures of E_1 and E_2, or that the curve fitting just described is a premature exercise, which should await further processing of the data to account for control strategy dynamics. This question will be answered in the next section; for now however, some additional observations concerning the phase characteristics are appropriate.

Shown in figure 7 and 8 are the calculated phase angles associated with CE_1 and CE_2, respectively. As before, the data is summarized by bar-plots of the population mean and standard deviation at each frequency. The dashed curve in each figure is the phase predicted by the transfer functions just described used to fit the amplitude data. The large discrepancy between this predicted phase and the actual trends of the data is presumably due, in part, to operator latency, as we have seen in earler phase data fitting exercises. Addition of a dead-time factor to the transfer functions results in the solid curve shown in each figure. The two delay times were chosen by visual inspection, and provide an approximate fit to the phase data means.

Two brief comments are appropriate here. First, from figure 7,
it should be clear that the curve fit to the phase data at low
frequencies is inadequate in the case of the "vestibular" channel.
The model predicts a lead where we actually observe a lag, and
would suggest the incorporation of a low-frequency lag term in
the model. How to accomplish this without affecting the AR
curve fit is at present unclear. The second point concerns the
relatively large delay times necessary to account for the observed
high frequency lags, approximately 0 6 to 0.7 seconds. Presumably
this delay time can be apportioned between the operator's estimation
and control functions; the balance between the two necessitates
a closer look at the operator's control strategy, and is the
subject of the next section.

FIG 7 : "VESTIBULAR" DF PHASES (CE)

6 SUBJECT POPULATION
UNCORRECTED FOR REMNANT
EMBEDDED CONTROL STRATEGY

$$K \frac{\omega_1^2}{\omega_2^2} S \frac{S^2 + 2\beta_2 \omega_2 S + \omega_{2i}^2}{S^2 - 2\beta_1 \omega_1 S + \omega_1^2}$$

(lag-lead plus washout plus lead)

$$K \frac{\omega_1^2}{\omega_2^2} S \frac{S^2 + 2\beta_2 \omega_2 S + \omega_2^2}{S^2 + 2\beta_1 \omega_1 S + \omega_{1i}^2} e^{-\tau_d S}$$

$K = 10.8$; $\tau_d = 0.6 \, sec$
$(\omega_1, \omega_2) = (0.29, 3.66)$ rad/sec
$(\beta_1, \beta_2) = (0.83, 0.85)$

FIG 8: "VISUAL" DF PHASES (CE₂)

6 SUBJECT POPULATION
UNCORRECTED FOR REMNANT
EMBEDDED CONTROL STRATEGY

$\frac{K}{s}(\tau_1 s+1)(\tau_4 s+1)$
(integrator plus double lead)

$\frac{K}{s}(\tau_1 s+1)(\tau_4 s+1)e^{-\tau_d s}$

$K = 0.16$
$(\tau_1, \tau_4) = (1.26, 0.13)$
$\tau_d = 0.7$ sec

6.0 VISUAL FIELD VELOCITY NULLING EXPERIMENT

As noted in the previous section, the subject's control strategy C(s) is embedded in the describing functions obtained from both the dual-input experiment (series IV) and the earlier velocity-nulling experiments (series I, II, III). Thus, the objective of determining the linear estimator functions E_1 and E_2 has yet to be met.

This motivated the design of another experimental series (VI) aimed at determining the control strategy, so that its effect could be divided out of the results already obtained. The experiment was designed so as to minimize the estimation task of the subject, but maintain the same controller structure used earlier. Specifically, the task chosen was a standard human operator visual compensatory tracking task in which the subject was instructed to null visual field velocity via appropriate motions of the control wheel. The disturbance noise injected into the projector drive loop was identical to that used in the dual-input experiment (i.e., the signal d_2) and the control wheel polarity was changed to be consistent with the field nulling task, i.e., a right wheel deflection resulted in right field motion. The same plant dynamics as before (P(s)) were inserted between wheel deflection and projector motion

The trainer remained stationary throughout the task, and the subject was informed of this prior to the experiment. In addition, to avoid any possibility of circularvection induced by the visual field motion, the side windows of the trainer were made opaque and the moving stripe pattern used earlier was projected on the trainer's front window. No sensations of self-motion were induced by this arrangement, as indicated by post-test questioning of the subjects.

87

This experimental series can be directly compared to the earlier velocity nulling tasks in which the visual field remained fixed. Both are single input experiments (visual field velocity in the present series, trainer velocity in the earlier ones) both requiring a single estimator cascaded with a control logic. Here, however, because of the known high-pass characteristics of the visual system it is reasonable to assume that the visual field velocity estimator necessary for this task has essentially unity gain over the frequency range of interest (nonlinear gain characteristics are another matter, however, and will be the subject of another study). Thus, what is measured in this experiment is the subject's control logic $C(s)$.

Of course, it can be argued that the subject's control strategy in this experiment will differ from that used in the motion nulling experiments, simply on the basis that the tasks are different. However, this can be countered by noting that the same control wheel, plant dynamics, and input disturbance (in the visual channel) are used in both experimental series. In addition, the tasks are similar in that a nulling of perceived velocity is being asked of the subject, in one case self-velocity and the other, visual field velocity. Since there is obviously no conclusive way to disect the control strategy from the estimators proposed in the parallel channel model, it seems reasonable to assume an identity between the control logics of the two tasks, especially in view of task similarities.

Shown in figure 1 is a block diagram of the nulling task, summarizing the basic features of the experiment and the conjectured functional structure of the human operator. From this diagram and the discussion
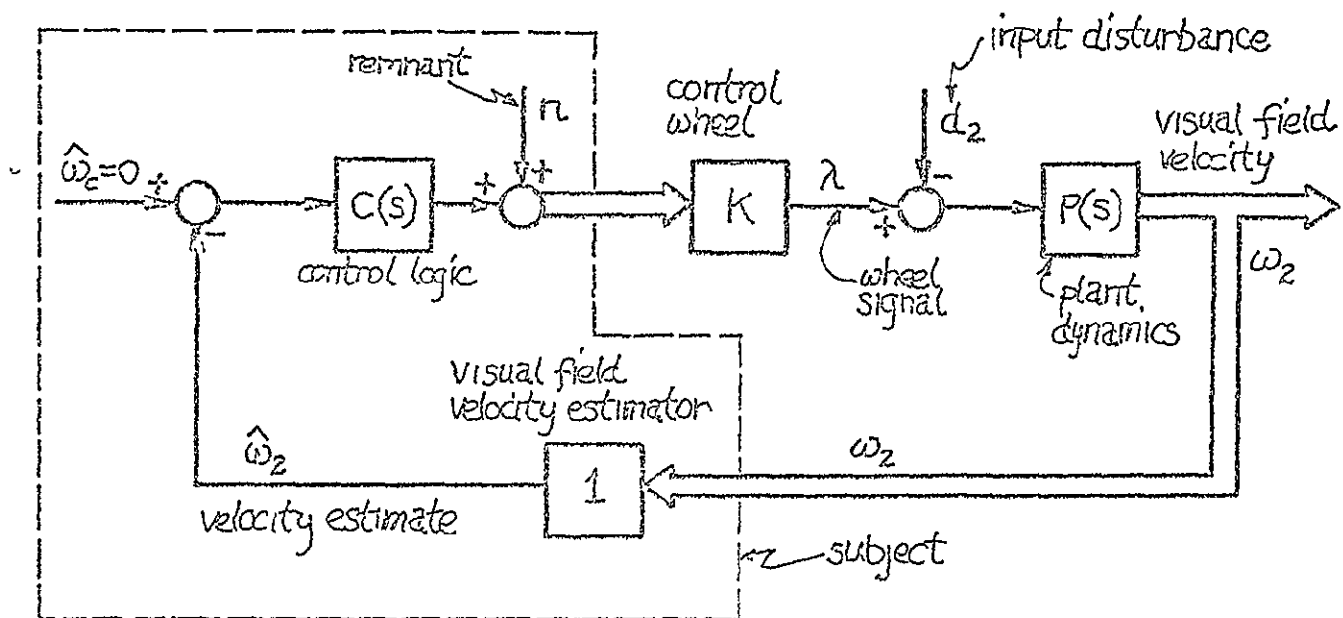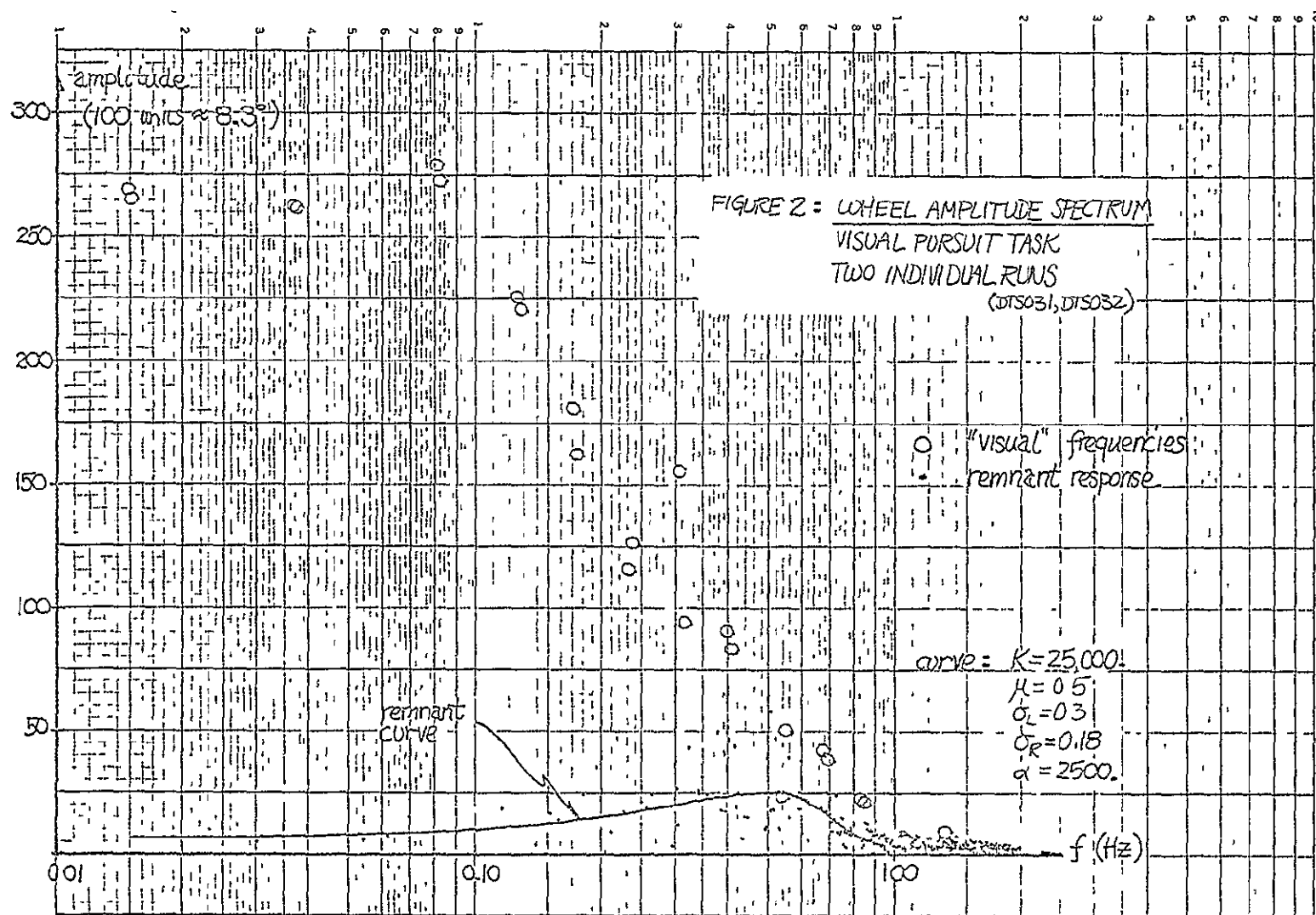
88

FIGURE 1 : VISUAL FIELD VELOCITY NULLING TASK

concerning cross-correlation functions given earlier, it is a direct matter to show that the control strategy C(s) is defined at the input disturbance frequencies $m_i\omega_0$ by the following relation·

$$KC(m_i\omega_0) = -\frac{\Phi_{\lambda d_2}(m_i\omega_0)}{\Phi_{\omega_2 d_2}(m_i\omega_0)} = -\frac{\lambda(m_i\omega_0)}{\omega_2(m_i\omega_0)} \qquad (1)$$

so that direct calculations from FFT results may be utilized

In this experimental series, 6 subjects attempted to null field velocity for two full periods of the disturbance signal (T = 128 sec.), for a total individual run time of 256 seconds. The FFT's were performed on each 128-second segment, so that two estimates of KC were obtained for each subject. It is appropriate to note that 4 of the subjects participating in this series also participated in the DI series (IV), so that it will be possible later to divide out control strategy, on an individual-by-individual basis

Shown in figure 2 are two sets of amplitude spectra obtained from one subject, illustrating the relatively large compensatory response at the input frequencies (circles) and the small remnant (dots). As was done earlier, a smooth curve has been drawn through the remnant amplitudes, to provide a simple approximation for remnant corrections to be introduced later. A comparison with similar data obtained from the self-velocity nulling experiments (series I through IV) shows considerably higher response amplitudes for the present task, indicative of either a higher gain in the control block C, or of attenuation in the self-velocity estimator blocks (E_1 and E_2). This is also reflected in the higher S/N

amplitude
(100 units ≈ 8.3°)

FIGURE 2 : WHEEL AMPLITUDE SPECTRUM
VISUAL PURSUIT TASK
TWO INDIVIDUAL RUNS
(DTS031, DTS032)

○ "visual" frequencies
• remnant response

curve : $K = 25,000$
$\mu = 0.5$
$\sigma_L = 0.3$
$\sigma_R = 0.18$
$\alpha = 2500.$

remnant
curve

f (Hz)

300

250

200

150

100

50

0.01

0.10

1.00

ratios seen in this task, In this instance the computed S/N power ratios arc 34.8 and 33.8 dB for the subject's two presentations, (to be compared with considerably lower S/N ratios for the DI experiment, for example).

Shown in figure 3 are amplitude ratio (AR) population averages for the six subjects, computed for this task from (1), with the bars indicating one-sigma spread. Superimposed on these data are corresponding AR's which have been corrected for each individual's remnant power, so as to get a more accurate estimate of the linear transfer function C(s). The remnant correction method will not be discussed here, as it is the subject of a later section. What is important to note, however, is that the two data sets, corrected and uncorrected, are obviously insignificantly different, and thus the simple transfer function approach of (1) is quite adequate for obtaining an estimate of C(s), especially in view of the data spread.
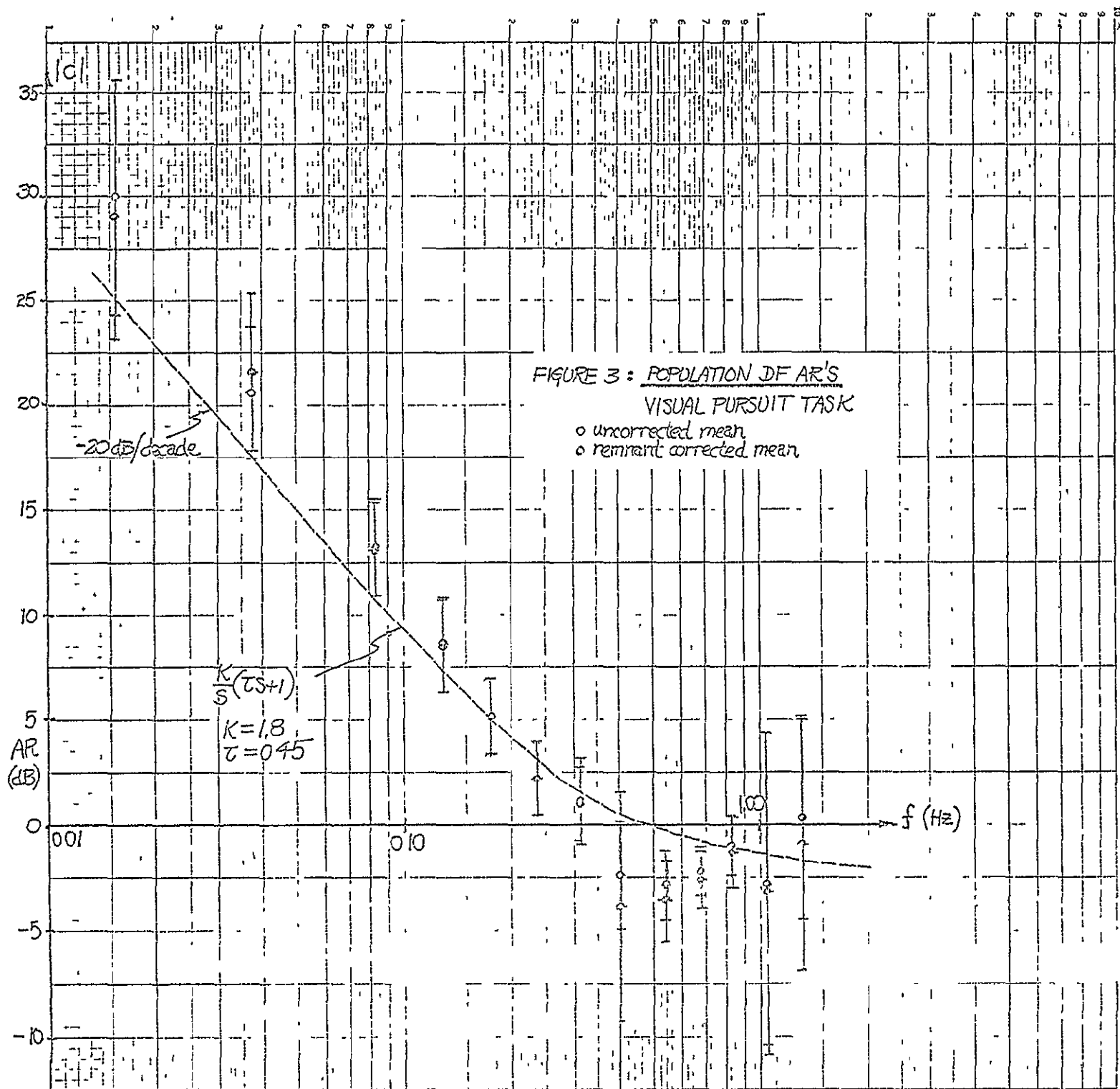
From the figure, the gain trends are quite obvious· integration at the low frequencies, followed by a mid-frequency lead break, similar to what was seen in the AR data defining the "visual" estimator/controller function CE_2. This motivates the fitting of the following function to the AR data:

$$\frac{K}{s}(\tau s + 1) \tag{2}$$

The dashed line in the figure shows one such fit obtained by a visual fit of asymptotes; the parameter values are given by:

$$K = 1.8 \qquad\qquad \tau = 0.45 \tag{3}$$

FIGURE 3: POPULATION DF AR'S
VISUAL PURSUIT TASK
o uncorrected mean
o remnant corrected mean

It should be noted that these are not the result of a least-squares
fitting algorithm (which will be done shortly), but simply rough
estimates. It is also appropriate to note that the low frequency
gain drop-off in the data is greater than the 20 dB/decade attribu-
table to a simple integrator, and the mid-frequency break seen in
the data is sharper than a break associated with a simple first-order
lead term. These discrepancies between model and data may motivate
the use of higher-order functional curve fits; for now, however, the
basic integrator plus lead function appears adequate.

The corresponding phase data obtained from this experimental series
are presented in figure 4, and although not fully corroborative of the
gain data, do show a constant phase lag of 120° at the low frequencies
(where we would expect a 90° lag with a simple integrator). Also ske-
tched on the figure is the predicted phase curve for the transfer func-
tion defined by (2) and (3). The discrepancy between the curve and the
data at high frequencies is presumably due to human operator latencies,
which can be modelled by a dead-time term, $e^{-\tau_d s}$. The resulting phase
shift is seen in the second curve on the figure, a reasonable approxi-
mation to the phase data is obtained by choosing a dead-time of 0.32
seconds. Again, a better fit can be expected with the eventual ap-
plication of a least-squares program to the data

As noted in the beginning of this section, the plots defining C(s)
can be used to infer the estimator functions (E_1 and E_2) from the DI
experimental data. One approach, given in the next section, is to
simply divide 6-subject means from the two experimental series; that
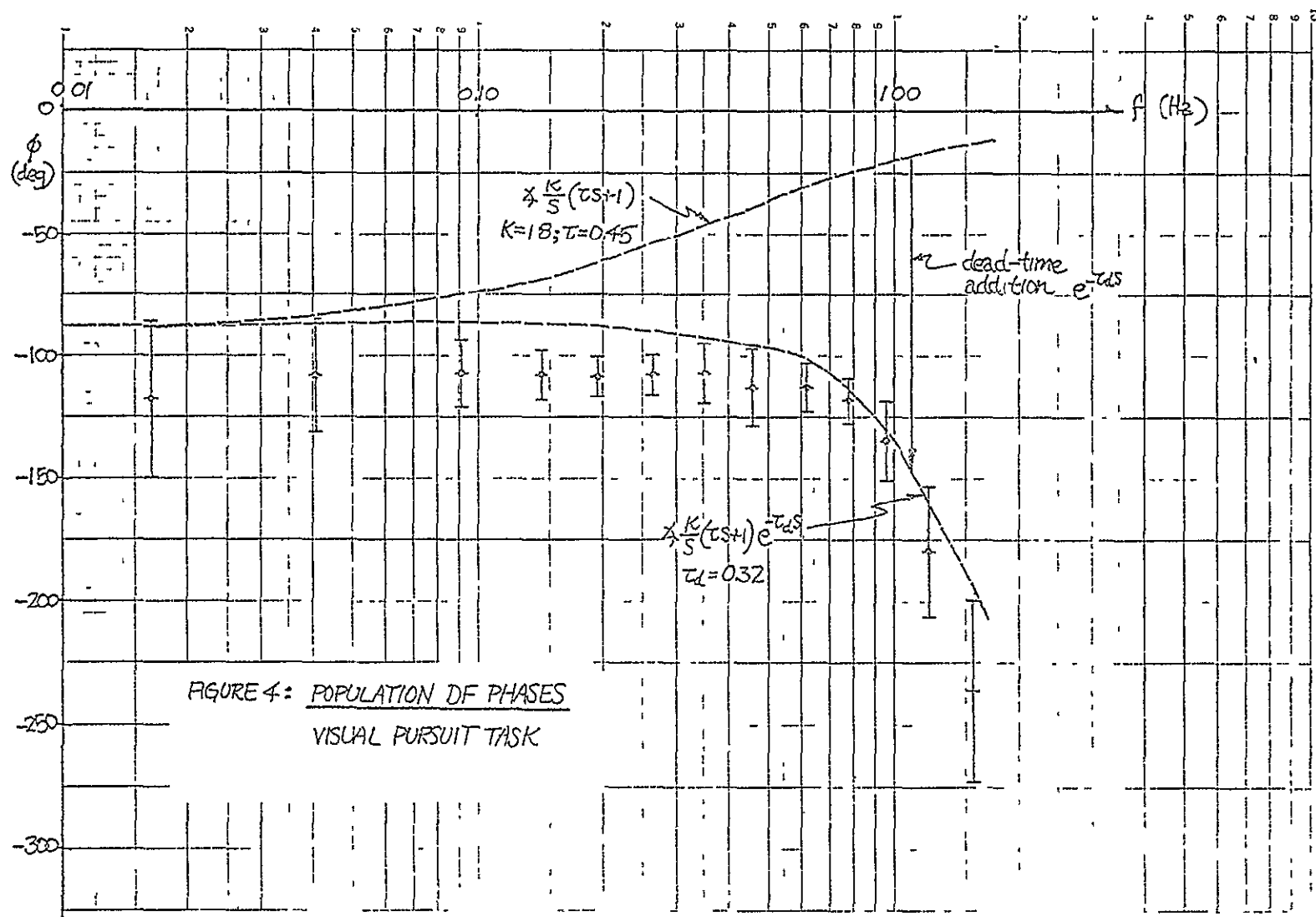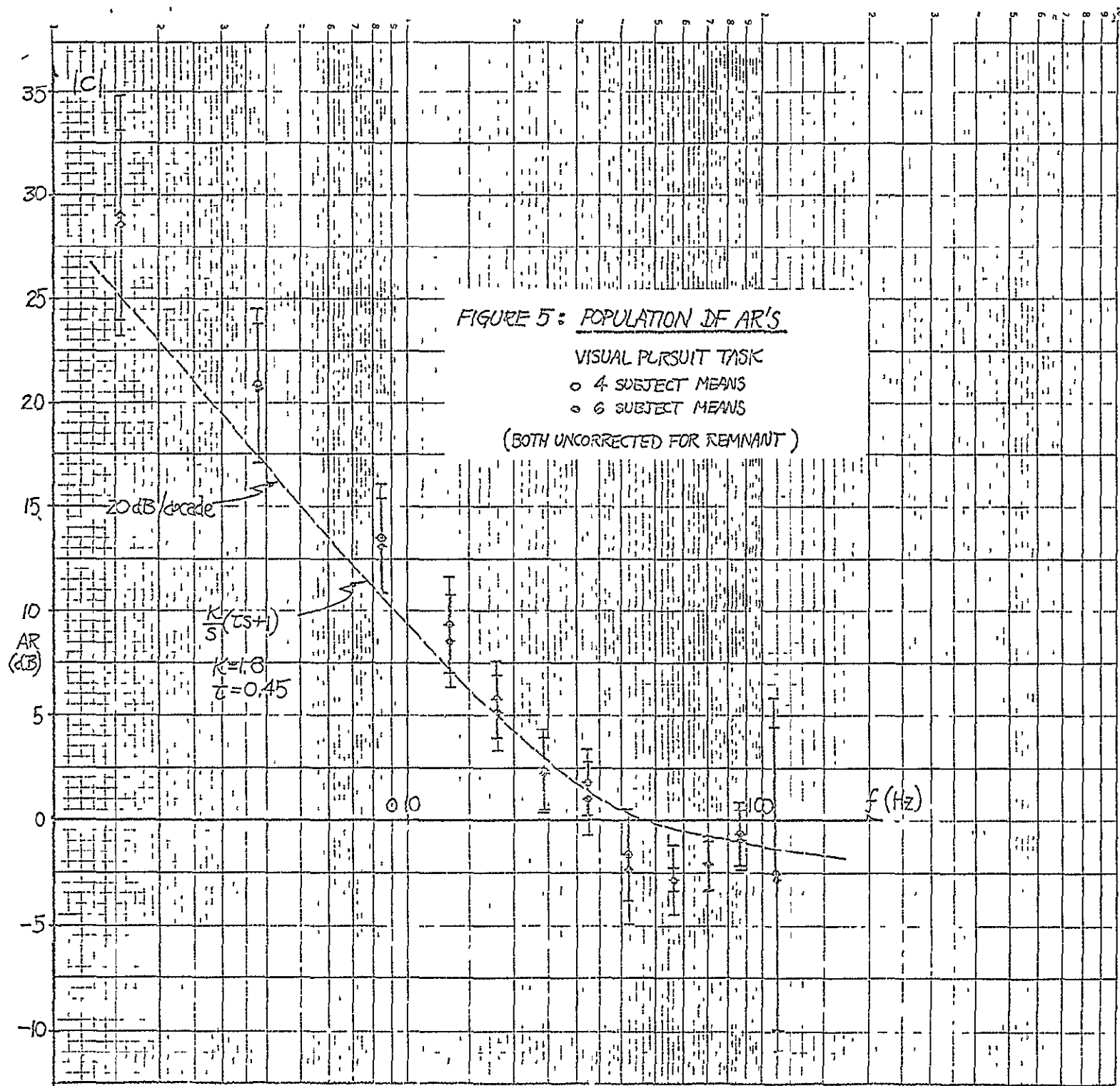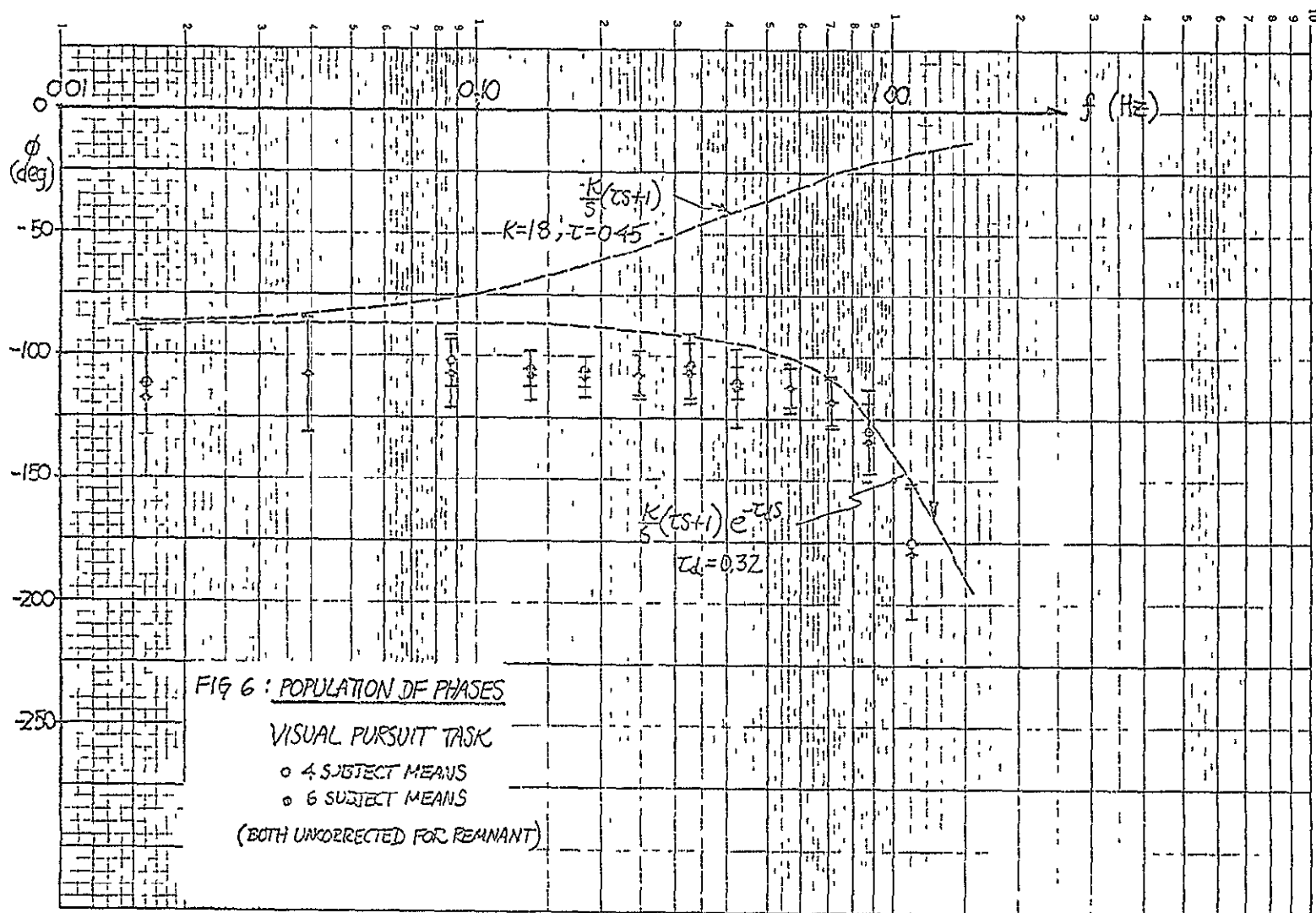is, at each frequency, divide the mean value for $|CE_1|$ by the mean

FIGURE 4: POPULATION OF PHASES
VISUAL PURSUIT TASK

value for $|C|$, to obtain an estimate for $|E_1|$, and similarly for $|E_2|$. Obviously, the same approach can be used for the phases.

An alternative approach, also presented in the next section, is to divide each individual's DI data by his manual control data, and then find average values for the resultant estimates of E_1 and E_2. It was noted earlier that only four subjects participated in both experimental series, so that the population is a subset of what has been considered so far. To show that the population average Bode plots for the four-subject population are not significantly different from those obtained for the six-subject population, it is only necessary to look at figures 5 and 6, where the two data sets are superimposed on one another. A formal test of equivalence involves t-tests on curve fit parameters, but curve-fitting of each data set is yet to be done. It should be obvious however, that the two data sets are not significantly different, and thus we might expect that the two approaches used in the next section to estimate the estimator functions will yield essentially the same results

FIGURE 5: POPULATION OF AR'S

VISUAL PURSUIT TASK
o 4 SUBJECT MEANS
o 6 SUBJECT MEANS

(BOTH UNCORRECTED FOR REMNANT)

FIG 6 : POPULATION OF PHASES

VISUAL PURSUIT TASK
o 4 SUBJECT MEANS
⊙ 6 SUBJECT MEANS
(BOTH UNCORRECTED FOR REMNANT)

7.0 ESTIMATOR FUNCTIONS FOR PARALLEL CHANNEL MODEL

In section 5, we obtained the gain and phase plots defining the combined controller/estimator functions for the parallel channel model, CE_1 and CE_2, and in the previous section we obtained similar plots which define the control function C. It is the purpose of this section to divide out the control law from the earlier results to obtain estimates of the estimator functions E_1 and E_2.

7.1 Population Division

The simplest approach to the problem is to simply divide the six-subject means from the two series (IV and VI) to obtain an estimate of the population mean for each E_i. Thus, at each frequency, divide the mean value for $|CE_1|$, obtained from Figure 5 of section 5, by the mean value for $|C|$, from Figure 3 of section 6, to obtain an estimate of the mean of $|E_1|$. The same can be done for E_2, and obviously a similar approach is applicable to phase angle calculation for both functions.

The results of such calculations are shown in Figures 1 and 2. In both figures the closed circles denote E_1 values, while the open circles denote E_2 values, the dashed lines only indicate trends with frequency and are not to be mistaken for fitted curves. Several points should be noted. First, the gain curve associated with E_1 exhibits a rapid drop-off at low frequencies and a levelling out at the higher frequencies, behavior which is entirely consistent with our notion of a "vestibular" transfer
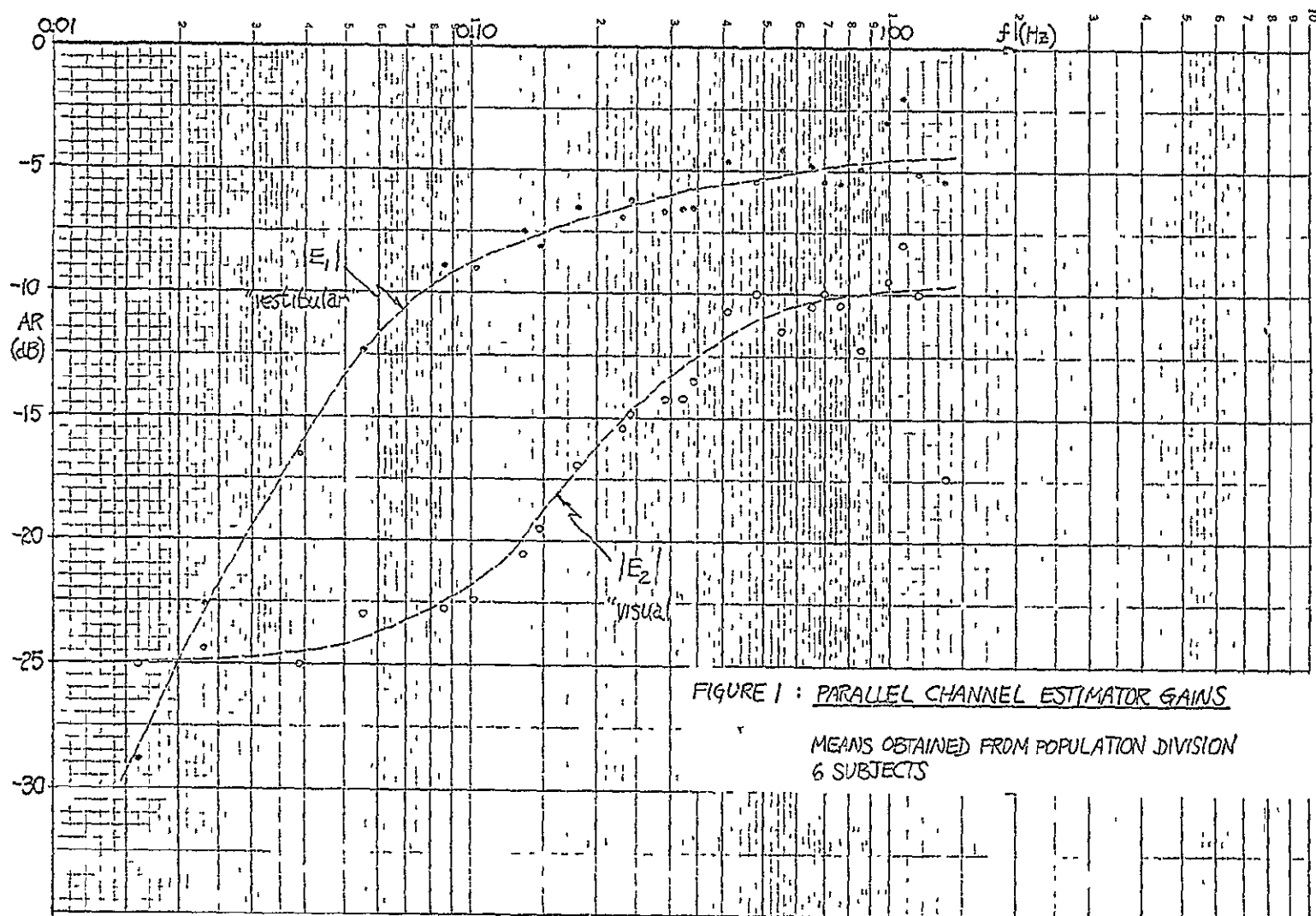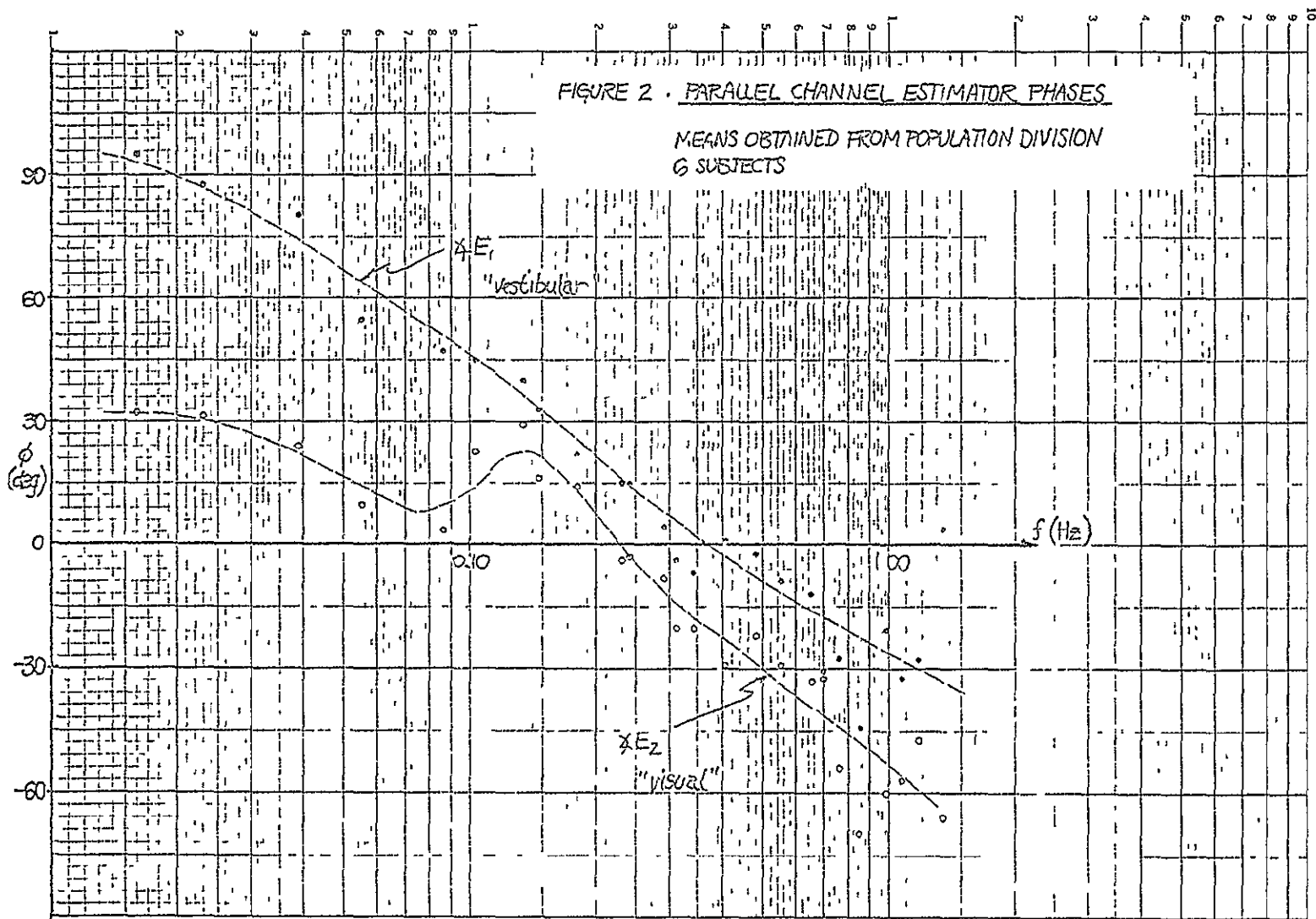
FIGURE 1 : PARALLEL CHANNEL ESTIMATOR GAINS

MEANS OBTAINED FROM POPULATION DIVISION
6 SUBJECTS

FIGURE 2 · PARALLEL CHANNEL ESTIMATOR PHASES

MEANS OBTAINED FROM POPULATION DIVISION
6 SUBJECTS

function. Had the experimental equipment allowed for a higher range of test frequencies to be used, we presumably would have seen an eventual drop-off in the E_1 gain, corroborating the previous findings of vestibular dynamics characterized by a bandpass filter centered around the frequency regime of normal physiological motions. The phase curve associated with E_1 is shown in Figure 2 and illustrates the expected 90° lead at low frequencies (characteristic of a "washout") with a gradual drop-off at mid-frequencies. With a simple washout we would expect zero lag at the highest frequencies; presumably the lag seen in the figure is due to operator latencies.

The behavior of the data characterizing the visual channel transfer function E_2 shows a considerable contrast. As noted in an earlier section, the visual gain (Figure 1) is a good deal lower than the vestibular gain over much of the frequency range, with approximate equality occuring only at the very low end. In this regime, the visual gain is approximately constant with frequency, in agreement with our knowledge of   circular-vection   a non-zero gain at zero frequency. However, the gain increase seen in the mid-frequency regime is unsettling, since it suggests increased velocity sensitivity with higher frequencies, behavior which is in conflict with the complementary filtering model. In fact, what we would have expected is a _drop_ in gain with increasing frequency, so that the only source of high frequency motion information would be by the vestibular pathway. The data shown here contradicts such a notion.

There are at least four points worth considering before arriving at any definite conclusions regarding the results just presented. The first is that the results were obtained by dividing the data from one six-subject

population by the data from a different six-subject population. Inter-subject variation could be a subtle cause of the unexplained visual gain behavior.To resolve this point, transfer function divisions have been made on an individual-by-individual basis for the 4-person subset of subjects participating in both experimental series. The results are the subject of the next subsection.

The second point is that the results shown here are based on data which was not corrected for operator remnant contributions. It may be recalled from section 6 that the corrected and uncorrected gains associated with the control strategy C did not significantly differ, and thus it might be surmised that such a correction would be of little value here However, it should also be recalled that the visual field velocity nulling task (Series VI, used to determine C) was characterized by relatively high S/N ratios. This is to be contrasted to the data obtained from the dual-input experiment (series IV), in which considerably lower S/N ratios were obtained for the visual channel (recall figure 2 of section 5). Thus, one might expect that the visual transfer function inferred from the DI experiment, CE_2, would show a more significant change when remnant corrections are incorporated. Presumably, such a change would be reflected in the calculated gain and phase for E_2 presented here, and thus "correct" the increasing gain tendencies seen in Figure 1. The results of such an approach will be discussed in section 8.

The third point reflects on the validity of the proposed parallel channel linear model: the model fails to incorporate a non-linear gain characteristic, a property often associated with human operator behavior. Specifically, we note that for the visual channel, the gain increases

at the higher frequencies. But from Figure 3 of section 4, we should

recall that the amplitudes of the input disturbances decrease with

increasing frequency. Thus, the possiblity exists that what we are

observing is not a gain dependence on frequency, but on amplitude: a

gain increase with decreasing amplitudes. This type of non-linear gain

function is sketched in figure 3, and is consistent with behavior seen

in subjective estimation performance in psychophysical experiments
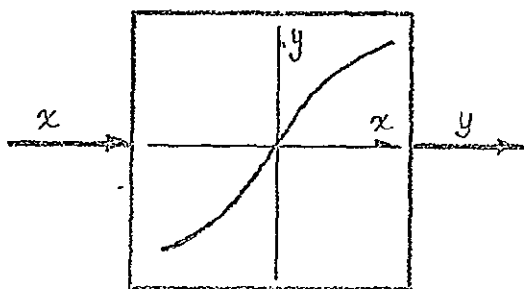
Consideration of this problem is a current area of effort.

FIGURE 3 : NON-LINEAR GAIN

$\frac{dy}{dx}$ decreases as $|x| \to \infty$

A final point worth noting is that the parallel channel model, as

is, may be a quite valid representation of the human velocity estimator,

and the data trends of figures 1 and 2 may be an accurate description of

the two individual transfer functions of the model. What then remains

to be resolved, however, are the conflicts between the predictions of this

model and the results obtained in past circularvection studies. For instance,

if the visual channel does indeed have a significant gain at high frequencies,

why then does the observed circularvection sensation build up so slowly,

in response to a step input of visual field velocity? Or, more to the

point, why do high frequency (say 1 Hz) oscillations of the peripheral

visual field fail to elicit a circularvection sensation, whereas low

frequency (say 0.01 Hz) oscillations do?

7.2 Individual Division

Shown in figures 4 though 7 are gain and phase plots showing average values for E_1 and E_2, calculated by dividing an individual's response in one experimental session (IV) by his response in the other (VI), and then averaging over the 4-subject test population. This approach corrects for intersubject gain variation, and further, allows for a calculation of gain and phase standard deviations at each frequency. One sigma bars are shown on the figures.

A comparison of these results with those described above (figures 1 and 2) shows that this method of transfer function estimation yields essentially the same results, as expected. It may be noted that the E_1 gains are generally lower here than those of figure 1, and that the low frequency phase leads for both functions are lower than those of figure 2, but, otherwise, the results are basically unchanged. Specifically, the increase in the visual channel gain with frequency is still present, and cannot be accounted for on the basis of intersubject variations.
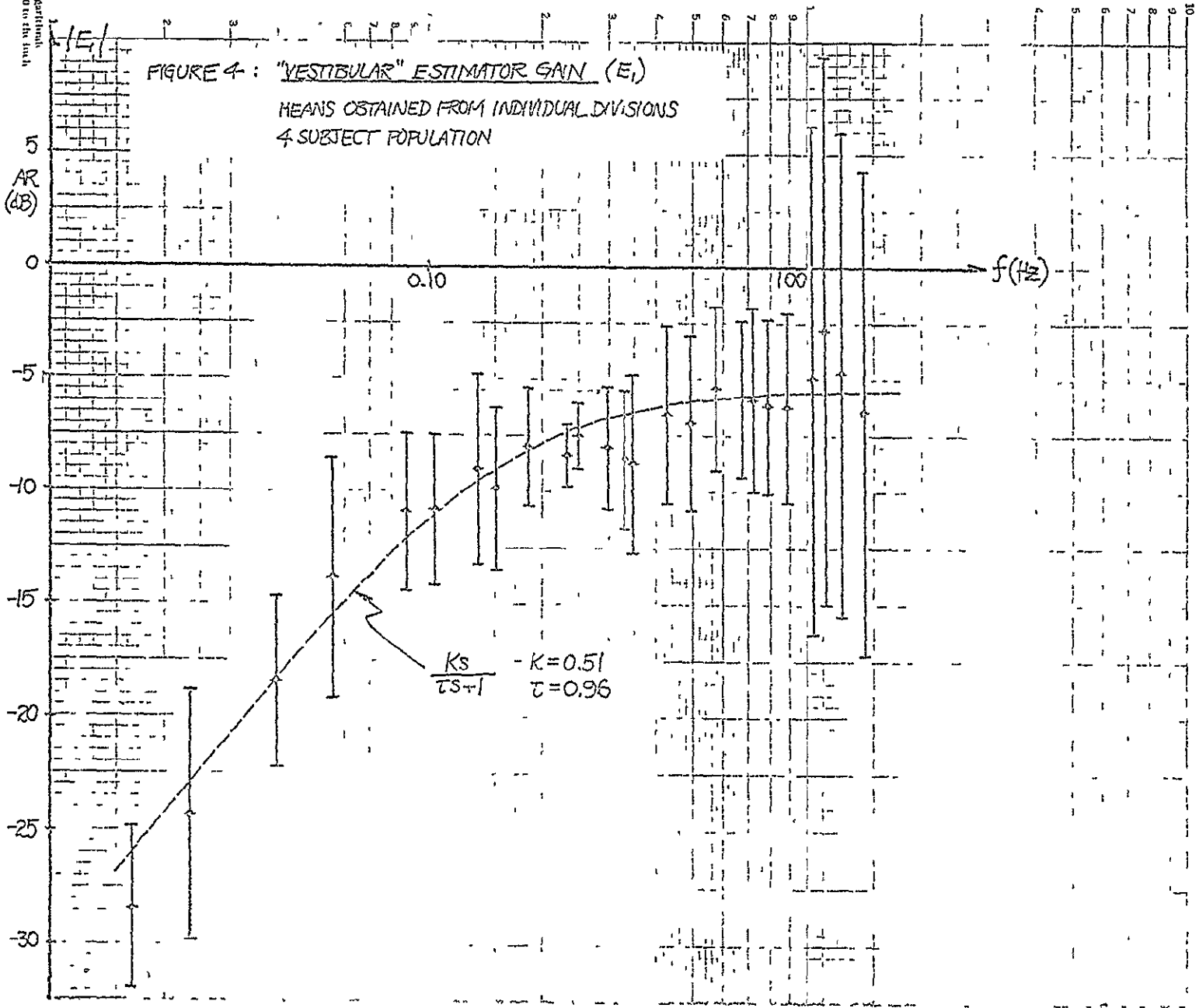
The figures also illustrate proposed transfer function curves, obtained from a simple visual inspection of the data: a washout for E_1, and a lead-lag for E_2. The actual parameter values are only rough estimates, and not the results of a least squares curve fit program. It is evident that both functions do a fair job of fitting the AR data means; the phase data , however, requires the addition of dead-time terms to follow the phase

FIGURE 4: "VESTIBULAR" ESTIMATOR GAIN (E_1)

MEANS OBTAINED FROM INDIVIDUAL DIVISIONS
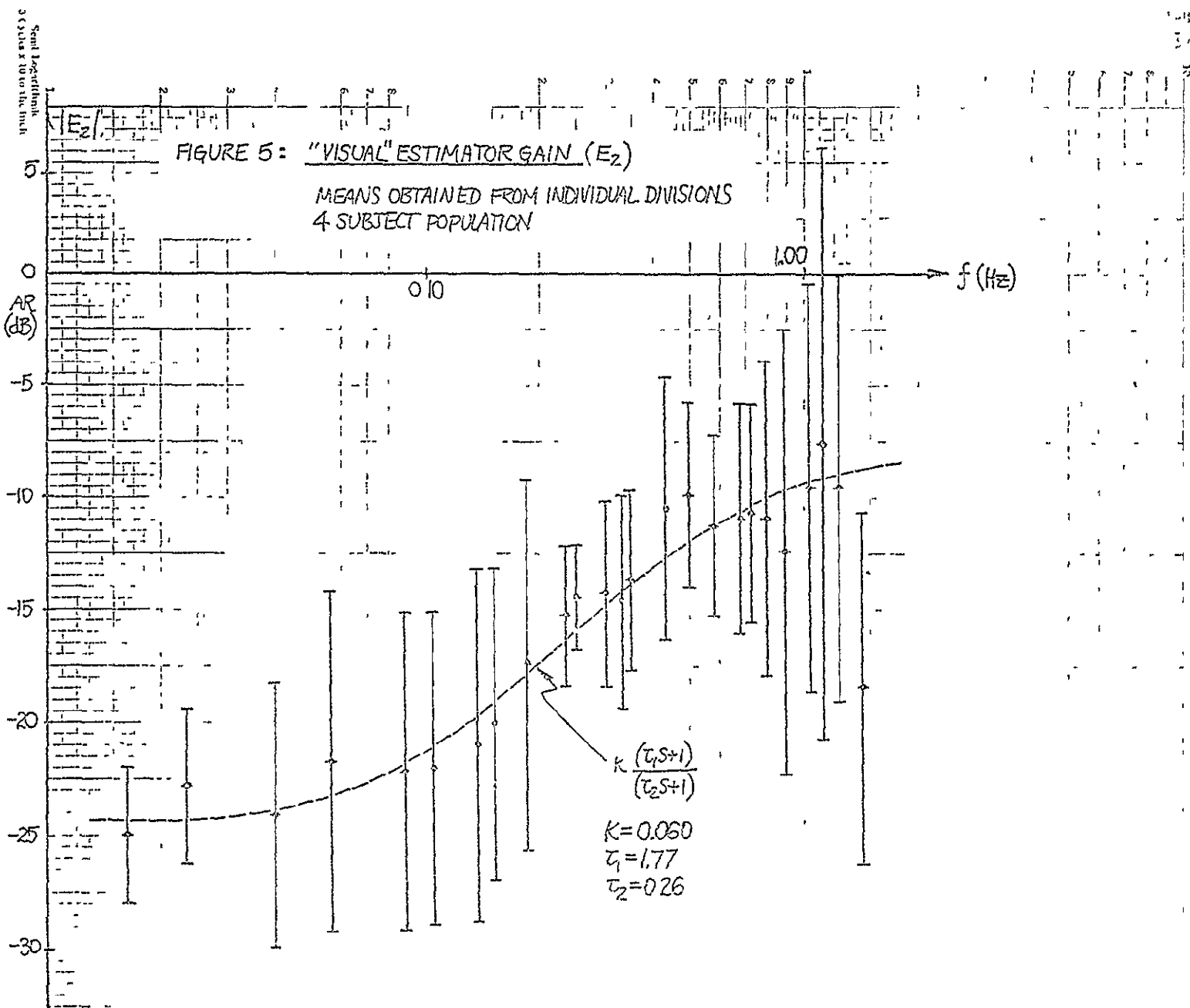
4 SUBJECT POPULATION

$\frac{Ks}{\tau s+1}$ — K=0.51 τ=0.96

108

FIGURE 5: "VISUAL" ESTIMATOR GAIN (E₂)

MEANS OBTAINED FROM INDIVIDUAL DIVISIONS
4 SUBJECT POPULATION

$$K \frac{(\tau_1 S + 1)}{(\tau_2 S + 1)}$$

$K = 0.060$
$\tau_1 = 1.77$
$\tau_2 = 0.26$

//

FIGURE 6 : "VESTIBULAR" ESTIMATOR PHASE (E_1)

MEANS OBTAINED FROM INDIVIDUAL DIVISIONS
4 SUBJECT POPULATION

$$\angle \frac{KS}{\tau S+1} \qquad K=0.51 \\ \tau=0.96$$

$$\angle \frac{KS}{\tau S+1} e^{-\tau_d S} \\ \tau_d=0.2$$

/08

112

FIGURE 7 : "VISUAL" ESTIMATOR PHASE (E_2)

MEANS OBTAINED FROM INDIVIDUAL DIVISIONS
4 SUBJECT POPULATION

$\not{\star} K \dfrac{\tau_1 s + 1}{\tau_2 s + 1}$

$K = 0.060$
$\tau_1 = 1.77$
$\tau_2 = 0.26$

$\not{\star} K \left(\dfrac{\tau_1 s + 1}{\tau_2 s + 1}\right) e^{-\tau_d s}$

$\tau_d = 0.20$
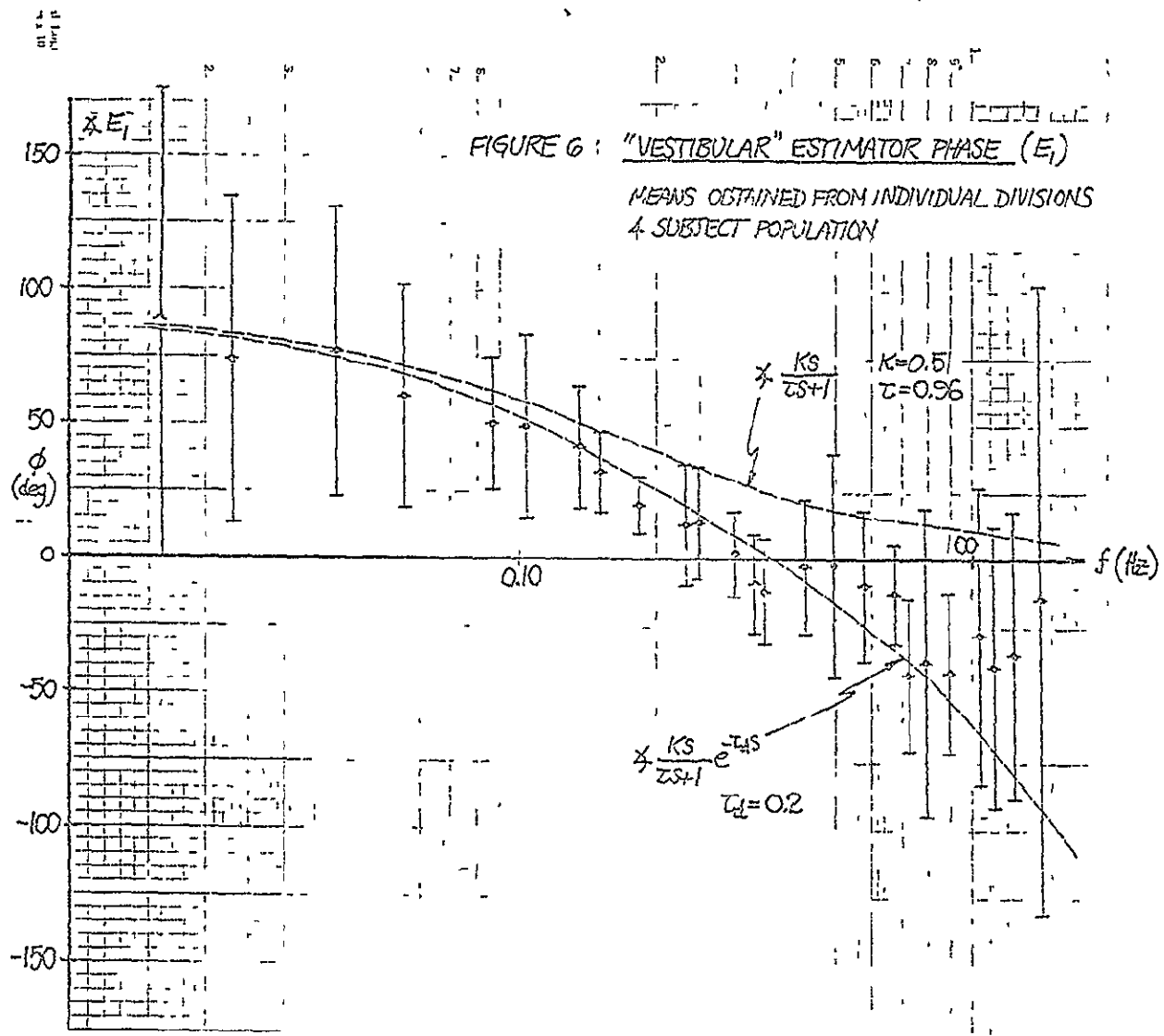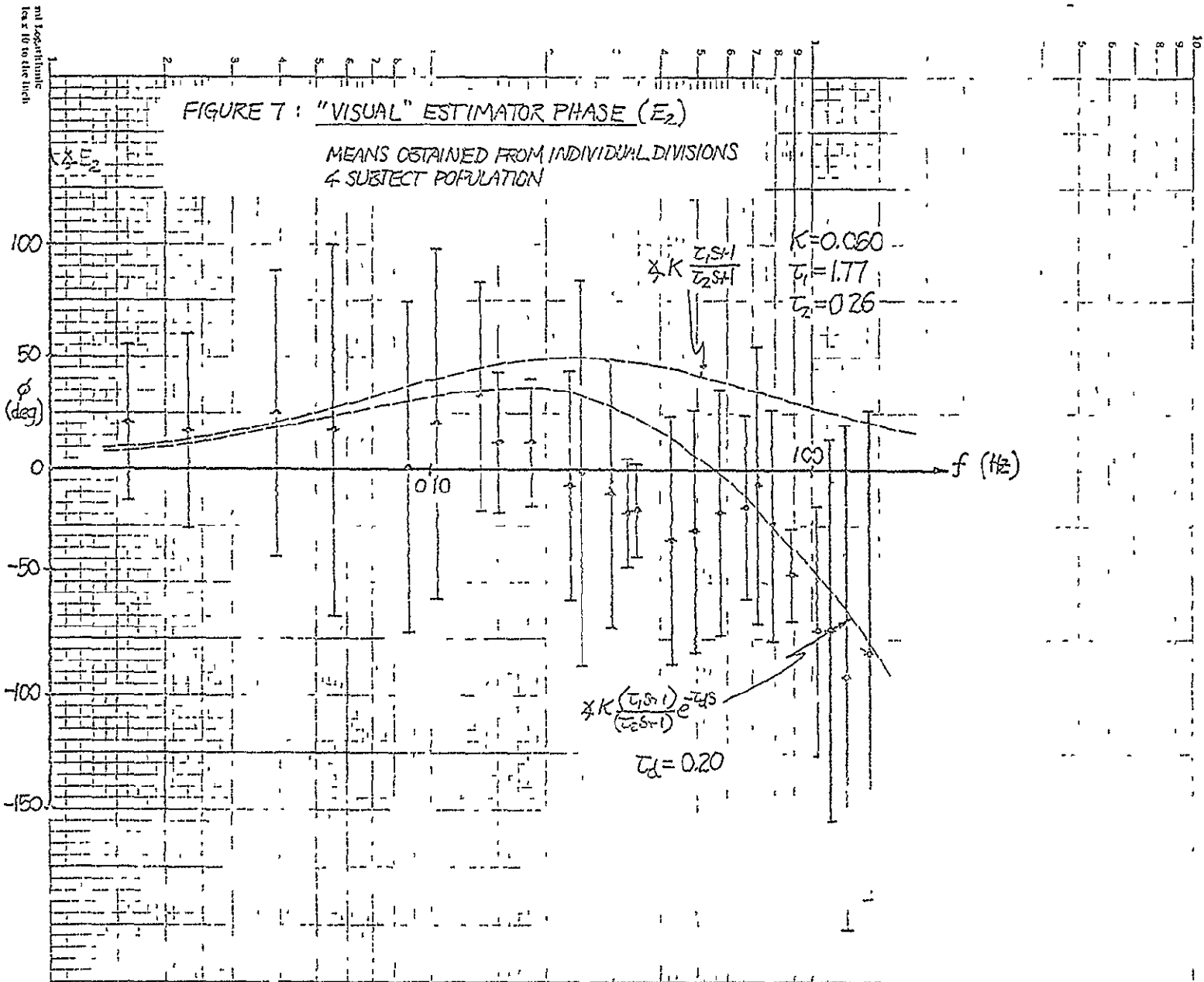
lag trends at high frequencies. Although this type of latency can be justified by assuming some type of estimation computation time, it should be clear from figure 7 that the augmented transfer function fit to the visual channel phase is not particularly satisfying, especially in the mid-frequency range.

At this point, it is appropriate to investigate the effect of remnant corrections on the data, to see if the visual channel gain trends are affected, and if such corrections afford an improvement in transfer function curve fitting.

Part 8 of this section of the report is in preparation.